Error Controlled Adaptive Multiscale Method for Fracture in Polycrystalline Materials

Ahmad Akbari Rahimabadi

Supervisors:
Dr. Pierre Kerfriden
Prof. Stéphane Bordas

A thesis submitted to the graduate school
in fulfilment of the requirements for the degree of
Doctor of Philosophy

Institute of Mechanics and Advanced Materials
Theoretical and Computational Mechanics

School of Engineering

Cardiff University
September 25, 2014

I would like to dedicate this thesis to my loving wife, Sara.

Acknowledgements

I would like to express my very great appreciation to my supervisors, Dr Pierre Kerfriden and Prof. Stéphane Bordas for their mentorship and kind help during my PhD.

I offer my sincere appreciation to my viva committee, Dr Michele Meo from the University of Bath, Dr Kirill Cherednichenko from the School of Mathematics at Cardiff University for their valuable feedback and Dr Carol Featherston as Chairperson.

I would like to offer my special thanks to my dear friend, Dr Claire Heaney, who kindly reviewed my thesis word by word. Advice given by my dear friend, Dr Sundar Natarajan, has been a great help in the beginning of and during my PhD. I am particularly grateful for the assistance given by Olivier and Danas by reviewing my reports and articles. I am very grateful for the casual discussions with Danas and Daniel about FE and fracture mechanics. The weekly seminars in the School of Mathematics held by Prof. Tim Phillips are very appreciated. My completion of this thesis could not have been accomplished without the support of my fellow classmates.

Thanks to Sundar, Chang-Kye, Daniel, Haojie, Olivier, Claire, Danas, Phu, Chi, Xuan, Hadrien, Pierre, Stéphane, Joseph, Andrés, Robert, Julia, Lars form Institute of Mechanics and Advanced Materials (IMAM), and Audrey, Olduz, Amir Hossein, Azadeh, Navid, Jorge, Lordes, Shaya, Khabir, Hazem, Riyadh, Ahmed, Susanne, Julia, Majid, Mozhgan, Mark and Maysam for making such memorable time for me in Cardiff.

My special thanks are extended to the staff of Research office at Cardiff University. I would also like to thank the University of Wit-

watersrand, especially Dr Jacob Muthu for providing me the research facilities during my visit to Johannesburg, South Africa. I am very thankful for the love and support of my Joburg-based family, Changiah, Laurel, Samara, Avi, Turgay, Di, Johanna and Emma who gave me a home away from home.

I would like to thank the Cardiff School of Engineering for the generous studentship support. I would also like to acknowledge the fund provided by Marie Curie foundation through MultiFrac project that supported my visit to Witwatersrand University for seven months.

Finally, to my caring, loving, and supportive wife, Sara: my deepest gratitude.

Ahmad Akbari Rahimabadi

Kermanshah - September 2014

Abstract

A lack of separation of scales is the major hurdle hampering predictive and computationally tractable simulations of fracture over multiple scales. In this thesis an adaptive multiscale method is presented in an attempt to address this challenge. This method is set in the context of FE^2 Feyel and Chaboche [2000] for which computational homogenisation breaks down upon loss of material stability (softening). The lack of scale separation due to the coalescence of microscopic cracks in a certain zone is tackled by a full discretisation of the microstructure in this zone. Polycrystalline materials are considered with cohesive cracks along the grain boundaries as a model problem. Adaptive mesh refinement of the coarse region and adaptive initiation and growth of fully resolved regions are performed based on discretisation error and homogenisation error criteria, respectively. In order to follow sharp snap-backs in load-displacement paths, a local arc-length technique is developed for the adaptive multiscale method. The results are validated against direct numerical simulation.

Contents

Contents v

List of Figures vii

1 Introduction 1

1.1 Multiscale approaches for fracture modelling 2

1.1.1 Non-concurrent multiscale approaches for fracture 4

1.1.2 Concurrent multiscale approaches for fracture 7

1.2 Proposed multiscale method 13

1.3 Outline 14

2 Constitutive Modelling of Polycrystalline Materials 16

2.1 Introduction 16

2.2 Microstructure model formulation 20

2.3 Microscopic constitutive equations 22

2.3.1 Bulk Grain constitutive law 22

2.3.2 Cohesive interface model for grain boundaries 22

2.4 Finite Element Discretization 30

2.5 Conclusion 34

3 Hierarchical and Concurrent Multiscale Methods 36

3.1 Hierarchical Multiscale: FE^2 Method 37

3.1.1 Macroscopic problem 38

3.1.2 Homogenised constitutive law 40

3.1.3 Limitations 47

3.2 Concurrent Multiscale: Domain Decomposition Method 49
3.2.1 Coupling Fine-Coarse meshes 50
3.2.2 Solving the coupled problem 53
3.2.3 Convergence Criteria 54
3.3 Conclusion 55

4 Solution Procedure **57**
4.1 Local Arc-length technique 58
4.2 Error Estimation and Adaptive Mesh Refinement 64
4.2.1 Homogenisation error 65
4.2.2 Zienkiewicz-Zhu error estimation 68
4.2.3 Coarse mesh refinement procedure 71
4.3 Adaptive expansion of fully resolved region 72
4.3.1 Equalisation process 74
4.3.2 Relaxation 75
4.4 Conclusion 75

5 Example Applications **78**
5.1 Determining the size of RVE 78
5.2 Numerical Example 85
5.2.1 Notched Beam 85

6 Conclusions and outlook **94**
6.1 New developments 95
6.2 Conclusions 96
6.3 Future perspective 97

Appendix A **99**

References **106**

List of Figures

1.1 A taxonomy for multiscale methods in mechanics. 3
1.2 Non-concurrent multiscale for fracture. Figure from [Alfaro et al., 2009]. 4
1.3 Concurrent multiscale modelling of fracture 7
1.4 A concurrent multiscale method for modelling of fracture: There is no control on discretisation or homogenisation errors. Picture from [Lloberas-Valls et al., 2012]. 9
1.5 *"The top-down multi-level model showing components of concurrent coupling, viz. continuum level-0, level-1 of asymptotic homogenization and level-2 of micromechanical analysis"* [Ghosh et al., 2007]. 11
1.6 A concurrent multiscale method: The homogenisation error is controlled by adapting the microscale, and discretisation error is controlled by the coarse mesh refinement. Picture from [Temizer and Wriggers, 2011]. 13

2.1 Two simple traction-separation laws for cohesive interface modelling. 17
2.2 Microscale problem 20
2.3 Local coordinates on the boundary of a grain $(\tilde{x}, \tilde{y})$, Local coordinates on the principal direction of the orthotropic grain $(1, 2)$, and global coordinate (x, y). 23
2.4 A schematic illustration of a damage evolution function based on Eqs. (2.23) and (2.24). In this figure, $\kappa_{\text{ini}} = 0.2$, $\kappa_{\text{full}} = 0.8$ and $n = 0.5$. 26

2.5 Variation of α and β versus n (see Eqs. (2.27) and (2.28)). Different choice of n can affect the original stiffness of cohesive cracks ($k_n \propto \beta$) and the required jump for a fully damaged crack ($[\![\mathbf{u}^f]\!]_{\text{full}} \propto \alpha$). 28

2.6 Traction-displacement curve for different value of parameter n in one dimension cohesive interface. In this figure, $\kappa_{ini} = 0$, the critical fracture energy equals $G_{Ic} = 35\frac{J}{m^2}$ and the maximum tensile strength is $\sigma_{\max} = 1\text{GPa}$ [Shabir et al., 2011]. 29

2.7 Local coordinate system on the boundary of a grain, $(\tilde{x}, \tilde{y})$, and displacement jump, $[\![\mathbf{u}]\!]$ in the local coordinate system. It is noted that the translation and rotation of local coordinates due to deformation can be neglected since small deformation is assumed. The node arrangement in the cohesive element must be based on the following construction: a) Node 1 and Node 3 belong to one grain, and Node 2 and Node 4 belong to the other grain, b) Node 1 has same position of Node 2, and Node 3 has the same position of Node 4, c) Nodes 1 and 3 must be chosen so that their grain fallen in the left side of the path from Node 1 to Node 3, d) The unit vectors of the local coordinate system are given by $\hat{\mathbf{t}} = \dfrac{\mathbf{x}_3 - \mathbf{x}_1}{\|\mathbf{x}_3 - \mathbf{x}_1\|}$ and $\hat{\mathbf{n}} = [\hat{t}_x \ , \ -\hat{t}_y]^T$, e) Therefore the displacement jump is defined by: $[\![\mathbf{u}^f(\tilde{y})]\!] = \mathbf{u}^f_B(\tilde{y}) - \mathbf{u}^f_A(\tilde{y})$. 31

3.1 FE^2 scheme 41

3.2 Flowchart for the FE^2 scheme. 47

3.3 Overlapping and non-overlapping domain decomposition methods. 48

3.4 A hybrid multiscale method includes non-overlapping domain decomposition method and FE^2. See also Fig.3.6 49

3.5 Strong coupling vs. weak coupling in non-overlapping DDM in deformed configuration. 51

3.6 Strong coupling between the fine mesh and the coarse mesh using the linear multipoint constraint (LMPC) method. 52

4.1 Load-displacement equilibrium obtained by the load control and displacement control procedures. The unphysical equilibrium path, shown by dash-line, cannot be followed by the load control and displacement control procedures. 59
4.2 The variation of the displacement jump $[\![\mathbf{u}^f]\!]$ at the middle point ζ_m of cohesive element e 61
4.3 The evaluation of the admissible interval S_a for the variational load factor $\delta\gamma$ in the local arc-length method. 63
4.4 The variation of homogenisation error and discretisation error with respect to the coarse element size in FE^2 [Vernerey and Kabiri, 2012]. 66
4.5 First displacement gradient, $\nabla\mathbf{u}$, second displacement gradient, $\nabla\nabla\mathbf{u}$, and the recovery-based second displacement gradient, $\nabla\nabla^*\mathbf{u}$, for a one-dimensional problem and linear shape functions. 69
4.6 Coarse mesh refinement in FE^2 method, and copying the RVEs from old mesh to the new mesh. An edge bisection method is used. The deformed quadrilaterals represents the underlying RVE corresponding to each coarse element. 73
4.7 The procedure of the development of the fully resolved region . . 74
4.8 Solving the fully resolved region using a boundary condition based on the displacement history of the corresponding critical zone. . . 76

5.1 Different size of non-regular RVEs. The sizes are in mm. 80
5.2 Macroscopic yield surface obtained form different size of RVEs. . . 81
5.3 Macroscopic stress-strain curve. 82
5.4 The ratio of energy dissipation increases by increasing the RVE size. The average grain size is maintained constant ($l_g = 25\mu$m). 83
5.5 Macroscopic Young's modulus obtained from homogenisation of RVEs under biaxial load. 84
5.6 Relative error in the macroscopic Young's Modulus. 84
5.7 A single-notched beam under uniaxial tensile load. 85
5.8 von Mises stress distribution in the notched bar a) DNS, b) Adaptive multiscale solution. Deformation is magnified by 100. 86

5.9 The distribution of strain-gradient sensitivity $L_{\mathcal{V}}||\nabla\nabla\mathbf{u}^c||_e$ at the coarse scale, and the adaptive development of the fully resolved region. 88
5.10 Coarse mesh in the adaptive multiscale at Time step 200. Deformation is magnified by 100. 89
5.11 Variation of the external work W_{ext}, the strain energy W_{int}, and the dissipated energy D in a notched beam under a uniaxial load. 90
5.12 Capturing the crack initiation at the grain scale using adaptive multiscale method. Deformation is magnified by 100. 91
5.13 The variation of dissipated energy D versus displacement at the Neumann boundary of notched beam (Point A in Fig. 5.12). . . . 92
5.14 The variation of dissipated energy D versus crack length. 93
5.15 The load-displacement curve for the single notched beam. 93

1 Heterogeneous domain 101

Chapter 1

Introduction

For a wide class of scientific and engineering problems it is sufficient to use a single scale when developing a model. For such kinds of problems, it is assumed that at the engineering scale the material properties and constitutive laws represent the microscopic heterogeneities, without considering, explicitly, the influence of these sub-scale properties. The simplest analytical models of materials that can represent the macroscopic response have a strong phenomenological basis. Finding a simple analytical model for engineering materials requires experimental data which is costly [Nemat-Nasser and Hori, 1999; Eringen, 2001]. In fact, in many engineering designs, macroscale models cannot predict the behaviour of complex materials correctly [Menk and Bordas, 2011]. Material failure, heterogeneous materials and multiphase problems may require more information than is available at the macroscale to construct constitutive relations and obtain material properties.

Multiscale modelling are aimed at solving problems for which macroscopic considerations are insufficient. For example, multiscale modelling is applicable to problems with complex material laws that fail to be determined by macroscopic approaches, or microscopic optimisation problems, where a bridge between micro and macro is required. Because of the large size of engineering structures, these problems cannot be solved completely at the micro-level, i.e. by resolving the micro structure explicitly on the whole domain of interest. Therefore it is reasonable to retain both the macroscopic and the microscopic points of view to find a practical technique to analyse such problems.

A taxonomy for the computational multiscale methods was presented by [Gravemeier et al., 2007], highlighting the differences and similarities in computational multiscale methods. Three different ways of classifying methods from the literature are given: 1) hierarchical and concurrent methods [Suquet, 1987; Feyel and Chaboche, 2000; Kouznetsova et al., 2001], 2) "Type A" or concurrent multiscale, "Type B" or hierarchical multiscale and "Type C" or hybrid multiscale methods [Weinan, E. and Li, Xiantao and Vanden-Eijnden, 2004], 3) fluid turbulence and material modelling [Bochev et al., 2004]. Those authors also divided multiscale methods into the Variational Multiscale Methods (VMM) [Hughes, 1995] and the Heterogeneous Multiscale Methods (HMM) [E and Engquist, 2003] (see Fig. 1.1) , and compared these frameworks in different ways: application, scale separation, scale linking and number of scale levels.

Most of the strategies for hierarchical multiscale modelling rely on homogenisation, which assumes a clear separation of scale. Hierarchical multiscale is basically an application of this principle using computational power to evaluate the homogenised properties "on-the-fly". Once the scale separation is lost, one must go lower in scale, which leads to hybrid multiscale solvers.

Hierarchical multiscale based on homogenisation fails to model the regions under high strain localisation due to the lack of scale separation assumption. Therefore, in order to model fracture in a polycrystalline materials, we develop a "Type C" or hybrid multiscale method which is a combination of hierarchical and concurrent multiscale methods. In the following section, this choice will be put in the context of previous work on modelling fracture in heterogeneous materials.

1.1 Multiscale approaches for fracture modelling

In order to simulate the behaviour of composite structures, one of the most promising approaches is to model the behaviour of the material at the scale of the material heterogeneities: this is usually called micro or meso-modelling. In a second step, these fine-scale features can be transferred to the scale of the structure by averaging techniques or homogenisation on a representative volume element (RVE). In this hierarchical method, when both the macroscale prob-

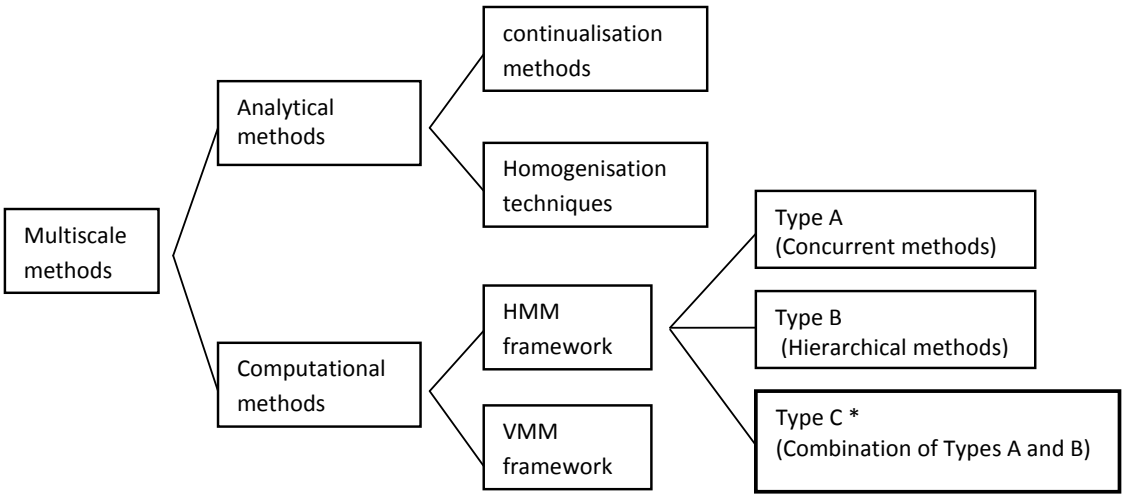

Figure 1.1: A taxonomy for multiscale methods in mechanics.

lem and local averages are obtained by the finite element method, the resulting strategy is known in the engineering community as FE^2 [Feyel and Chaboche, 2000; Runesson and Larsson, 2008; Abdulle, 2009; Geers et al., 2010]. However, in the case of fracture, these so called upscaling methods cannot be used in the vicinity of cracks, as the separation of scales necessary for their application is lost [Gitman et al., 2007]. In the literature, two techniques have been used in order to alleviate this problem: i) Non-concurrent methods, ii) Concurrent methods. The first method tries to extend the applicability of averaging techniques to fracture (e.g. [Massart et al., 2007; Alfaro et al., 2009; Verhoosel, Remmers and Gutiérrez, 2010; Nguyen et al., 2011] for special averaging techniques dedicated to established damage bands). The second makes use of a concurrent framework and attempt to detect the zone where the homogenisation fails directly at the microscale (e.g. [Kerfriden et al., 2009; Larsson and Runesson, 2011]). Although the latter approach is more general, it is " more costly" in terms of computation, and requires the development of robust adaptivity procedures [Romkes et al., 2006; Larsson and Runesson, 2011; Lloberas-Valls et al., 2012].

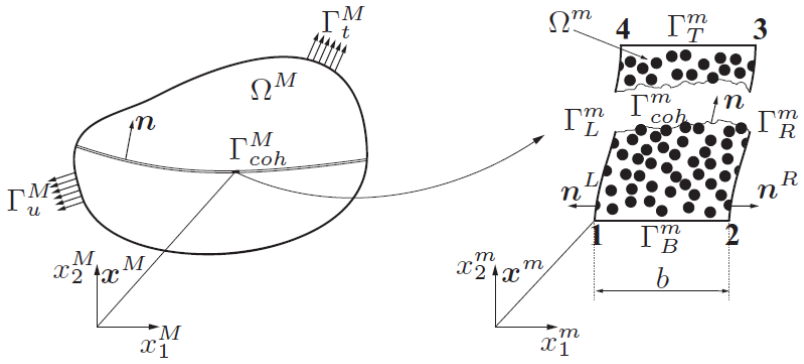

Figure 1.2: Non-concurrent multiscale for fracture. Figure from [Alfaro et al., 2009].

1.1.1 Non-concurrent multiscale approaches for fracture

In the non-concurrent mutliscale scheme for fracture modelling, a macroscopic crack is represented by e.g. cohesive interface elements, and the associated constitutive model is derived from homogenisation. In these approaches, the classical homogenisation technique is modified to obtain a homogenised behaviour of the softening regime, while the microscopic model loses stability and the scale separation assumption ceases to exist. The principle of the modified homogenisation technique is based on a decomposition of the averaging procedure into two parts: one averaging over the region of the RVE where it is in the elastic regime and a second averaging over the region that is undergoing softening. This is a modified homogenisation to get the cohesive law of the macroscopic crack from the microstructure. Increasing the width of the RVE leads to a more brittle response because the RVE stores more elastic energy but dissipates a constant amount of energy due to the constant band of localisation. The idea is to filter out the elastic part so that the energy of the cohesive crack is equated only to the energy of the part of the RVE that undergoes significant dissipation and damage localisation. In most of the existing approaches, the direction of propagation is found via macroscopic criteria, although some progresses have been achieved in the context of bottom up approach [Bosco, 2012].

As pioneer, [Massart et al., 2007] developed a computational homogenisation technique for the modelling of localisation in masonry structures. They related the traction-separation behaviour of the coarse scale damaging band to a microscopic unit cell consisting of a brick surrounded by damaging mortar at the softening regime. The onset of localisation is detected based on the appearance of negative eigenvalues of the homogenised tangent operator, and an eigenspectrum analysis of the acoustic tensor provides the orientation of the discrete band of localisation at the coarse scale.

Multiscale Aggregating Discontinuities (MAD) was proposed by [Belytschko et al., 2008]. This method aggregates the many discontinuities in the unit cell on the fine scale into a single discontinuity at the coarse scale by separating the bulk deformation from the failure deformation of a unit cell. By solving the boundary value problems of the unit cells, both the stress response for the macroscopic quadrature point, and the orientation and magnitude of the macroscopic displacement jump are obtained.

[Matous et al., 2008] proposed a multiscale approach that homogenises the complex damage evolution at the microscale to model the failure of an adhesive layer at the macroscale. In their homogenisation scheme, the height of the RVE is fixed to the thickness of the cohesive interface. In a similar approach, [Hirschberger et al., 2009] proposed a computational homogenisation procedure for a softening layer by applying an averaging technique on a continuous RVE with a height equal to that of the microscopic thickness of the cohesive layer.

In [Alfaro et al., 2009], the macroscopic behaviour of a cohesive layer was modelled by the numerically homogenised fracture response of a periodic RVE loaded under uniaxial tension. At the macroscale the thickness of cohesive layer was neglected, whilst at the microscale, it dictated the height of the RVE. They illustrated that different widths of RVEs give the same macroscopic traction-separation law. However, these methods can only be employed for problems in which the crack path is known in advance. The microscopic thickness of the cohesive crack must also be known.

[Verhoosel, Remmers, Gutiérrez and de Borst, 2010; Verhoosel, Remmers and Gutiérrez, 2010] developed a non-concurrent multiscale method to model the

nucleation and propagation of macroscopic cohesive cracks in heterogeneous microstructure based on homogenisation. The maximum principal stress of the macroscale was used to determine the nucleation as well as the propagation direction of a macroscopic cohesive segment. The microscopic model is only adopted for modelling the softening regime. In their homogenisation scheme for a cohesive crack, the direction along the crack is considered as homogeneous, so the homogenisation procedure is applied in the perpendicular direction. They emphasised that the proposed homogenisation technique should be interpreted as homogenisation applied along the cracks.

[Nguyen et al., 2011] showed the existence of the RVE for the softening regime of quasi-brittle materials with non-local continuum damage model at the microscale. In their proposed method, the averaging scheme is only applied over the band of non-local damage, and the elastic domain of the RVE is not considered for homogenisation. [Nguyen et al., 2012] implemented the softening regime homogenisation in a multiscale framework in order to model macroscopic crack propagation under cyclic loading with a treatment for macroscopic snap-back. The traction-separation law for macroscopic cohesive cracks was obtained by homogenisation of the non-local damaged band of the RVE. They determined the nucleation and the direction of macroscopic cracks by either a macroscopic criterion, (e.g. maximum hoop stress) or a microscopic criterion (i.e. the negative determinant of the homogenised stiffness matrix and eigenspectrum analysis of the acoustic tensor). However, the damaged band can only emerge in parallel with the vertical or horizontal edges of the RVE.

[Unger, 2013] developed a non-concurrent multiscale method for fracture which is based on a decomposition of the RVE energy into the energy of the damaged zone and the energy of the non-damaged zone. The macroscopic strain is also decomposed into a homogeneous strain and a crack opening part. Two microscopic models were employed: an elastic model corresponding to the non-critical macroscopic elements, and a softening model corresponding to the macroscopic cohesive crack. In order to impose the macroscopic displacement jump on the boundary of the damaged RVE, they made use of an enrichment function. A modified boundary condition technique was implemented that allows a microscopic damaged-band to emerge not only in the vertical or horizontal direction,

but in any possible direction. Similar work on the non-concurrent multiscale method for failure can be found in [Coenen et al., 2012; Bosco, 2012; Toro et al., 2013].

1.1.2 Concurrent multiscale approaches for fracture

Crack tip properties in a heterogeneous structure cannot be accurately determined by replacing the whole structure with a homogenised medium and calculating the SIF of the crack in that medium. For example, [Wang et al., 2008] proposed that the crack tip region must explicitly be retained with the actual microstructure, and at best replace the surrounding region with the homogenised medium.

The goal of concurrent multiscale fracture modelling is to take advantage of the fact that in fracture problems, only a small portion of the total domain is of interest [Buehler and Gao, 2005].

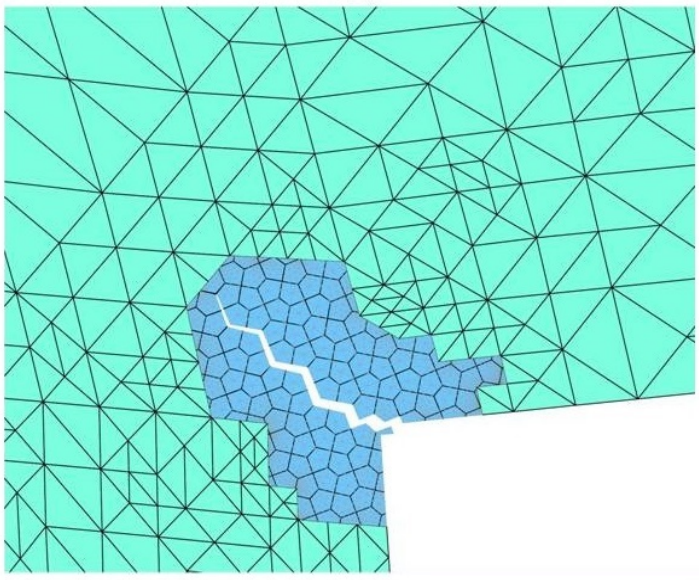

Figure 1.3: Concurrent multiscale modelling of fracture

To reach this goal, a concurrent multiscale scheme must establish a direct link between the macro and microscale without a prerequisite for scale-separation. In this scheme, both scales (or all scales) are resolved simultaneously. Information

is exchanged between the scales through their common interfaces (see Fig. 1.3). In a failure-oriented concurrent multiscale method, the main challenges are

- determining those regions which must be modelled with a microscale and those for which a macroscale model is sufficient,
- adequately modelling the coupling between the scales.

Different criteria have been employed to determine the scale of modelling in multiscale fracture problems. These criteria can be either physically oriented (for example based on the level of stress, strain or damage [Ghosh et al., 2001]) or mathematically oriented for example based on the macroscopic discretisation error inherent to the finite element approximation or the modelling error due to homogenised material properties [Zohdi et al., 1996; Ghosh et al., 2007; Temizer and Wriggers, 2011; Vernerey and Kabiri, 2012]). However, in none of failure oriented multiscale methods the scale adaptation criteria based on modelling error has been employed.

To tackle the second challenge of the failure-oriented concurrent multiscale method, several coupling techniques have been proposed in the literature in order to connect the macroscopic and the microscopic domains in a concurrent manner. These methods differ according to the physics of the problem. They include the Arlequin method [Dhia, 1998], mortar element method [Bernardi et al., 2005; Amini et al., 2009], Linear multi-point connection (or the strong coupling) [Lloberas-Valls et al., 2012]. The latter will be employed in this thesis.

[Ibrahimbegovic and Markovic, 2003] proposed a strong coupling method for modelling the inelastic behaviour of heterogeneous materials in such a way that each macroscopic element is strongly linked to its underlying microstructure. The method cannot be used for the modelling of localisation without modification.

[Hund and Ramm, 2007] proposed a superposition-based multiscale method to model localisation phenomena in non-linear materials. The solution for the local critical area is split into a macroscopic contribution and a microscopic part, while in the non-critical area the microscopic contribution is neglected. The scale adaptation is based on a strain criterion at the integration point.

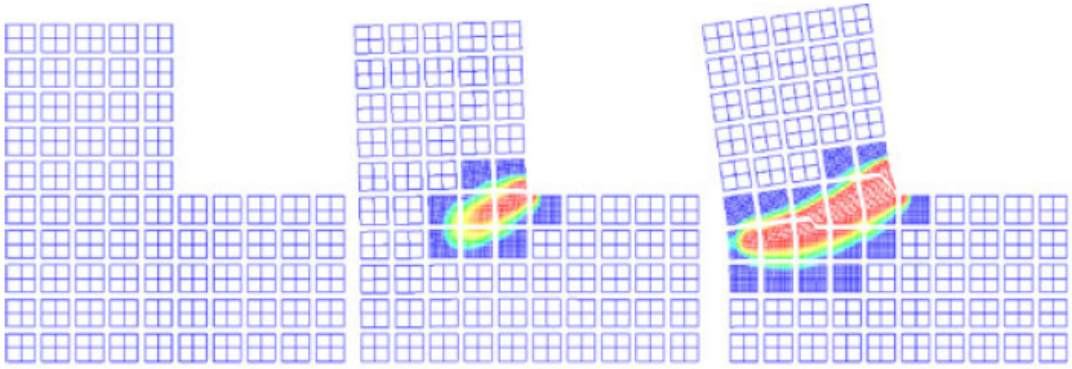

Figure 1.4: A concurrent multiscale method for modelling of fracture: There is no control on discretisation or homogenisation errors. Picture from [Lloberas-Valls et al., 2012].

[Unger and Eckardt, 2011] developed a concurrent multiscale method to model localisation in concrete. The macroscale problem is modelled by a fixed structured mesh with linear elastic material behaviour. The principal stress at the macroscale is used as an indicator for the adaptation of the microscopic model. At the microscale, the heterogeneous structure of concrete is modelled with a nonlocal continuum damage model. They investigated three different coupling methods between coarse and fine scales: the strong coupling method which provides a strong non-overlapping connection between the displacement fields of the fine mesh and coarse mesh; the mortar method which connects the fine mesh and coarse mesh through a non-overlapping interface in an average sense; and the arlequin method which connects the two meshes through overlapping domains.

[Lloberas-Valls et al., 2012] presented a hybrid multiscale method that employs both a hierarchical and a concurrent approach to capture the initiation, growth and propagation of continuum damage in a heterogeneous structure. The FE^2 method was employed to determine the coarse scale constitutive relations in the non-critical region, and a domain decomposition procedure, i.e FETI method [Farhat and Roux, 1991], was chosen as the basis of the concurrent multiscale method (see Fig. 1.4). Switching from the coarse scale to the fine scale is triggered if non-linearities is predicted in the corresponding domain of interest. Thanks to the domain decomposition technique, the global domain is split into sub-domains

for parallel computing. However, they mentioned that a mesh refinement approach is not compatible with this procedure, and therefore, dicretisation error cannot be controlled in their method. In order to simulate failure at the microsturcture a gradient-enhanced continuum damage model [Peerlings et al., 1996] was assumed.

[Ghosh and Chaudhuri, 2013] proposed a concurrent multiscale method for modeling of fracture using a meshfree method. In their method the fine scale region is not adaptive, and it is chosen once at the beginning of simulation.

[Larsson and Runesson, 2011] proposed a seamless scale-bridging technique that turns from a hierarchical multiscale strategy (classical homogenisation) to a concurrent multiscale strategy at the critical region through a four-level procedure. In the first level, the size of the coarse element is much larger that the size of the RVE which means that the essential assumption of homogenisation is fulfilled, so the classical homogenisation is carried out (fully scale separation). In the second level, the size of the coarse element is slightly larger than the size of the RVE, then the local microscale problems are solved on Quadrature Subscale Volume Elements (QSVE) as part of the integration scheme at the coarse scale (near-complete scale separation). In the third level, where the size of the coarse element is almost the same or slightly less than the size of the RVE, the microscale problem is solved on a Subscale Volume Element (SVE) that is identical to the coarse element (partial scale separation). Finally, if the size of the coarse element is smaller than the size of the RVE, then there is no scale separation, and the problem is fully resolved at the fine scale. In their work, the coarse mesh was adaptively refined by an error estimator technique.

[Ghosh et al., 2001] proposed an adaptive concurrent multiscale method to address the modelling error due to homogenisation. The macroscale mesh was adaptively refined based on either a local estimate of the error or based on the solution gradient. Two reasons were given for the coarse mesh refinement 1) to identify and reduce a chosen 'error measure' in the macroscale finite element model, 2) to detect the development of critical regions. They divided the domain of the problem into three subdomains (see Fig. 1.5): Level-0 as a non-

critical macroscopic model, Level-1 as a critical but still a macroscopic model, and Level-2 as a critical microscopic model. The level-1 subdomains are modelled at the macroscale but the development of damage and instabilities in the RVE is monitored by using the homogenisation technique. The coarse mesh refinement by h-adaptation continues for this level. This level is identified by a criterion based on locally high gradients of macroscopic variables e.g. stresses, strains or strain energy. The level-2 subdomains are critical regions where the microscopic structure is fully simulated by the Voronoi cell finite element model. In their work, the extended microstructure for the level-2 subdomain is generated in a way that fits the macroscopic elements. The transition criterion from level-1 to level-2 is based on the evolution of microscopic damage. The authors called their concurrent method a global-local method. The schematic of the component of the concurrent multiscale method proposed by [Ghosh et al., 2001] is shown in Fig. 1.5. In [Raghavan et al., 2004], both h- and p-adaptivity are used to re-

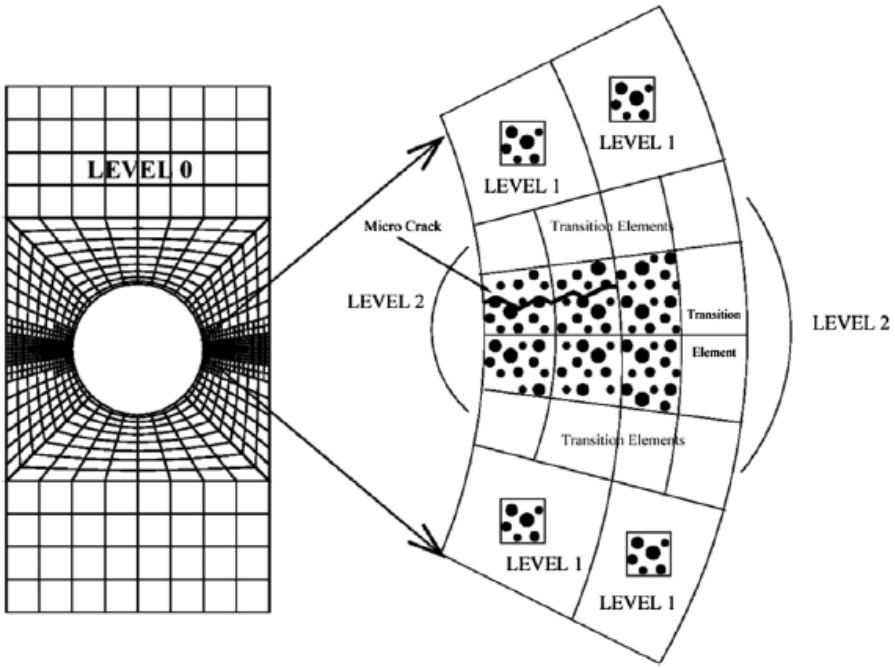

Figure 1.5: *"The top-down multi-level model showing components of concurrent coupling, viz. continuum level-0, level-1 of asymptotic homogenization and level-2 of micromechanical analysis"* [Ghosh et al., 2007].

duce the discretisation error in the macroscopic computations as an extension to [Ghosh et al., 2001]. [Ghosh et al., 2007] made use of a different criterion for transition from the level-1 subdomain to the level-2 subdomain. The proposed criterion was based on a scale ratio which is the ratio of the characteristic length of the level-2 elements to the size of the RVE. In their fibre reinforced composite model, damage only appears at the interface of matrix and inclusion, and cannot defuse into the matrix. In another words, damage are not allowed to propagate and a strain localisation band does not appear in the structure.

[Vernerey and Kabiri, 2012] proposed a concurrent adaptive multiscale method for elasticity which the error in the coarse scale discretization and the modelling error due to homogenisation are controlled. The coarse mesh was adaptively refined to reduce the discretization error. When the size of coarse elements becomes comparable to that of the microstructure (a critical size) they were replaced by the underlying microstructure. They derived a criterion for the validation of the first order numerical homogenisation based on a comparison between elastic energy retained in the first displacement gradient and those retained in the second displacement gradient. The homogenisation technique is valid while the elastic energy from second displacement gradient is sufficiently small in comparison to the elastic energy of the first displacement gradient. The local error in the macroscopic strain field was used to find a closed-form relation between the critical size of coarse elements, desirable discretization and homogenisation errors and the size of RVE.

According to this literature review, those concurrent multiscale methods that address the discretisation and homogenisation errors are not dealing with fracture and failure phenomena, e.g. [Ibrahimbegovic and Markovic, 2003; Ghosh et al., 2007; Larsson and Runesson, 2011; Temizer and Wriggers, 2011; Vernerey and Kabiri, 2012]. Figure 1.6 shows an algorithm for the scale adaptation proposed by [Temizer and Wriggers, 2011] which the microscopic structure appears at the coarse scale based on the level of homogenisation error, and the coarse mesh is refined based on the level of discretisation error. However this method does not model fracture in the structure. A few works can be found in the literature that are designed for the modelling of fracture[Unger and Eckardt, 2011; Lloberas-

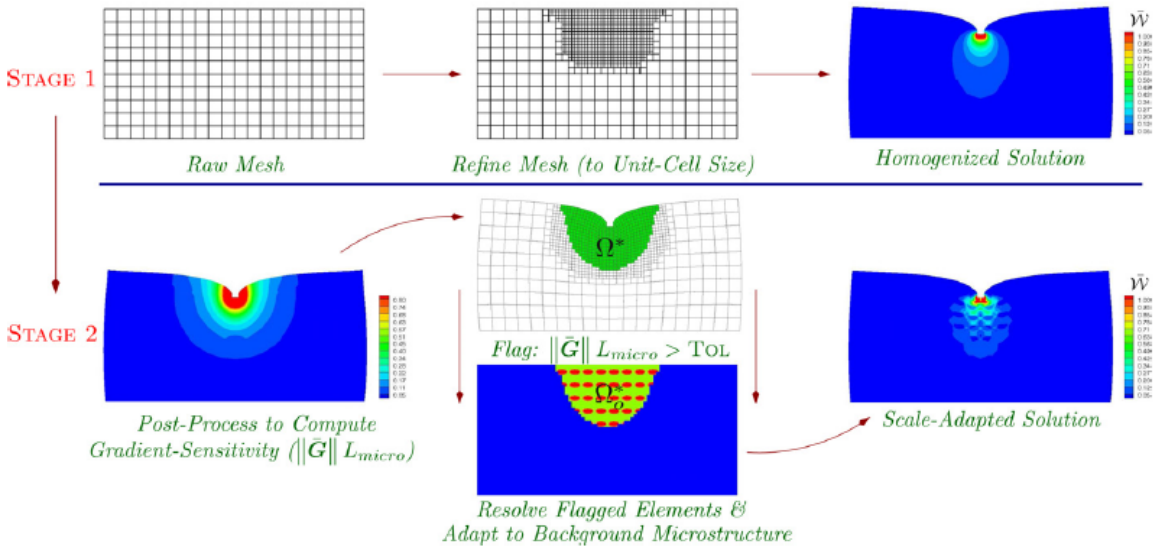

Figure 1.6: A concurrent multiscale method: The homogenisation error is controlled by adapting the microscale, and discretisation error is controlled by the coarse mesh refinement. Picture from [Temizer and Wriggers, 2011].

Valls et al., 2012; Talebi et al., 2013; Ghosh and Chaudhuri, 2013]. These methods usually have a fixed macroscopic mesh without any control on the modelling or discretisation errors (For example, see Fig. 1.4). In this thesis, a concurrent multiscale method will be presented that is designed to model crack propagation through an adaptive expansion of the microscopic region together with a mesh refinement procedure to control the discretisation error at the coarse mesh. The unstructured macroscopic mesh is an advantageous that allow us to model non-regular shapes.

1.2 Proposed multiscale method

In this work, we propose an adaptive hybrid multiscale method for modelling fracture in a heterogeneous material composed of orthotropic grains with cohesive interfaces between grains. Instead of a direct solver the FE^2 method, derived from the homogenisation technique, is employed to compute the effective behaviour of the heterogeneous microscopic medium at a much coarser scale in the non-critical

region where the modelling error due to the homogenisation is still low. The coarse scale is discretised with non-structured triangular finite elements, and adaptive mesh refinement is used to control the discretization error. While the coarse mesh refinement retains the discretization error at a certain level, the modelling error increases due to the fact that the finer the coarse elements, the less the scale separation assumption is fulfilled, which is a key issue for homogenisation. The accuracy of homogenisation is examined by measuring the second gradient of displacement which is ignored in the first order homogenisation. A critical zone emerges when the second displacement gradient reaches the critical value, or if the underlying RVE (representative volume element of microstructure) of the element loses stability due to localisation. Thereafter, a zoom-in process is triggered to replace the corresponding coarse elements of the critical zone with a high resolution microscale mesh and gluing it to the coarse scale mesh through a strong coupling technique using Lagrange multipliers. The high resolution region can gradually be extended to the newly emerged critical zones. A local arc-length technique is adopted to control the opening of microscopic cohesive cracks.

1.3 Outline

In Chapter 2, the constitutive model for a polycrystalline material will be discussed. Grains are modelled as orthotropic with cohesive interfaces. A thermodynamically consistent damage model is presented for simulation of the cohesive interface between the grains. The finite element method with linear triangular element and 4-node cohesive elements for the grains and grain boundaries will be detailed.

In Chapter 3, hierarchical and concurrent multiscale methods will be introduced. The modelling of polycrystalline materials with the FE^2 method will be explained. Then, a non-overlapping domain decomposition method for non-conforming meshes will be introduced that allows us to model localisation in critical regions where the FE^2 method is not valid. A strong coupling technique will be employed to connect the displacement field at the interface of the coarse and fine meshes in the domain decomposition method.

In Chapter 4, the algorithmic aspect of the proposed adaptive multiscale

method will be explained. In order to follow load-displacement paths, a robust local arc-length technique will be proposed. The coarse mesh refinement based on Zinkiewicz-Zhu error estimator will be discussed, and introduction of fully resolved microstructure in the critical regions will be explained.

Finally, in Chapter 5, some test cases will be simulated with adaptive multi-scale method and the results will be verified by direct numerical solution of the problems.

Chapter 2

Constitutive Modelling of Polycrystalline Materials

2.1 Introduction

This chapter deals with the numerical modelling of brittle fracture in polycrystalline materials. Brittle failure in such materials is usually due to inter-granular fracture. In an inter-granular fracture, cracks can grow at the interfaces between the grains, while in a trans-granular fracture, cracks propagate into the grains and display a more ductile response due to the plastic behaviour of the grains. The brittleness of inter-granular fracture is caused by the elastic behaviour of bulk grains which release more energy than the amount of energy needed for dissipation at the inter-granular fracture. As a matter of fact, the more energy released from (work done by) the elastic grains, the faster the cracks propagate and the more brittle the response is expected to be. A vast amount of research on the failure of polycrystalline materials has been done, e.g. experimental studies can be found in [Anil et al., 1978; Bellante and Kahn, 2005; Luo et al., 2007; Carolan et al., 2013], and analytical/computational modelling can be found in [Sakai et al., 1983; Zavattieri and Espinosa, 2001; Sukumar et al., 2003; Rollett et al., 2004; Sfantos and Aliabadi, 2007; Verhoosel and Gutiérrez, 2009; Paggi and Wriggers, 2011]. Researchers observed that inter-granular cracks are the main cause of crack initiation and propagation at the microscale which leads to

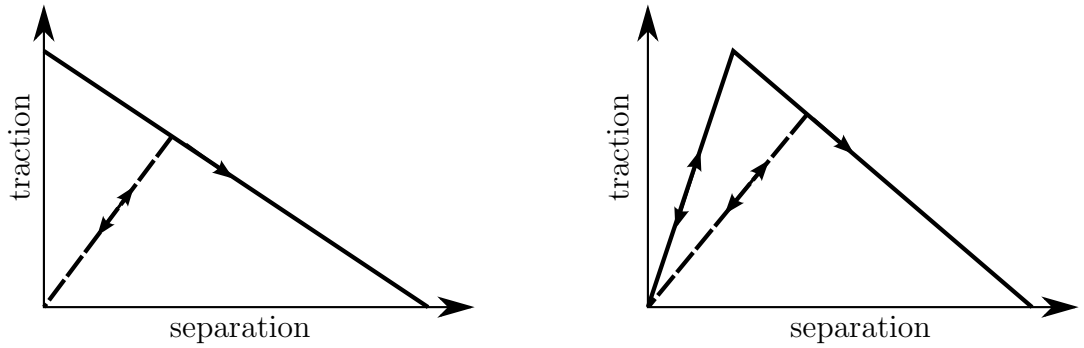

Initially rigid cohesive law

bi-linear cohesive law

Figure 2.1: Two simple traction-separation laws for cohesive interface modelling.

a brittle failure of the structure from a macroscopic point of view [Nemat-Nasser and Hori, 1999; Wei, 2004]. In computational modelling, the grain interfaces are mostly modelled by zero-thickness cohesive elements which are usually based on a traction-separation relationship rather than a stress-strain relationship. On a cohesive interface, the traction at each point is considered as a function of the gap between the two sides of the crack (or displacement jump). Several mathematical models for traction-separation relationships have been proposed in the literature to represent failure in different materials, e.g. laminated composites [Allix and Corigliano, 1996], concretes [Wang, 2007] and polycrystalline materials [Sfantos and Aliabadi, 2007]. The two most simple models of the traction-separation laws are the initially rigid and bi-linear functions, shown in Figure 2.1, for a tensile load in a one-dimensional cohesive crack [Ortiz and Pandolfi, 1999; Nguyen et al., 2001]. [Tvergaard and Hutchinson, 1992, 1993] proposed a cohesive interface law for modelling fracture in ductile materials. They showed that in a ductile material, the macroscopic work done by a crack is much larger that the energy dissipated at the crack tip. Another noteworthy cohesive interface model which has been widely used for the modelling of failure in polycrystalline materials is the potential-based cohesive law proposed by [Xu and Needleman, 1994]. It has been employed extensively for modelling fracture in brittle materials.

[Zavattieri and Espinosa, 2001] studied dynamic fracture in polycrystalline materials using a linear cohesive interface law between the grains. [Espinosa and Zavattieri, 2003] carried out an intensive investigation on the effect of different cohesive laws on the dynamic fracture of polycrystalline materials. A finite element simulation of inter-granular fracture in polycrystalline materials was performed by [Shabir et al., 2011], in order to understand the dependency of the crack path on microstructural parameters and the finite element mesh size. They used a zero thickness cohesive interface law adopted from [Xu and Needleman, 1994] for the physical modelling of the grain boundaries which was modelled computationally by a generalized finite element method (GFEM/XFEM).

[Wei, 2004] developed a computational tool for an elasto-plastic interface model coupled with a crystal-plasticity model for the grain interior to investigate the deformation and fracture response of nanocrystalline nickel. They discussed the effect of the grain size on the macroscopic stress-strain curve, and it was concluded that the nanocrystalline nickel showed a brittle response when a high yield strength of the grain interiors and a relatively weaker strength of the interfaces is assumed. This means that inter-granular fracture can be assumed if grain boundaries are weaker than grain bodies. For a comprehensive overview on cohesive interface models see [Brocks et al., 2003; Mosler, 2007].

Some novel techniques have also been developed for modelling grain boundaries in which no cohesive zone model has been employed .

[Sukumar et al., 2003] modelled inter-granular and trans-granular crack propagation in a polycrystalline microstructure by using the extended finite element method. They considered one fracture toughness for the grain boundary, G_c^{gb}, and a different fracture toughness for the inside of the grains, G_c^i. Their method can be used for the fracture analysis of functionally graded materials by varying the toughness ratio G_c^{gb}/G_c^i in space. Notably, their model is based on linear fracture mechanics which is much cheaper than the cohesive interface model. [Paggi and Wriggers, 2011] studied inter-granular fracture using a non-local cohesive interface model with non-zero thickness interfaces. In their model, the thickness of the interfaces depend on the grain size. An atomistic approach was proposed by [Glaessgen et al., 2006] to study grain boundary fracture in polycrystalline aluminium. The constitutive model of the traction-separation relationship at the

cohesive interfaces was characterised by a molecular-dynamics simulation of the physical behaviour at the nanoscale. [Abdollahi and Arias, 2014] simulated the fracture processes of ferroelectric polycrystals in three dimensions using a phase-field model. In their model, the grain boundaries, cracks and the ferroelectric domain walls are represented in a diffuse way by three phase-fields, in order to avoid the difficulty of tracking the interfaces in three dimensions.

Recently, [Mosler and Scheider, 2011] proposed a thermodynamically consistent cohesive model based on an energy potential which, in contrast to the Xu-Needleman model, depends on some internal variables related to the deformation history of the interface in addition to the current displacement jump. Their model is based on the Helmholtz energy which is separated into different parts corresponding to different failure modes by applying the Coleman and Noll procedure. In their model, the dissipation of energy is related to an internal variable called the damage parameter, in accordance with the second law of thermodynamics. [Dimitri et al., 2014] investigated the physical inconsistencies between stresses and dissipated energy in some widely used cohesive models, e.g. Xu-Needleman and bi-linear models, and compared the results with thermodynamically consistent models. Their analyses revealed that all models, except the thermodynamically consistent model, present energetic inconsistencies due to incomplete dissipations or non-monotonic variations of the total work of separation.

Due to this fact, in this thesis, a thermodynamically consistent cohesive interface model based on [Mosler and Scheider, 2011] is adapted to simulate inter-granular fracture. To the best knowledge of the author, this is the first time that a thermodynamically consistent cohesive interface model is employed for the modelling of grain boundaries in a polycrystalline microstructure. Two-dimensional grains are modelled as linear elastic materials with cohesive interfaces between the grains. Only inter-granular fracture is considered, therefore cracks are not allowed to pass through the bulk grains. In the following, the constitutive equations for bulk grains and grain boundaries will be explained. Figure 2.2 shows a domain Ω occupied by a structure consisting of randomly distributed orthotropic grains undergoing quasi-static small perturbations.

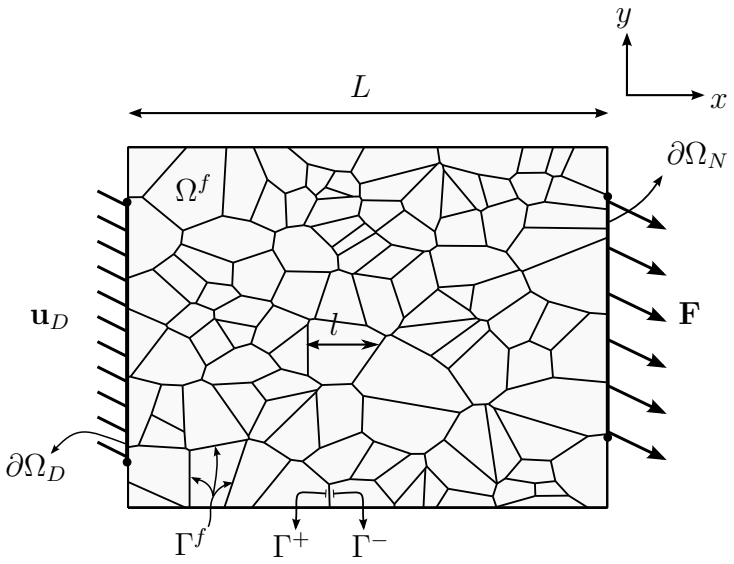

Figure 2.2: Microscale problem

2.2 Microstructure model formulation

To start with, a boundary value problem of a structure where the polycrystalline material is represented explicitly is defined.

Given the displacement boundary condition $\mathbf{u}_D : \partial\Omega_D \to \mathbb{R}^2$ and the traction boundary condition $\mathbf{F} : \partial\Omega_N \to \mathbb{R}^2$, find $\mathbf{u}^f : \Omega \to \mathbb{R}^2$ such that, $\forall \delta\mathbf{u}^f \in \mathcal{U}_0$

$$\delta\Pi^f(\mathbf{u}^f, \delta\mathbf{u}^f) = \int_{\Omega^f \setminus \Gamma^f} \boldsymbol{\sigma}^f : \boldsymbol{\varepsilon}^f(\delta\mathbf{u}^f)\ \mathrm{d}\Omega + \int_{\Gamma^f} \mathbf{T}^f \cdot [\![\delta\mathbf{u}^f]\!]\ \mathrm{d}\Gamma - \int_{\partial\Omega_N} \mathbf{F} \cdot \delta\mathbf{u}^f\ \mathrm{d}\Gamma = 0 \tag{2.1}$$

$$(\boldsymbol{\sigma}^f \cdot \mathbf{n})\,|_{\mathbf{x}\in\Gamma^+} = -\,(\boldsymbol{\sigma}^f \cdot \mathbf{n})\,|_{\mathbf{x}\in\Gamma^-} = \mathbf{T}^f([\![\mathbf{u}^f]\!])\,|_{\mathbf{x}\in\Gamma^f}\ . \tag{2.2}$$

The superscript f indicate that the variables are at the fine scale. The vector $\mathbf{n}$ is a unit vector normal to the cohesive interface (see Fig. 2.7). $\delta\Pi^f$ is the virtual work, $\mathbf{u}^f \in \mathcal{U}$ is displacement field and $\delta\mathbf{u}^f \in \mathcal{U}_0$ is an arbitrary virtual displacement field. $\mathcal{U}$ and $\mathcal{U}_0$ are collection of trial, $\mathbf{u}^f$, and test functions, $\delta\mathbf{u}^f$

respectively, which can be defined by

$$\mathcal{U} = \{\mathbf{u}|\mathbf{u} \in H^1(\Omega^f \setminus \Gamma^f), \mathbf{u}|_{\partial\Omega_D} = \mathbf{u}_D\} \tag{2.3}$$

$$\mathcal{U}_0 = \{\delta\mathbf{u}|\delta\mathbf{u} \in H^1(\Omega^f \setminus \Gamma^f), \delta\mathbf{u}|_{\partial\Omega_D} = \mathbf{0}\} \tag{2.4}$$

where $H^1(\Omega^f \setminus \Gamma^f)$ is the Sobolev space of degree one for inside the grains not at the interfaces.

The Cauchy stress tensor, the strain tensor at the fine scale are $\boldsymbol{\sigma}^f$ and $\boldsymbol{\varepsilon}^f$, and the traction and displacement jump on the interfaces of grains, Γ^f, are denoted by $\mathbf{T}^f$ and $[\![\mathbf{u}^f]\!]$ respectively. Figure 2.7 displays the displacement jump $[\![\tilde{\mathbf{u}}]\!]$ as differences between the displacement of two slides of an interface. The microscopic grains are orthotropic material. The constitutive relationship for the grains is given by Hooke's law:

$$\boldsymbol{\sigma}^f_{|\mathbf{x},t} = \mathbb{C}^f_{|\mathbf{x}} : \boldsymbol{\varepsilon}^f(\mathbf{u}^f_{|\mathbf{x},t}), \quad \text{in } \Omega^f \setminus \Gamma^f, \tag{2.5}$$

or in Voigt's form the constitutive equation is given by:

$$\boldsymbol{\sigma}^f_{|\mathbf{x},t} = \mathbf{C}^f_{|\mathbf{x}}\boldsymbol{\varepsilon}^f(\mathbf{u}^f_{|\mathbf{x},t}), \quad \forall\mathbf{x} \in \Omega^f \setminus \Gamma^f, \tag{2.6}$$

where $\mathbb{C}^f$ is the fourth order stiffness tensor, and $\mathbf{C}^f$ is a matrix contains the constant elastic stiffness moduli of the grains. Note that the tensor form of stress and strain are shown by the same notation as used for their vector form since they can be distinguished in context. The constitutive relationship for the interface between grains is based on a cohesive interface model given by:

$$\delta\mathbf{T}^f(\mathbf{x}) = \mathbf{K}_{dT}\delta[\![\mathbf{u}^f(\mathbf{x})]\!], \quad \text{on } \Gamma^f, \tag{2.7}$$

where $\mathbf{K}_{dT}$ is the tangent stiffness matrix. In Section 2.3.2 the tangent stiffness matrix $\mathbf{K}_{dT}$ will be derived as a thermodynamically consistent function of the history of the displacement jump $[\![\mathbf{u}^f]\!]$ on the interface of the grains.

2.3 Microscopic constitutive equations

2.3.1 Bulk Grain constitutive law

The stiffness matrix for a 2D orthotropic grain, used in constitutive equation (2.6), can be written in Voigt form:

$$\tilde{\mathbf{C}}^f = \begin{bmatrix} C_{11} & C_{12} & 0 \\ C_{21} & C_{22} & 0 \\ 0 & 0 & C_{66} \end{bmatrix}, \tag{2.8}$$

where C_{ij} are elastic constants and the subscripts 1 and 2 refer to the material principal coordinates (see Fig. 2.3). To obtain the stiffness matrix in the global coordinate system, the following matrix transformation is employed:

$$\mathbf{C}^f = \mathbf{T}_\sigma^{-1} \tilde{\mathbf{C}}^f \mathbf{T}_\varepsilon \tag{2.9}$$

where the transformation matrices are given by

$$\mathbf{T}_\varepsilon^T = \mathbf{T}_\sigma^{-1} = \begin{bmatrix} \cos^2\theta & \sin^2\theta & -\sin 2\theta \\ \sin^2\theta & \cos^2\theta & \sin 2\theta \\ 0.5\sin 2\theta & -0.5\sin 2\theta & \cos 2\theta \end{bmatrix}, \tag{2.10}$$

Figure 2.3 illustrates θ, which is the angle between the material coordinate system, $(1, 2)$, and the global coordinate system, (x, y).

2.3.2 Cohesive interface model for grain boundaries

The potential failure of the interface between adjacent grains is described by a thermodynamically consistent cohesive model in the local coordinate system $(\tilde{x}, \tilde{y})$ (see Fig. 2.3 and 2.7). A material point at the cohesive interfaces is considered as the thermodynamic system. The variation of temperature and heat conduction are neglected due to isothermal and homogeneous temperature assumptions, respectively.

The first law of thermodynamics states that the variation of internal surface energy density $\dot{U}$ is equal to the work done per unit surface of interface, $\dot{W}$, plus

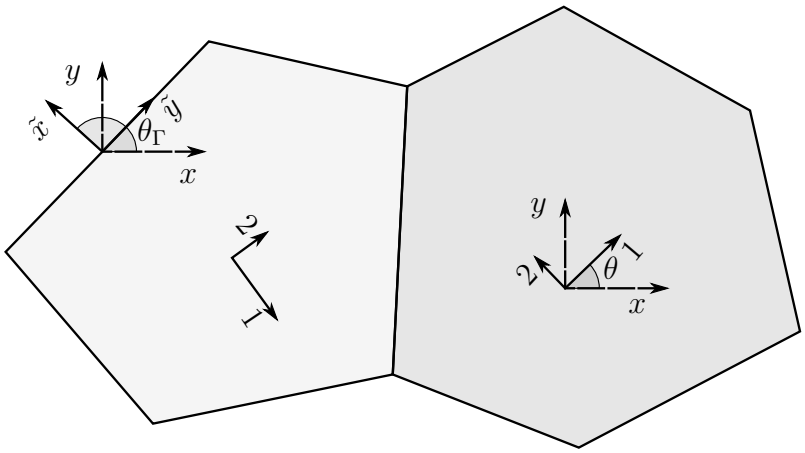

Figure 2.3: Local coordinates on the boundary of a grain $(\tilde{x}, \tilde{y})$, Local coordinates on the principal direction of the orthotropic grain $(1, 2)$, and global coordinate (x, y).

the rate of heat provided to the system $\dot{Q}$:

$$\dot{U} = \dot{W} + \dot{Q}, \tag{2.11}$$

where the dot denotes the total derivative with respect to time, $\dot{\square} = \frac{\partial \square}{\partial t}$. The second law of thermodynamics for a fracture surface states that the variation in surface entropy density $\dot{S}$ is always greater than or equal to the change in surface entropy density caused by heat introduced to the system:

$$\dot{S} \geq \frac{\dot{Q}}{\Theta}, \tag{2.12}$$

where Θ is the absolute temperature. An internal heat source due to dissipation leads to the inequality in Eq. (2.12). The rate of surface dissipation density is therefore given by [Buehler, 2008]

$$\dot{D} = \Theta \dot{S} - \dot{Q} \geq 0, \tag{2.13}$$

According to the first law of thermodynamics, $\dot{Q} = \dot{U} - \dot{W}$, so we can write

$$\dot{D} = \dot{W} - \dot{\Psi} \geq 0, \tag{2.14}$$

The term $\Psi = U - \Theta S$ is called the free energy, or Helmholtz energy which is "the maximum internal capacity of the system that can do work" [Buehler, 2008]. For a cohesive interface in which the material is degraded, the free energy can be defined by a set of functions that are related to some internal variables and the displacement jump $\Psi = \Psi(\llbracket \tilde{\mathbf{u}}^f \rrbracket, \mathbf{d})$. For notational simplicity, the superscript f is henceforth dropped in this Section. Only one scalar parameter d is considered to indicate the level of damage in the interface. The variation of the work and free energy can be written as

$$\dot{W} = \tilde{\mathbf{T}} \cdot \llbracket \dot{\tilde{\mathbf{u}}} \rrbracket, \tag{2.15}$$

$$\dot{\Psi} = \frac{\partial \Psi}{\partial \llbracket \tilde{\mathbf{u}} \rrbracket} \cdot \llbracket \dot{\tilde{\mathbf{u}}} \rrbracket + \frac{\partial \Psi}{\partial d} \dot{d}. \tag{2.16}$$

where $\tilde{\mathbf{T}}$ and $\llbracket \tilde{\mathbf{u}} \rrbracket$ are the traction and the displacement jump in the local coordinate at the cohesive interface, respectively. Consequently, by substituting Eqs. (2.15) and (2.16) into Eq. (2.14) the dissipation rate is given by

$$\dot{D} = \tilde{\mathbf{T}} \cdot \llbracket \dot{\tilde{\mathbf{u}}} \rrbracket - \frac{\partial \Psi}{\partial \llbracket \tilde{\mathbf{u}} \rrbracket} \cdot \llbracket \dot{\tilde{\mathbf{u}}} \rrbracket - \frac{\partial \Psi}{\partial d} \dot{d} \geq 0 \tag{2.17}$$

For any rate of displacement jump $\llbracket \dot{\tilde{\mathbf{u}}} \rrbracket$ in the unloading regime, the dissipation rate and variation of damage are zero, which gives rise to

$$\tilde{\mathbf{T}} = \frac{\partial \Psi(\llbracket \tilde{\mathbf{u}} \rrbracket, d)}{\partial \llbracket \tilde{\mathbf{u}} \rrbracket}, \tag{2.18}$$

In another words, if there is no change in the damage state of the interface, then the change in the dissipation must be zero, which yields the state equation

$$\dot{D} = Y \dot{d} \geq 0, \quad \text{where } Y = -\frac{\partial \Psi(\llbracket \tilde{\mathbf{u}} \rrbracket, d)}{\partial d} \tag{2.19}$$

Y is called thermodynamic force or damage energy release rate. Usually in the literature, the free energy function is defined by separation of the variables which is valid for isotropic damage [Lemaitre and Chaboche, 1994]:

$$\Psi(\llbracket \tilde{\mathbf{u}} \rrbracket, d) = \phi(d) \Psi_0 \left(\llbracket \tilde{\mathbf{u}} \rrbracket \right). \tag{2.20}$$

The damage function is usually chosen as $\phi(d) = 1 - d$, where $d \in [0, 1]$ indicates the level of damage in the interface. Ψ_0 is the energy for an undamaged elastic interface that is defined by $\Psi_0 = 0.5[\![\tilde{\mathbf{u}}]\!]^T \tilde{\mathbf{K}}_0 [\![\tilde{\mathbf{u}}]\!]$, where $\tilde{\mathbf{K}}_0$ is the original (initial) stiffness of the interface. Therefore, we have

$$\tilde{\mathbf{T}} = \phi(d) \frac{\partial \Psi_0([\![\tilde{\mathbf{u}}]\!])}{\partial [\![\tilde{\mathbf{u}}]\!]} = (1 - d) \tilde{\mathbf{K}}_0 [\![\tilde{\mathbf{u}}]\!], \tag{2.21}$$

$$Y = -\frac{\partial \phi(d)}{\partial d} \Psi_0([\![\tilde{\mathbf{u}}]\!]) = \frac{1}{2} [\![\tilde{\mathbf{u}}]\!]^T \tilde{\mathbf{K}}_0 [\![\tilde{\mathbf{u}}]\!]. \tag{2.22}$$

Now, we need to evaluate the damage parameter d. According to Eq. $(2.19)_1$, in order to fulfil the second law of thermodynamics, the damage parameter d must increase monotonically since the thermodynamic force is always non-negative (see Eq. (2.22)). Several damage evolution laws have been proposed in literature.

Different choices of damage evolution lead to different traction-separation laws, although [Mosler and Scheider, 2011] have shown that the evolution law does show intense effect on the overall structural response in their example. We choose a power-law damage evolution for our model:

$$d(\kappa) = \begin{cases} 0 & \kappa < \kappa_{\text{ini}} \\ 1 - \left(\frac{\kappa_{\text{ful}} - \kappa}{\kappa_{\text{ful}} - \kappa_{\text{ini}}} \right)^n & \kappa_{\text{ini}} < \kappa < \kappa_{\text{ful}} \\ 1 & \kappa > \kappa_{\text{ful}} \end{cases} \tag{2.23}$$

where n is a material variable. κ_{ini} and κ_{ful} are the thresholds of the internal variable κ that are associated with the initiation and the fully damaged conditions of the interface crack respectively. For time $t + \delta t$, κ is given by:

$$\kappa(t + \delta t) = \max\left(\kappa(t); u_{\text{eff}}\right), \quad u_{\text{eff}} = \left\| \begin{array}{c} [\![\tilde{u}_n]\!] \mathcal{H}([\![\tilde{u}_n]\!]) \\ a_t [\![\tilde{u}_t]\!] \end{array} \right\|, \tag{2.24}$$

where $[\![\tilde{u}_n]\!]$ and $[\![\tilde{u}_t]\!]$ are the normal and tangential component of the displacement jump $[\![\tilde{\mathbf{u}}]\!]$.The coefficient $a_t > 0$ controls the effect of shear jump on the damage parameter, and in this study $a_t = 1$. The function 'max' does not allow κ to decrease, and the Heaviside function $\mathcal{H}([\![\tilde{u}_n]\!])$ prevents the negative jump in normal direction $[\![\tilde{u}_n]\!] < 0$ (associated with compression mode) from having an influence on the damage variable. Figure 2.4 shows a schematic profile for the

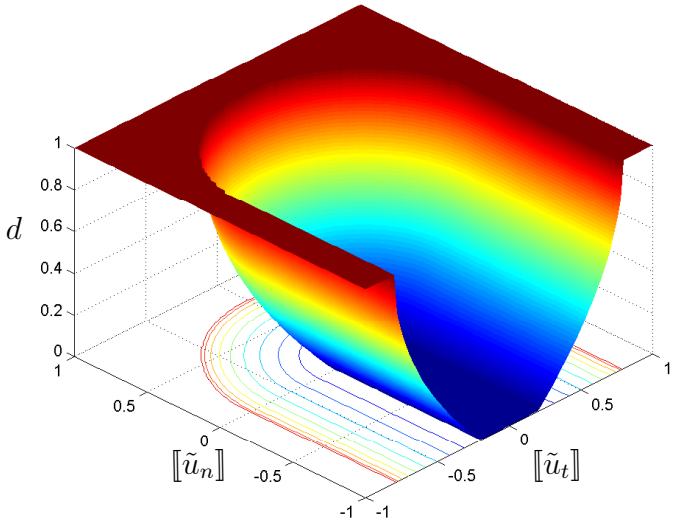

Figure 2.4: A schematic illustration of a damage evolution function based on Eqs. (2.23) and (2.24). In this figure, $\kappa_{\text{ini}} = 0.2$, $\kappa_{\text{full}} = 0.8$ and $n = 0.5$.

damage parameter d. Due to a lack of precise knowledge, we assume that the critical fracture energy of modes I and II and the maximum tensile and shear strengths are equal ($G_{Ic} = G_{IIc}$ and $\sigma_{\max} = \tau_{\max}$). The internal variable threshold κ_{ini} assumed to be zero. The parameters introduced in the damage evolution law, Eq. (2.23), can be evaluated by the following equations:

$$G_{Ic} = \int_0^{[\![u]\!]_{\text{full}}} \tilde{T}_n \, \mathrm{d}[\![\tilde{u}_n]\!], \tag{2.25}$$

$$\sigma_{\max} = \left\{ \tilde{T}_n([\![\tilde{u}_n]\!]) \,\middle|\, \frac{\mathrm{d}\tilde{T}_n}{\mathrm{d}[\![\tilde{u}_n]\!]} = 0 \right\}. \tag{2.26}$$

Equation (2.25) states that the fracture energy equals to the total work of external load that leads to a fully opened cohesive interface ($[\![\tilde{u}_n]\!] = [\![u]\!]_{\text{full}}$), and Eq. (2.26) states that the maximum normal stress occurs at the stationary point of the traction-separation law. In order to follow the loading path of the traction-separation curve, it is assumed that the normal jump along the interface monotonically increases. Thus we are allowed to use the normal jump directly in the

equation of damage evolution (2.23). Finally by solving Eq. (2.25) and (2.26) we find that:

$$\kappa_{\text{full}} = [\![u]\!]_{\text{full}} = \alpha \frac{G_{Ic}}{\sigma_{\max}}, \quad \alpha = (n+2)\left(\frac{n}{n+1}\right)^{n} \tag{2.27}$$

$$k_n = k_t = \beta \frac{\sigma_{\max}^2}{G_{Ic}}, \quad \beta = \frac{(n+1)}{(n+2)}\left(\frac{n+1}{n}\right)^{2n} \tag{2.28}$$

where the original stiffness of cohesive interface in normal and tangential directions, k_n and k_t, are assumed to be equal. The variations of α and β versus n are shown in Fig. 2.5. β is limited to $\beta \in (0, \exp(2))$, which means the stiffness coefficients are bound between $0.5\frac{\sigma_{\max}^2}{G_{Ic}} < k_n = k_t < \exp(2)\frac{\sigma_{\max}^2}{G_{Ic}}$. In the rest of the thesis $n = 0.5$. The influence of n on the traction-separation law and overall response of structure still needs to be studied, however this is beyond the scope of this thesis, where we assume that a material model is available and develop general tools able to rely on advances in such material models.

Inspired by [Allix and Corigliano, 1996], the traction-separation relationship and the stiffness matrix of the cohesive interface is modified to give a non-damageable stiffness in compression loading:

$$\tilde{\mathbf{T}} = \tilde{\mathbf{K}}_d [\![\tilde{\mathbf{u}}^f]\!] \quad \text{where} \quad \tilde{\mathbf{K}}_d = \begin{bmatrix} k_n^+ (1-d)\, \mathcal{H}([\![\tilde{u}_n^f]\!]) + k_n^- \mathcal{H}(-[\![\tilde{u}_n^f]\!]) & 0 \\ 0 & k_t(1-d) \end{bmatrix}. \tag{2.29}$$

The subscript t refers to the tangential direction of the interface and n refers to the normal to the interface (See Fig. 2.7). k_t and k_n are original interface stiffness with dimension of force over length cubed. In order to avoid the penetration of grains into each other, the original interface stiffness for the closing mode is chosen to be much larger than the original interface stiffness for the opening mode, $k_n^-/k_n^+ > 1$. It is noted that a very large value of k_n^- causes ill-conditioning of the stiffness matrix in finite element procedure. In this study, $k_n^-/k_n^+ = 100$. The Heaviside function $\mathcal{H}$ does not allow the damage parameter to influence the stiffness of the cohesive crack in compression mode. Figure 2.6 shows the traction-separation law for a one-dimension cohesive interface.

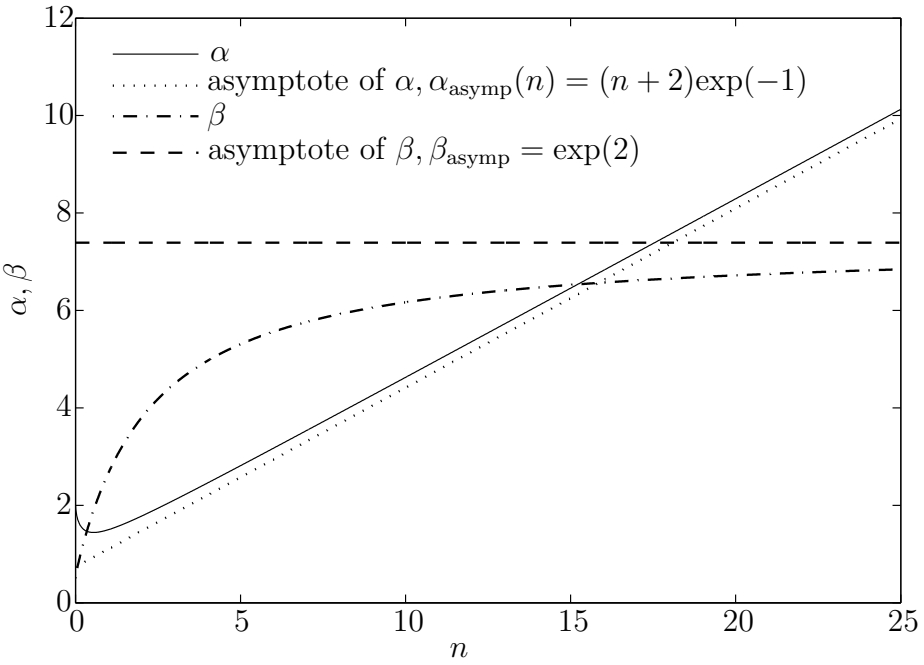

Figure 2.5: Variation of α and β versus n (see Eqs. (2.27) and (2.28)). Different choice of n can affect the original stiffness of cohesive cracks ($k_n \propto \beta$) and the required jump for a fully damaged crack ($[\![\mathbf{u}^f]\!]_{\text{full}} \propto \alpha$).

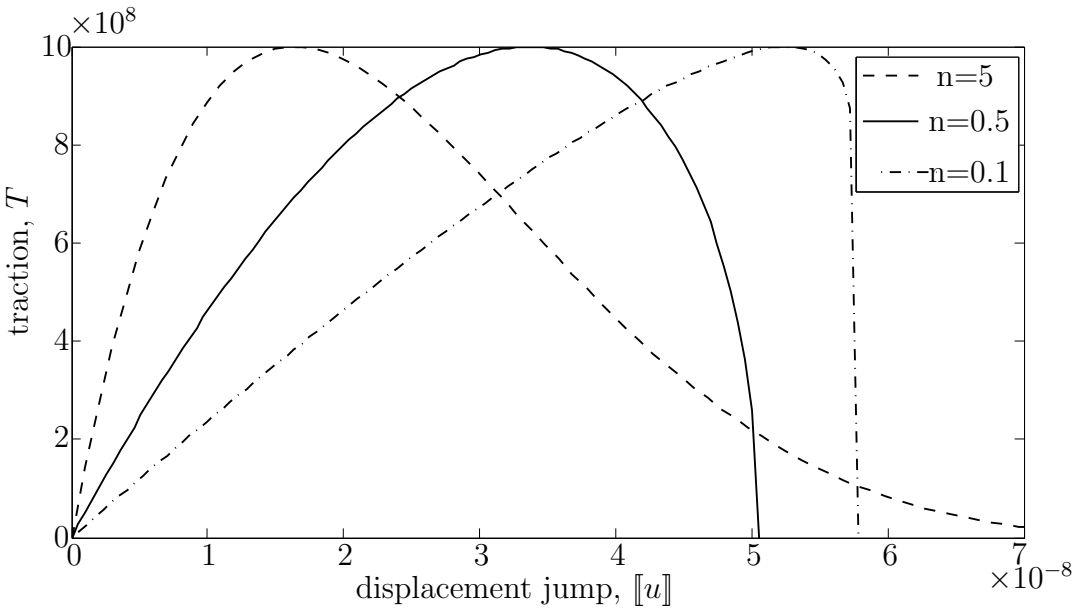

Figure 2.6: Traction-displacement curve for different value of parameter n in one dimension cohesive interface. In this figure, $\kappa_{ini} = 0$, the critical fracture energy equals $G_{Ic} = 35\frac{J}{m^2}$ and the maximum tensile strength is $\sigma_{\max} = 1\text{GPa}$ [Shabir et al., 2011].

The tangent stiffness of a cohesive element is required for Newton-Raphson iterative solver

$$\begin{aligned}\tilde{\mathbf{K}}_{dT} &= \frac{\mathrm{d}\tilde{\mathbf{T}}}{\mathrm{d}[\![\tilde{\mathbf{u}}^f]\!]} = \frac{\partial\tilde{\mathbf{T}}}{\partial[\![\tilde{\mathbf{u}}^f]\!]} + \frac{\partial\tilde{\mathbf{T}}}{\partial d}\frac{\partial d}{\partial[\![\tilde{\mathbf{u}}^f]\!]} \\ &= \tilde{\mathbf{K}}_d - \frac{1}{\kappa}\frac{\partial d}{\partial\kappa}\begin{bmatrix} k_n^+\mathcal{H}([\![\tilde{u}_n^f]\!]) & 0 \\ 0 & k_t \end{bmatrix}\begin{bmatrix} [\![\tilde{u}_n^f]\!] \\ [\![\tilde{u}_t^f]\!] \end{bmatrix}\left[[\![\tilde{u}_n^f]\!]\mathcal{H}([\![\tilde{u}_n^f]\!]) \ , \ [\![\tilde{u}_t^f]\!]\right], \quad \forall\kappa > 0\end{aligned} \tag{2.30}$$

In the case $\kappa = 0$ then $\tilde{\mathbf{K}}_{dT} = \tilde{\mathbf{K}}_d$.

The constitutive equation of cohesive interface in the global coordinate system is obtained by using the transformation matrix, $\mathbf{T}_\Gamma$:

$$\mathbf{T} = \mathbf{T}_\Gamma^{-1}\tilde{\mathbf{K}}_d\mathbf{T}_\Gamma[\![\mathbf{u}^f]\!] \quad \text{where} \quad \mathbf{T}_\Gamma = \begin{bmatrix} \cos\theta_\Gamma & -\sin\theta_\Gamma \\ \sin\theta_\Gamma & \cos\theta_\Gamma \end{bmatrix}. \tag{2.31}$$

θ_Γ is the angle between the global coordinate system and the local coordinate system on the boundary of the grains which is shown in Fig. 2.3.

2.4 Finite Element Discretization

In order to use Eq. (2.1) in the finite element method, first it is changed this equation to the Voigt notation. Recalling that the tensor and voight notations are the same:

$$\delta\Pi^f = \int_{\Omega^f\setminus\Gamma^f} \delta\boldsymbol{\varepsilon}^{f^T}\boldsymbol{\sigma}^f \ \mathrm{d}\Omega + \int_{\Gamma^f} [\![\delta\mathbf{u}^f]\!]^T\mathbf{T}^f \ \mathrm{d}\Gamma - \int_{\partial\Omega_N} \delta\mathbf{u}^{f^T}\mathbf{F} \ \mathrm{d}\Gamma = 0. \tag{2.32}$$

where $\delta\boldsymbol{\varepsilon}^f$ and $\boldsymbol{\sigma}^f$ are the vector form of virtual strain and stress tensor respectively:

$$\delta\boldsymbol{\varepsilon}^{f^T} = \left[\frac{\partial\delta u^f}{\partial x} \quad \frac{\partial\delta v^f}{\partial y} \quad \left(\frac{\partial\delta u^f}{\partial y} + \frac{\partial\delta v^f}{\partial x}\right)\right], \tag{2.33}$$

$$\boldsymbol{\sigma}^f = \begin{bmatrix}\sigma_{xx}^f & \sigma_{yy}^f & \sigma_{xy}^f\end{bmatrix}^T. \tag{2.34}$$

The FE formulation is developed by discretising Eq. (2.32) spatially. The orthotropic grains discretised by linear triangular finite elements.The interface

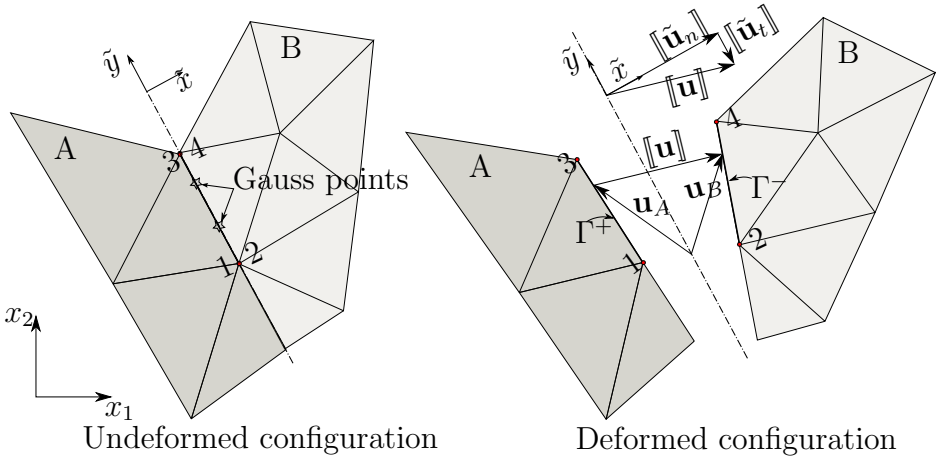

Figure 2.7: Local coordinate system on the boundary of a grain, $(\tilde{x}, \tilde{y})$, and displacement jump, $[\![\mathbf{u}]\!]$ in the local coordinate system. It is noted that the translation and rotation of local coordinates due to deformation can be neglected since small deformation is assumed. The node arrangement in the cohesive element must be based on the following construction: a) Node 1 and Node 3 belong to one grain, and Node 2 and Node 4 belong to the other grain, b) Node 1 has same position of Node 2, and Node 3 has the same position of Node 4, c) Nodes 1 and 3 must be chosen so that their grain fallen in the left side of the path from Node 1 to Node 3, d) The unit vectors of the local coordinate system are given by $\hat{\mathbf{t}} = \dfrac{\mathbf{x}_3 - \mathbf{x}_1}{\|\mathbf{x}_3 - \mathbf{x}_1\|}$ and $\hat{\mathbf{n}} = [\hat{t}_x \ , \ -\hat{t}_y]^T$, e) Therefore the displacement jump is defined by: $[\![\mathbf{u}^f(\tilde{y})]\!] = \mathbf{u}^f_B(\tilde{y}) - \mathbf{u}^f_A(\tilde{y})$.

of grains is discretized by 4-node cohesive elements with two integration points (see Fig. 2.7). The approximation of the displacement field $\mathbf{u}^f$ and strain $\boldsymbol{\varepsilon}^f$ in element (e) are given by:

$$\forall \mathbf{x} \in \Omega_e^f, \quad \mathbf{u}^f(\mathbf{x}) = \mathbf{N}_e \mathbf{U}_e^f, \tag{2.35}$$

$$\forall \mathbf{x} \in \Omega_e^f, \quad \boldsymbol{\varepsilon}^f(\mathbf{x}) = \mathbf{B}_e \mathbf{U}_e^f, \tag{2.36}$$

$$\tag{2.37}$$

where $\mathbf{N}_e$ is the linear shape function matrix, $\mathbf{B}_e$ is the matrix of the shape functions derivatives, and $\mathbf{U}^f$ is the nodal displacement vector:

$$\mathbf{N}_e(\mathbf{x}) = \begin{bmatrix} N_1(\mathbf{x}) & 0 & N_2(\mathbf{x}) & 0 & N_3(\mathbf{x}) & 0 \\ 0 & N_1(\mathbf{x}) & 0 & N_2(\mathbf{x}) & 0 & N_3(\mathbf{x}) \end{bmatrix}_e, \tag{2.38}$$

$$\mathbf{B}_e(\mathbf{x}) = \begin{bmatrix} \frac{\partial N_1}{\partial x} & 0 & \frac{\partial N_2}{\partial x} & 0 & \frac{\partial N_3}{\partial x} & 0 \\ 0 & \frac{\partial N_1}{\partial y} & 0 & \frac{\partial N_2}{\partial y} & 0 & \frac{\partial N_3}{\partial y} \\ \frac{\partial N_1}{\partial y} & \frac{\partial N_1}{\partial x} & \frac{\partial N_2}{\partial y} & \frac{\partial N_2}{\partial x} & \frac{\partial N_3}{\partial y} & \frac{\partial N_3}{\partial x} \end{bmatrix}_e \tag{2.39}$$

$$\mathbf{U}_e^{fT} = \begin{bmatrix} U_1^f & V_1^f & U_2^f & V_2^f & U_3^f & V_3^f \end{bmatrix}_e. \tag{2.40}$$

where U_i^f and V_i^f are the the displacement of node i in x- and y-directions respectively. The displacement jump $[\![\mathbf{u}^f]\!]$ in the cohesive elements (d) can be obtained by defining a matrix that contains the linear shape functions:

$$\forall \mathbf{x} \in \Gamma_d^f \quad [\![\mathbf{u}^f]\!](\mathbf{x}) = \mathbf{B}_d(\mathbf{x})^\Gamma \mathbf{U}_d^f, \tag{2.41}$$

$$\mathbf{B}_d^\Gamma(\mathbf{x}) = \begin{bmatrix} -N_1 & 0 & N_2 & 0 & -N_3 & 0 & N_4 & 0 \\ 0 & -N_1 & 0 & N_2 & 0 & -N_3 & 0 & N_4 \end{bmatrix}_d, \tag{2.42}$$

$$\mathbf{U}_d^f = \begin{bmatrix} U_1 & V_1 & U_2 & V_2 & U_3 & V_3 & U_4 & V_4 \end{bmatrix}_d^T. \tag{2.43}$$

where Γ_d^f is the interface between the grains, and the shape functions of cohesive elements are the trace of the shape functions on the adjacent triangular elements. It is noted that the jump extractor matrix $\mathbf{B}_d^f$ is designed based on the particular node arrangement that have been explained in Fig. 2.7.

Finally, finite element discretization of Eq. (2.32) writes:

$$\delta\Pi^f(\mathbf{U}^f,\delta\mathbf{U}^f) = \delta\mathbf{U}^{fT}\left(\sum_{e=1}^{n_B}\mathbf{M}_e\int_{\Omega_e^f\setminus\Gamma^f}\mathbf{B}_e^{fT}\boldsymbol{\sigma}_e^f\ \mathrm{d}\Omega+\sum_{d=1}^{n_C}\bar{\mathbf{M}}_d\int_{\Gamma_d^f}\mathbf{B}_d^{\Gamma T}\mathbf{T}_d^f\ \mathrm{d}\Gamma - \sum_{e=1}^{n_B}\mathbf{M}_e\int_{\partial\Omega_N}\mathbf{N}_e{}^T\mathbf{F}\ \mathrm{d}\Gamma\right)=0. \tag{2.44}$$

where $\mathbf{M}_e$ and $\bar{\mathbf{M}}_d$ are the boolean matrices that maps respectively the bulk element and the cohesive element vectors to the corresponding entries of global vectors. The total number of triangular elements and cohesive elements are n_B and n_C respectively. Since the variational work is zero for any admissible variation of displacement vector $\delta\mathbf{U}^f$, it is concluded that the residual force vector must be null:

$$\mathbf{R}^f\left(\mathbf{U}^f\right)=\mathbf{f}_{\text{int}}\left(\mathbf{U}^f\right)-\mathbf{f}_{\text{ext}}=\mathbf{0}, \tag{2.45}$$

$$\mathbf{f}_{\text{int}}\left(\mathbf{U}^f\right)=\sum_{e=1}^{n_B}\mathbf{M}_e\int_{\Omega_e^f\setminus\Gamma^f}\mathbf{B}_e^{fT}\boldsymbol{\sigma}_e^f\ \mathrm{d}\Omega+\sum_{d=1}^{n_C}\bar{\mathbf{M}}_d\int_{\Gamma_d^f}\mathbf{B}_d^{\Gamma T}\mathbf{T}_d^f\ \mathrm{d}\Gamma \tag{2.46}$$

$$\mathbf{f}_{\text{ext}}=\sum_{e=1}^{n_B}\mathbf{M}_e\int_{\partial\Omega_N}\mathbf{N}_e{}^T\mathbf{F}\ \mathrm{d}\Gamma. \tag{2.47}$$

Because of the nonlinear behaviour of the cohesive interface elements, Eq. (2.45) cannot be solved directly for $\mathbf{U}^f$. The Newton-Raphson procedure is employed to find the solution iteratively. Therefore, Eq. (2.45) is linearised with respect to the displacement vector $\mathbf{U}^f$:

$$\bar{\mathbf{R}}^f\left(\mathbf{U}^f+\delta\mathbf{U}^f\right)\approx\mathbf{R}^f(\mathbf{U}^f)+\frac{\partial\mathbf{R}^f\left(\mathbf{U}^f\right)}{\partial\mathbf{U}^f}\delta\mathbf{U}^f= \mathbf{f}_{\text{int}}\left(\mathbf{U}^f\right)-\mathbf{f}_{\text{ext}}+\frac{\partial\mathbf{f}_{\text{int}}^f\left(\mathbf{U}^f\right)}{\partial\mathbf{U}^f}\delta\mathbf{U}^f. \tag{2.48}$$

In the linearised equilibrium equation (2.48) the term $\dfrac{\partial\mathbf{f}_{\text{int}}^f\left(\mathbf{U}^f\right)}{\partial\mathbf{U}^f}$ is the tangent

stiffness matrix $\mathbf{K}_T^f$ that is given by:

$$\frac{\partial \mathbf{f}_{\text{int}}^f\left(\mathbf{U}^f\right)}{\partial \mathbf{U}^f} = \sum_{e=1}^{n_B} \mathbf{M}_e \left(\int_{\Omega_e^f \setminus \Gamma^f} \mathbf{B}_e^{f\,T} \frac{\partial \boldsymbol{\sigma}_e^f}{\partial \mathbf{U}_e^f} \, \mathrm{d}\Omega \right) \mathbf{M}_e^T + \sum_{d=1}^{n_C} \bar{\mathbf{M}}_d \left(\int_{\Gamma_d^f} \mathbf{B}_d^{\Gamma\,T} \frac{\partial \mathbf{T}_d^f}{\partial \mathbf{U}_d^f} \, \mathrm{d}\Gamma \right) \bar{\mathbf{M}}_d^T, \tag{2.49}$$

where

$$\frac{\partial \boldsymbol{\sigma}_e^f}{\partial \mathbf{U}_e^f} = \frac{\partial \boldsymbol{\sigma}_e^f}{\partial \boldsymbol{\varepsilon}_e^f} \frac{\partial \boldsymbol{\varepsilon}_e^f}{\partial \mathbf{U}_e^f} = \mathbf{C}_e^f \mathbf{B}_e^f, \tag{2.50}$$

$$\frac{\partial \mathbf{T}_d^f}{\partial \mathbf{U}_d^f} = \frac{\partial \mathbf{T}_d^f}{\partial [\![\mathbf{u}^f]\!]_d} \frac{\partial [\![\mathbf{u}^f]\!]_d}{\partial \mathbf{U}_d^f} = \mathbf{K}_{dT_d} \mathbf{B}_d^\Gamma. \tag{2.51}$$

where $\mathbf{C}^f$ is the stiffness matrix of the bulk element e given by Eq. 2.9, and $\mathbf{K}_{dT}$ is the stiffness matrix of the interface element d given by Eq. 2.31. Then, the tangent stiffness matrix can be written as following:

$$\mathbf{K}_T^f = \sum_{e=1}^{n_B} \mathbf{M}_e \left(\int_{\Omega_e^f \setminus \Gamma^f} {\mathbf{B}_e}^T \mathbf{C}_e^f \mathbf{B}_e \, \mathrm{d}\Omega \right) \mathbf{M}_e^T + \sum_{d=1}^{n_C} \bar{\mathbf{M}}_d \left(\int_{\Gamma_d^f} \mathbf{B}_d^{\Gamma\,T} \mathbf{K}_{dT_d} \mathbf{B}_d^\Gamma \, \mathrm{d}\Gamma \right) \bar{\mathbf{M}}_d^T, \tag{2.52}$$

Finally, by assuming $\bar{\mathbf{R}}^f\left(\mathbf{U}^f + \delta\mathbf{U}^f\right) = \mathbf{0}$, the variation of the displacement at each iteration of the Newton-Raphson solver is obtained by:

$$\delta\mathbf{U}^f = -\mathbf{K}_T^{f^{-1}} \mathbf{R}^f(\mathbf{U}^f). \tag{2.53}$$

2.5 Conclusion

In this chapter, a constitutive model for polycrystalline materials was introduced. A two-dimensional orthotropic constitutive model was considered for the bulk grains. The interfaces between the grains were modelled with a thermodynamically consistent cohesive law, and the underlying damage evolution law was detailed. The influence of microscopic material parameters on the fracture

toughness and the stiffness of cohesive interface was explained. Finally, the finite element formulations for the bulk grains and the cohesive interfaces were derived.

Since the modelling of engineering problems in grain level is not affordable, a multiscale method will be developed that make it possible to model the engineering problem in such way that the microscopic details are taken into consideration. In the next chapter, two classes of existence multiscale methods, which are the bases for the proposed multiscale technique in this thesis, will be introduced.

Chapter 3

Hierarchical and Concurrent Multiscale Methods

This chapter explains a hierarchical multiscale method, based on computational homogenisation, and a concurrent multiscale method, based on domain decomposition. Homogenisation techniques, known as hierarchical methods, aim at obtaining the average quantities of the constitutive relation for a macroscopic point by testing at a spatial sample of the heterogeneous microstructure which is called a Representative Volume Element (RVE). In computational homogenisation methods, the constitutive equations do not need to be explicitly defined at the macro-level. Incremental macroscopic stress-strain laws are obtained on-the-fly during the macroscopic solution process by solving the boundary value problem associated with the RVE at each (quadrature) point of the macroscopic problem. The boundary conditions of the RVE are defined by macroscopic state variables, e.g., strain or stress. The overall response of the RVE is used to determine the macroscopic constitutive equation [Suquet, 1987; Feyel and Chaboche, 2000; Kouznetsova et al., 2001].

Domain decomposition techniques are widely used to solve large scale problems in parallel by splitting the domain into several sub-domains. Sub-domains may or may not overlap, can have different physical properties, and can also be discretised by meshes which are not conforming [Lions, 1988; Farhat and Roux, 1991; Mandel, 1993; Ladevèze and Simmonds, 1999]. Domain decomposition is

well suited to the solution of multiscale problems, in which the domain is split naturally into fine scale regions and coarse scale regions. The fine scale in the area of interest with a fine discretisation is glued to the surrounding coarse mesh through overlapping or non-overlapping coupling methods, and the global solution is obtained by solving fine and coarse meshes concurrently. For our problem, domain decomposition method can be used to model fracture in polycrystalline materials by splitting the domain into the microscopic sub-domain and macroscopic sub-domain, which microscopic domain composed of grains with cohesive cracks while the macroscopic sub-domain is a homogeneous domain.

3.1 Hierarchical Multiscale: FE^2 Method

In this section, a hierarchical multiscale method based on computational homogenisation for a nonlinear heterogeneous material (the fracture of polycrystalline materials) is detailed. In this method the effective material properties are computed by using averaging theorems applied to kinematic and static quantities of the heterogeneous microscale material. This method is based on the scale separation assumption, which requires, 1) the gradient of the macroscopic fields are not extensive over the underlying microstructure, and 2) the fluctuation of the microscopic fields affect the macroscopic behaviour only through their volume average [Bohm, 2008]. Homogenisation provides a bridge between scales by mapping the average of the stress from the microscale to the macroscale and downscaling the macroscopic deformation tensor to the boundary of the microscopic RVE. The main advantages of computational homogenisation technique are:

- Computational homogenisation is a general method, even for very nonlinear problems as opposed to semi-analytical methods, e.g. mean-fields, that require some homogeneity of the micro fields in each micro phase.
- It does not require for explicit macroscopic constitutive law trough heuristic curve-fitting.
- In comparison with semi-analytical mean-field theories, computational ho-

mogenisation method potentially is more accurate since there is no approximation of the fields in its underlying RVE.

- It gives useful insight in micro-fields due to the previous point.

In homogenisation method, the macroscopic deformation tensor provides the boundary conditions for the microscopic RVE. The solution of the boundary value problem for the RVE yields the tangent stiffness moduli and the macroscopic stress tensor which can then be used for calculating the internal force vector at the macroscale. This hierarchical multiscale method that implicitly defines nonlinear homogenised constitutive relationships is often called the FE^2 method [Feyel and Chaboche, 2000] since the finite element method is used at both the macro and micro scales.

3.1.1 Macroscopic problem

When the characteristic length of the problem at the loading scale, L, is considerably larger than the characteristic length of the microstructure, l (see Fig. 2.2) computational homogenisation can be employed to search for an effective displacement field $\mathbf{u}^c \in \mathcal{U}^c$ defined over Ω which

$$\forall \delta\mathbf{u}^c \in \mathcal{U}^{c,0}, \quad \delta\Pi = \int_\Omega \boldsymbol{\sigma}^c_{|_t} : \boldsymbol{\varepsilon}(\delta\mathbf{u}^c)\, \mathrm{d}\Omega - \int_{\partial\Omega_N} \mathbf{F}_{|_t} \cdot \delta\mathbf{u}^c\, \mathrm{d}\Gamma = 0. \tag{3.1}$$

$\mathcal{U}^c$ and $\mathcal{U}^{c,0}$ are collections of trial functions, $\mathbf{u}$, and test functions, $\delta\mathbf{u}$, respectively, which can be defined by

$$\mathcal{U}^c = \left\{ \mathbf{u} | \mathbf{u} \in H^1(\Omega), \mathbf{u}_{|\partial\Omega_D} = \mathbf{u}_D \right\}, \tag{3.2}$$

$$\mathcal{U}^{c,0} = \left\{ \mathbf{u} | \mathbf{u} \in H^1(\Omega), \delta\mathbf{u}_{|\partial\Omega_N} = \mathbf{0} \right\}, \tag{3.3}$$

where H^1 is the Sobolev space of degree one. The Dirichlet boundary condition at all times is given by

$$\mathbf{u}^c_{|_{\mathbf{x},t}} = \mathbf{u}_{D|_{\mathbf{x},t}} \quad \text{on } \partial\Gamma_D. \tag{3.4}$$

The Homogenised constitutive law at the coarse scale relates the coarse stress to the history of the coarse strain, locally at every point of the domain:

$$\boldsymbol{\sigma}^c_{|\mathbf{x},t} = \sigma^c \left(\left(\boldsymbol{\varepsilon}(\mathbf{u}^c_{|\mathbf{x},\mathcal{T}}) \right)_{\mathcal{T} \leq t} \right) \quad \text{in } \Omega, \tag{3.5}$$

where $\boldsymbol{\sigma}^c$ and $\boldsymbol{\varepsilon}^c$ are the coarse scale stress and strain respectively. In the general framework of homogenisation, the coarse scale constitutive law (3.5) is not known *a priori*. It is assumed however that, at lower scales, the constitutive law of the microstructural heterogeneities is known, or is at least identifiable. The coarse scale problem Eq. (3.1) is spatially discretised by triangular linear finite elements. One integration point suffices for each element. Finally, the finite element discretisation of Eq. (3.1) can be written as:

$$\delta\Pi^c = \delta\mathbf{U}^{cT} \left(\sum_e \mathbf{M}_e \int_{\Omega^c_e \ \Gamma^c} \mathbf{B}^{cT}_e \boldsymbol{\sigma}^c_e \, \mathrm{d}\Omega - \sum_e \mathbf{M}_e \int_{\partial\Omega_N} \mathbf{N}_e{}^T \mathbf{F} \, \mathrm{d}\Gamma \right) = 0. \tag{3.6}$$

where $\mathbf{N}_e$ and $\mathbf{B}^c_e$ are shape function matrix and derivaties of the shape functions for the triangular linear coarse elements which are given by (2.38) and (2.39) respectively. $\boldsymbol{\sigma}^c_e$ is the vector form of stress, and $\mathbf{M}_e$ is the boolean matrix that maps the coarse element vector to the corresponding entries of the global vector. Since the variational work is zero for any admissible variation of displacement vector $\delta\mathbf{U}^c$, it is concluded that the residual force vector must be null:

$$\mathbf{R}^c\left(\mathbf{U}^c\right) = \mathbf{f}_{\text{int}}\left(\mathbf{U}^c\right) - \mathbf{f}_{\text{ext}} = \mathbf{0}, \tag{3.7}$$

where

$$\mathbf{f}_{\text{int}}\left(\mathbf{U}^c\right) = \sum_e \mathbf{M}_e \int_{\Omega^c_e} \mathbf{B}^{cT}_e \boldsymbol{\sigma}^c_e \, \mathrm{d}\Omega \tag{3.8}$$

$$\mathbf{f}_{\text{ext}} = \sum_e \mathbf{M}_e \int_{\partial\Omega_N} \mathbf{N}_e{}^T \mathbf{F} \, \mathrm{d}\Gamma. \tag{3.9}$$

Because of material non-linearity, Eq. (3.7) cannot be solved directly for $\mathbf{U}^c$. The Newton-Raphson procedure is employed to find the solution iteratively. The

linearisation of the coarse scale residual $\mathbf{R}^c$ with respect to the displacement $\mathbf{U}^c$ is given by:

$$\bar{\mathbf{R}}^c\left(\mathbf{U}^c+\delta\mathbf{U}^c\right)=\mathbf{R}^c\left(\mathbf{U}^c\right)+\frac{\partial\mathbf{R}^c}{\partial\mathbf{U}^c}\delta\mathbf{U}^c=0, \tag{3.10}$$

finally the linearised equilibrium equation for the coarse scale problem can be written as

$$\mathbf{K}_T^c\delta\mathbf{U}^c=-\left(\mathbf{f}_{\text{int}}\left(\mathbf{U}^c\right)-\mathbf{f}_{\text{ext}}\right) \tag{3.11}$$

where after each iteration, the displacement vector $\mathbf{U}^c$ is updated, and consequently the internal force vector $\mathbf{f}_{\text{int}}\left(\mathbf{U}^c\right)$ and the tangent stiffness matrix $\mathbf{K}_T^c$ is updated by solving the underlying RVE problem. The tangent stiffness matrix is

$$\begin{aligned}\mathbf{K}_T^c=\frac{\partial\mathbf{f}_{\text{int}}}{\partial\mathbf{U}^c}&=\sum_e\mathbf{M}_e\left(\int_{\Omega_e^c}\mathbf{B}_e^{cT}\frac{\partial\boldsymbol{\sigma}_e^c}{\partial\boldsymbol{\varepsilon}_e^c}\frac{\partial\boldsymbol{\varepsilon}_e^c}{\partial\mathbf{U}_e^c}\,\mathrm{d}\Omega\right)\mathbf{M}_e^T\\&=\sum_e\left(\mathbf{M}_e\int_{\Omega_e^c}\mathbf{B}_e^{cT}\mathbf{C}_{T_e}\mathbf{B}_e^c\,\mathrm{d}\Omega\right)\mathbf{M}_e^T\end{aligned} \tag{3.12}$$

where $\mathbf{C}_{T_e}$ is the macroscopic tangent stiffness that is computed through the homogenisation of RVE. When the component of residual force $\mathbf{R}^c(\mathbf{U}^c)$ become "very small" (less than some convergence tolerance) the Newton-Raphson iterations are stopped, and a new time step is started by changing the external force $\mathbf{f}_{\text{ext}}$. More details on the convergence criterion is given in Section 3.2.3.

3.1.2 Homogenised constitutive law

The coarse scale constitutive law (3.5) at an arbitrary point $\mathbf{x}$ is obtained through homogenisation. The material point $\mathbf{x}$ can be related to a representative volume element (RVE). The RVE, $\mathcal{V}_\diamondsuit(\mathbf{x})$, must statistically represents the heterogeneity of the microstructure in the vicinity of the corresponding macroscopic point $\mathbf{x}$. The relation between $\boldsymbol{\sigma}^c$ and $\boldsymbol{\varepsilon}^c$ is obtained by solving a boundary-value problem over the RVE. The volume average of properties over the RVE is used at the corresponding point $\mathbf{x}$ at the coarse scale, Fig. 3.1.

According to homogenisation, the macroscopic strain, stress, and strain energy

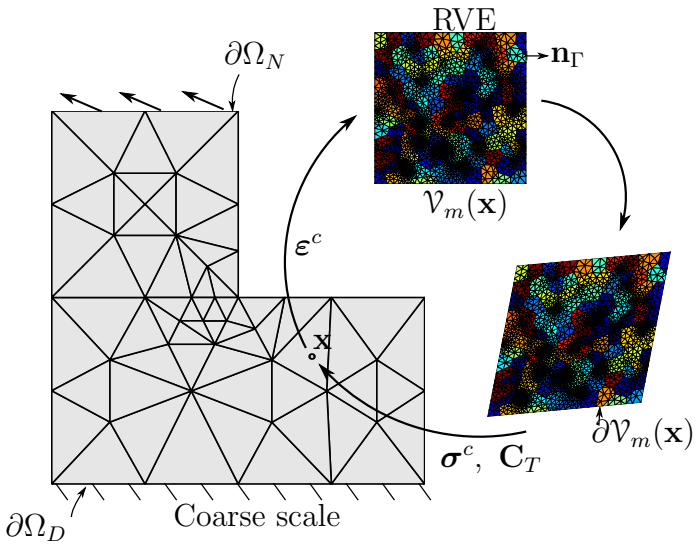

Figure 3.1: FE^2 scheme

at a local point, $\mathbf{x}$, are respectively related to the volume average of the strain and stress fields, and the strain energy of corresponding microscopic RVE, $\mathcal{V}_\diamond(\mathbf{x})$. In the following, the homogenisation of the constitutive law of polycrystalline materials defined in Chapter 2 will be explained.

- **Strain averaging**: the volume average of the microscopic strain $\boldsymbol{\varepsilon}^f$ over an RVE, $\mathcal{V}_\diamond(\mathbf{x})$, is defined as the macroscopic strain $\boldsymbol{\varepsilon}^c$ at the associated macroscopic point $\mathbf{x}$ [Nemat-Nasser and Hori, 1999] :

$$\boldsymbol{\varepsilon}^c(\mathbf{x},t) = \langle \boldsymbol{\varepsilon}^f \rangle \ = \ \frac{1}{2|\mathcal{V}_\diamond(\mathbf{x})|} \int_{\partial V} \mathbf{u}^f \otimes \mathbf{n} + (\mathbf{u}^f \otimes \mathbf{n})^T \ \mathrm{d}\Gamma, \tag{3.13}$$

  where $|\mathcal{V}_\diamond(\mathbf{x})|$ is the surface area of the two-dimensional RVE, $\mathbf{n}$ denotes the unit outward vector normal to the RVE boundary, ∂V, and the tensor product operator is denoted by $\otimes$.

  However, Eq. 3.13 is not valid for a microstructure with discontinuities in the displacement field [Zohdi and Wriggers, 2008]. The volume average strain for a domain with jump in displacement field is given by:

$$\begin{aligned}\langle \boldsymbol{\varepsilon}^f \rangle \; =& \frac{1}{2|\mathcal{V}_\diamond(\mathbf{x})|} \int_{\partial V} \mathbf{u}^f \otimes \mathbf{n} + (\mathbf{u}^f \otimes \mathbf{n})^T \; \mathrm{d}\Gamma \\ & - \frac{1}{2|\mathcal{V}_\diamond(\mathbf{x})|} \int_{\Gamma^f} [\![\mathbf{u}^f]\!] \otimes \mathbf{n}_\Gamma + ([\![\mathbf{u}^f]\!] \otimes \mathbf{n}_\Gamma)^T \; \mathrm{d}\Gamma \end{aligned} \tag{3.14}$$

where $\mathbf{n}_\Gamma$ is the unit vector normal to the discontinuities, Γ^f. The direction of $\mathbf{n}_\Gamma$ should be chosen in a way that $[\![\mathbf{u}^f]\!] \cdot \mathbf{n}_\Gamma > 0$ in the opening mode.

If the RVE has the following uniform loading on its surface:

$$\forall \mathbf{x}^f \in \partial V, \quad \mathbf{u}^f(\mathbf{x}^f) = \boldsymbol{\varepsilon}^c \cdot \mathbf{x}^f,$$

then,

$$\begin{aligned}\boldsymbol{\varepsilon}^c \; &= \langle \boldsymbol{\varepsilon}^f \rangle \; + \frac{1}{2|\mathcal{V}_\diamond(\mathbf{x})|} \int_{\Gamma^f} [\![\mathbf{u}^f]\!] \otimes \mathbf{n}_\Gamma + ([\![\mathbf{u}^f]\!] \otimes \mathbf{n}_\Gamma)^T \; \mathrm{d}\Gamma \\ &= \frac{1}{2|\mathcal{V}_\diamond(\mathbf{x})|} \int_{\partial V} \mathbf{u}^f \otimes \mathbf{n} + (\mathbf{u}^f \otimes \mathbf{n})^T \; \mathrm{d}\Gamma. \end{aligned} \tag{3.15}$$

- **Stress averaging**: the coarse scale stress $\boldsymbol{\sigma}^c$ can be defined as the volume average of the microscopic stress $\boldsymbol{\sigma}^f$ over the RVE, $\mathcal{V}_\diamond(\mathbf{x})$

$$\boldsymbol{\sigma}^c(\mathbf{x}, t) \; = \; \langle \boldsymbol{\sigma}^f \rangle \; = \; \frac{1}{|\mathcal{V}_\diamond(\mathbf{x})|} \int_{\partial V} \mathbf{t}^f \otimes \mathbf{x}^f \; \mathrm{d}\Gamma, \tag{3.16}$$

  In Eq. (3.16), the average stress is defined in terms of the boundary tractions $\mathbf{t}^f$, and the local coordinates at the RVE scale, $\mathbf{x}^f$ [Nemat-Nasser and Hori, 1999]. Note that unlike Eq. 3.13, discontinuity in the displacement field does not change Eq. (3.16).

- **Strain energy averaging (Hill-Mandel condition)**: the Hill-Mandel condition which expresses the energy consistency of the micro-macro scale transition states that the volume average rate of work of any admissible microscale stress and strain rates over an RVE equals the rate of work of

the average stress over the RVE [Hill, 1963]:

$$\begin{aligned}\boldsymbol{\sigma}^c : \dot{\boldsymbol{\varepsilon}}^c &= \langle \boldsymbol{\sigma}^f : \dot{\boldsymbol{\varepsilon}}^f + \mathbf{T}^f \cdot [\![\dot{\mathbf{u}}^f]\!] \rangle \\ &= \frac{1}{|\mathcal{V}_\diamond(\mathbf{x})|} \left(\int_{\mathcal{V}\setminus\Gamma^f} \boldsymbol{\sigma}^f : \boldsymbol{\varepsilon}^f \mathrm{d}\Omega + \int_{\Gamma^f} \mathbf{T}^f \otimes [\![\dot{\mathbf{u}}^f]\!] \, \mathrm{d}\Gamma \right), \end{aligned} \tag{3.17}$$

where $\mathbf{T}^f \cdot [\![\dot{\mathbf{u}}^f]\!]$ is the rate of work of traction $\mathbf{T}^f$ on the cohesive interfaces. This equality ensures that the homogenized stiffness tensor defined through the average of stress work equals to the same defined through the relations of the average of stress-strain. This energy consistency is automatically ensured if the stress and strain averaging are correctly made.

In order to track down the coarse scale constitutive law (3.5), a boundary value problem is defined over the RVE by imposing the prescribed fully bounded displacement boundary condition that is compatible with the strain averaging theorem (3.13). We recall that the constitutive laws of the fine scale constituents are explicitly defined. Hence, locally in the coarse domain, we assume the existence of an equilibrated micro pair $(\mathbf{u}^f, \boldsymbol{\sigma}^f)$defined over $\mathcal{V}_\diamond(\mathbf{x})$ such that the governing equations introduced in Eqs. (2.1), (2.2) and (2.3) are satisfied. The weak form of the governing equations is given by:

$$\forall \delta\mathbf{u}^f \in \mathcal{U}^{f,0}, \quad \int_{\mathcal{V}\setminus\Gamma^f} \boldsymbol{\sigma}^f : \boldsymbol{\varepsilon}(\delta\mathbf{u}^f) \, \mathrm{d}\Omega + \int_{\Gamma^f} \mathbf{T}^f \cdot [\![\delta\mathbf{u}^f]\!] \, \mathrm{d}\Gamma = 0, \tag{3.18}$$

where $\mathcal{V}$ is the RVE domain, and Γ^f is all the cohesive interfaces in the RVE.

$$\mathcal{U}^f = \left\{ \mathbf{u} | \mathbf{u} \in H^1(\mathcal{V} \setminus \Gamma^f), \mathbf{u}_{|\partial\Omega_D} = \mathbf{u}_D^f \right\}, \tag{3.19}$$

$$\mathcal{U}^{f,0} = \left\{ \delta\mathbf{u} | \delta\mathbf{u} \in H^1(\mathcal{V} \setminus \Gamma^f), \delta\mathbf{u}_{|\partial\Omega_D} = \mathbf{0} \right\}, \tag{3.20}$$

$$\tag{3.21}$$

This means that the RVE is in static equilibrium without prescribed tractions on the boundary and without volume body force. $\mathcal{U}^f$ and $\mathcal{U}^{f,0}$ are the collections of trial solutions, $\mathbf{u}^f$, and test functions, $\delta\mathbf{u}^f$, respectively. The constitutive equations for the microstructure have been discussed in Section 2.3.

Downscaling kinematic condition: the following Dirichlet boundary condition which satisfies the strain averaging theorem (3.13) is imposed on the RVE problem:

$$\mathbf{u}_D^f(\mathbf{x}^f, t) = \boldsymbol{\varepsilon}^c(\mathbf{x}, t)\ \mathbf{x}^f \quad \text{on } \partial\Omega \tag{3.22}$$

where the macroscopic strain tensor $\boldsymbol{\varepsilon}^c(\mathbf{x}, t)$ is constant over $\mathcal{V}_\diamondsuit(\mathbf{x})$. This particular choice for the boundary conditions of the RVE problem enforces that the fluctuation of the displacement field is null over the boundary. The choice of the fluctuation of the displacement field has an influence on the accuracy of homogenisation which is beyond the scope of this work [Gitman et al., 2007].

Solving the RVE boundary value problem: The finite element method is used to solve the RVE problem defined by Eq. (3.18), and the Lagrange multiplier technique is adopted to impose the displacement boundary conditions (3.22):

$$\mathbf{R}_f^\diamondsuit(\mathbf{U}^f, \boldsymbol{\lambda}) = \mathbf{f}_{\text{int}}^\diamondsuit - \mathbf{f}_{\text{ext}}^\diamondsuit - \mathbf{A}_{bf}^T\boldsymbol{\lambda} = \mathbf{0}, \tag{3.23}$$

$$\mathbf{R}_u^\diamondsuit(\mathbf{U}^f) = \mathbf{A}_{bf}\mathbf{U}^f - \mathbf{u}_D^f = \mathbf{0}, \tag{3.24}$$

where $\mathbf{R}_f^\diamondsuit$ and $\mathbf{R}_u^\diamondsuit$ are the residual forces and residual displacements of the RVE, respectively. $\mathbf{U}^f$ is the nodal displacement at the fine scale, $\boldsymbol{\lambda}$ are the Lagrange multipliers, and $\mathbf{A}_{bf}$ is a boolean matrix that extracts the DOFs of the boundary from the total DOFs of the RVE. For our RVE boundary value problem, the equations for calculation of the external force $\mathbf{f}_{\text{ext}}^\diamondsuit = \mathbf{0}$ and the internal force vector $\mathbf{f}_{\text{int}}^\diamondsuit$ is given by Eq. (2.46).

The constitutive relationships for the microstructure are given by Eqs.(2.5) and (2.7). The non-linear system of equations (3.23) and (3.24) are linearised and set to zero in order to employ the Newton-Raphson iterative solver:

$$\begin{aligned}\bar{\mathbf{R}}_f^\diamondsuit(\mathbf{U}^f + \delta\mathbf{U}^f, \boldsymbol{\lambda} + \delta\boldsymbol{\lambda}) =& \mathbf{R}_f^\diamondsuit(\mathbf{U}^f, \boldsymbol{\lambda}) + \\ & \frac{\partial \mathbf{R}_f^\diamondsuit(\mathbf{U}^f, \boldsymbol{\lambda})}{\partial \mathbf{U}^f}\delta\mathbf{U}^f + \frac{\partial \mathbf{R}_f^\diamondsuit(\mathbf{U}^f, \boldsymbol{\lambda})}{\partial \boldsymbol{\lambda}}\delta\boldsymbol{\lambda} = \mathbf{0}\end{aligned} \tag{3.25}$$

$$\bar{\mathbf{R}}_u^\diamondsuit(\mathbf{U}^f + \delta\mathbf{U}^f) = \mathbf{R}_u^\diamondsuit(\mathbf{U}^f) + \frac{\partial \mathbf{R}_u^\diamondsuit(\mathbf{U}^f)}{\partial \mathbf{U}^f}\delta\mathbf{U}^f = \mathbf{0}. \tag{3.26}$$

The resultant system of equations can be written in matrix form:

$$\begin{pmatrix} \overset{\diamondsuit}{\mathbf{K}}_T & p\mathbf{A}_{bf}^T \\ p\mathbf{A}_{bf} & \mathbf{0} \end{pmatrix} \begin{pmatrix} \delta\mathbf{U}^f \\ \delta\bar{\boldsymbol{\lambda}} \end{pmatrix} = - \begin{pmatrix} \mathbf{R}_f^{\diamondsuit}(\mathbf{U}^f, \boldsymbol{\lambda}) \\ \mathbf{R}_u^{\diamondsuit}(\mathbf{U}^f) \end{pmatrix}, \tag{3.27}$$

where the entries of right hand side vector are given by Eqs. (3.23) and (3.24), and the tangent stiffness of the RVE, $\overset{\diamondsuit}{\mathbf{K}}_T$, is given by Eq. (2.52). The Lagrange multipliers $\boldsymbol{\lambda}$ are replaced by $p\bar{\boldsymbol{\lambda}}$ to improve the condition number of the global stiffness matrix, as $p = \max(|\overset{\diamondsuit}{\mathbf{K}}_{ii}|)$ is a scalar related to the maximum diagonal entry of the initial stiffness matrix of RVE. It is calculated once at the beginning of simulation [Unger and Eckardt, 2011].

Up-scaling kinetic condition: After solving the RVE problem, the Lagrange multipliers $\boldsymbol{\lambda}$ represent the traction on the boundary of the RVE and can be used in Eq. (3.16) to upscale the macroscopic stress:

$$\begin{aligned} \boldsymbol{\sigma}^c(\mathbf{x},t) &= \frac{1}{|\mathcal{V}_\diamondsuit(\mathbf{x})|}\int_{\partial V} \mathbf{t}^f \otimes \mathbf{x}^f \, \mathrm{d}\Gamma \\ &= \frac{1}{|\mathcal{V}_\diamondsuit(\mathbf{x})|}\sum_{e=1}^{n_b}\left(\int_{\partial V_e\cap\partial V} \mathbf{t}_e^f \begin{bmatrix} N_1 & N_2 \end{bmatrix}_e \mathrm{d}\Gamma \begin{bmatrix} x_1^f & y_1^f \\ x_2^f & y_2^f \end{bmatrix}_e\right) \\ &= \frac{1}{|\mathcal{V}_\diamondsuit(\mathbf{x})|}\sum_{e=1}^{n_b}\left(\int_{\partial V_e\cap\partial V} \begin{bmatrix} t_x^f N_1 & t_x^f N_2 \\ t_y^f N_1 & t_y^f N_2 \end{bmatrix}_e \mathrm{d}\Gamma \begin{bmatrix} x_1^f & y_1^f \\ x_2^f & y_2^f \end{bmatrix}_e\right) \\ &= \frac{1}{|\mathcal{V}_\diamondsuit(\mathbf{x})|}\sum_{e=1}^{n_b} \begin{bmatrix} \lambda_{x_1} & \lambda_{x_2} \\ \lambda_{y_1} & \lambda_{y_2} \end{bmatrix}_e \begin{bmatrix} x_1^f & y_1^f \\ x_2^f & y_2^f \end{bmatrix}_e, \end{aligned} \tag{3.28}$$

where n_b is the number of the elements that have an edge on the boundary of RVE. N_1 and N_2 are the shape functions of the first and second nodes on that edge of element e that is common with the boundary of RVE, $\partial V_e \cap \partial V \neq \emptyset$. The position of the quadrature points on the element edge are given by interpolation of nodal positions using the finite element shape functions:

$$\mathbf{x}_e^f = \begin{bmatrix} N_1 & N_2 \end{bmatrix}_e \begin{bmatrix} x_1^f & y_1^f \\ x_2^f & y_2^f \end{bmatrix}_e, \tag{3.29}$$

The matrix of the node positions $[x_i,\ y_i]_e$ ($i = \{1, 2\}$) is constant, and can be out of integral. In the last line of Eq. (3.28), $\int \mathbf{t}^f N_i \, \mathrm{d}\Gamma$ gives the boundary integral of external traction $\mathbf{t}^f$ over external boundary of element e that in the finite element method, equals the nodal force $[\lambda_{x_i}, \lambda_{y_i}]_e$. Therefore, the macroscopic stress in Voigt form can be computed by:

$$\boldsymbol{\sigma}^c(\mathbf{x}, t) = \frac{1}{|\mathcal{V}_\diamond(\mathbf{x})|}\mathbf{D}^T\boldsymbol{\lambda}, \tag{3.30}$$

where

$$\mathbf{D}^T = \begin{bmatrix} x_1^f & 0 & x_2^f & 0 & \cdots & x_{n_b}^f & 0 \\ 0 & y_1^f & 0 & y_2^f & \cdots & 0 & y_{n_b}^f \\ 0.5y_1^f & 0.5x_1^f & 0.5y_2^f & 0.5x_2^f & \cdots & 0.5y_{n_b}^f & 0.5x_{n_b}^f \end{bmatrix}. \tag{3.31}$$

The macroscopic tangent stiffness $\mathbf{C}_T$ is determined by finding the relationship between $\delta\boldsymbol{\sigma}^c = \langle\delta\boldsymbol{\sigma}^f\rangle$ and $\delta\boldsymbol{\varepsilon}^c = \langle\delta\boldsymbol{\varepsilon}^f\rangle$ through the finite element solution of the RVE problem. Recall Eqs. (3.22) and (3.30), the variation of macroscopic stress and strain can be given by:

$$\delta\mathbf{u}_D^f = \mathbf{D}\delta\boldsymbol{\varepsilon}^c, \tag{3.32}$$

$$\delta\boldsymbol{\sigma}^c = \frac{1}{|\mathcal{V}_\diamond(\mathbf{x})|}\mathbf{D}^T\delta\boldsymbol{\lambda}. \tag{3.33}$$

On the other hand, the relation between $\delta\mathbf{u}_D^f$ and $\delta\boldsymbol{\lambda}$ can be defined through the Schur complement of the tangent stiffness matrix with respect to the internal nodes of the RVE $\delta\boldsymbol{\lambda} = \overset{\diamond}{\mathbf{K}}_S\ \delta\mathbf{u}_D^f$. Thus the macroscopic stress-strain relationship can be defined by:

$$\delta\boldsymbol{\sigma}^c = \frac{1}{|\mathcal{V}_\diamond(\mathbf{x})|}\mathbf{D}^T\ \overset{\diamond}{\mathbf{K}}_S\ \mathbf{D}\ \delta\boldsymbol{\varepsilon}^c, \tag{3.34}$$

where $\overset{\diamond}{\mathbf{K}}_S = \overset{\diamond}{\mathbf{K}}_{bb} - \overset{\diamond}{\mathbf{K}}_{bi}\overset{\diamond}{\mathbf{K}}_{ii}^{-1}\overset{\diamond}{\mathbf{K}}_{ib}$. Consequently, the macroscopic tangent stiffness $\mathbf{C}_T$ is

$$\mathbf{C}_T = \frac{1}{|\mathcal{V}_\diamond(\mathbf{x})|}\mathbf{D}^T\ \overset{\diamond}{\mathbf{K}}_S\ \mathbf{D}. \tag{3.35}$$

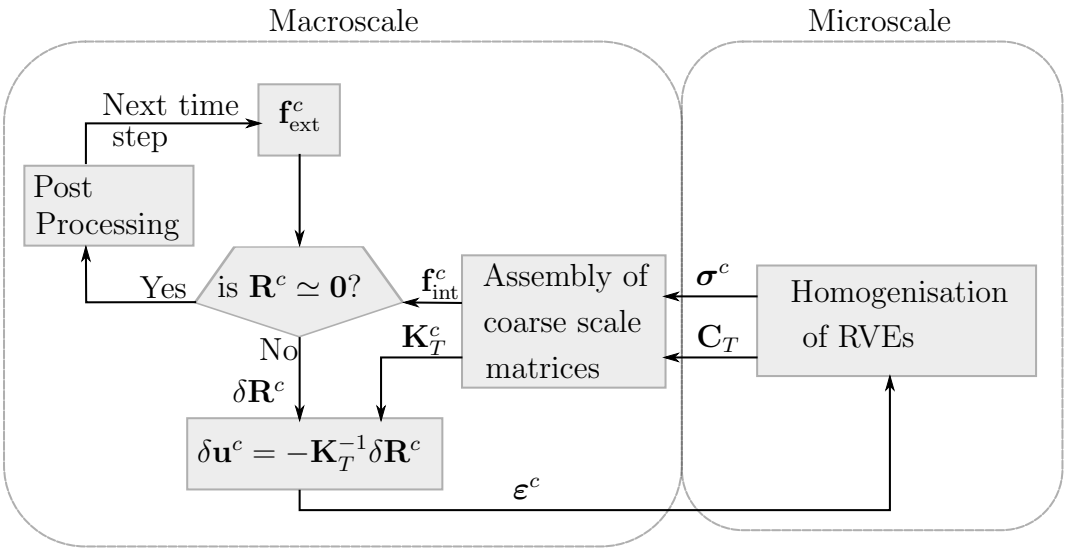

Figure 3.2: Flowchart for the FE^2 scheme.

An algorithm for the FE^2 method applied to out problem of fracture in polycrystalline materials is shown in Figure 3.2.

3.1.3 Limitations

In the previous section, a computational homogenisation multiscale method was presented. Despite a number of attractive characteristics, there are a few significant limitations to the this computational homogenisation framework which are described, for instance [Kouznetsova et al., 2002; Gitman et al., 2007; Geers et al., 2010]. The main limitations of homogenisation are:

- Bridging scales by homogenisation are only valid if scales are separable. The main shortcomings of classical homogenisation schemes come from the fundamental implicit assumption that the RVE size must be negligible in comparison with the macro structural characteristic length (determined by the size of the macroscopic specimen or the wave length of the macroscopic load) [Hill, 1963]. While softening happens, the homogenisation method is strongly sensitive to the variation of both macroscopic mesh size and RVE size.

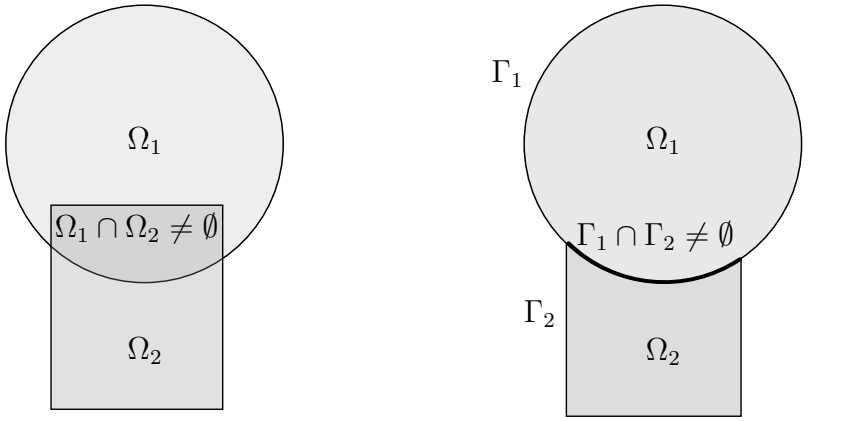

Figure 3.3: Overlapping and non-overlapping domain decomposition methods.

- This is a computationally expensive method but it is much cheaper than solving engineering problems fully at the microscale. However, novel methods aim at reducing this computational effort. For instance nonuniform transformation field analysis, [Michel and Suquet, 2003]; Model order reduction [Kerfriden et al., 2013]) and more heuristic ones where RVE is deactivated or RVEs are regrouped.

According to the first shortcoming, bridging scales by homogenisation are only valid if scales are separable. In the critical regions where the scale separation assumption is not fulfilled, the FE^2 method is bypassed and a concurrent multiscale method is adopted. In the concurrent multiscale method the scale separation assumption does not need to be fulfilled, since the microscopic model is solved directly.

In the next section, a concurrent multiscale method based on domain decomposition is detailed, in order to solve the microscopic problem in critical regions simultaneously with the macroscopic problem.

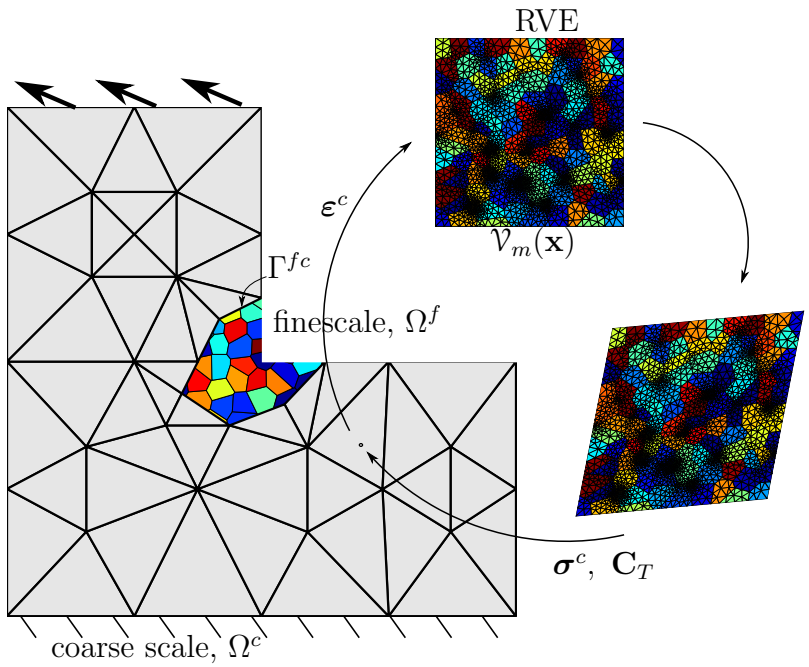

Figure 3.4: A hybrid multiscale method includes non-overlapping domain decomposition method and FE^2. See also Fig.3.6

3.2 Concurrent Multiscale: Domain Decomposition Method

Domain decomposition methods (DDM) can be used for solving a large problem by partitioning it into smaller subdomains or for solving a problem with different physical models in its sub-domains [Lions, 1988; Farhat and Roux, 1991; Mandel, 1993; Ladevèze and Simmonds, 1999].

Figure 3.3 shows the two main classes of Domain decomposition methods: overlapping [Dhia, 1998; Guidault and Belytschko, 2007] and non-overlapping [Lee et al., 2005; Lloberas-Valls et al., 2012] interface methods. DDM can also be categorised into direct and iterative.

For our problem, a non-overlapping DDM is adopted to solve directly the microscopic problem at a critical region concurrently along with the coarse scale problem at the region that scales are separable (see Fig. 3.4).

The domain Ω is partitioned into a coarse scale sub-domain Ω^c and a fine

scale sub-domain Ω^f such that $\Omega^c \cup \Omega^f = \Omega$ and $\Omega^c \cap \Omega^f = \emptyset$. The FE^2 method is used to solve the microscopic problem on average over Ω^c. The finite element method is deployed to directly model the microscopic problem at the fine scale Ω^f. Figure 3.4 depicts schematically the hybrid multiscale scheme for modelling of fracture in polycrystalline materials. It is assumed that there is an equation that bridges the fine scale to the coarse scale solutions:

$$\mathbf{R}^{\Gamma}\left(\mathbf{u}^c, \mathbf{u}^f\right) = \mathbf{0}, \quad \text{on } \Gamma^{fc}. \tag{3.36}$$

where $\mathbf{u}^f$ and $\mathbf{u}^c$ are the displacement field at the Ω^f and Ω^c, respectively.

The Lagrange multiplier technique is used to satisfy the constraint equation 3.36. At a stationary point, the variation of the Lagrangian function Λ with respect to the displacement of the coarse scale $\delta\mathbf{u}^c$, the displacement of the fine scale $\delta\mathbf{u}^f$, and the Lagrange multipliers $\delta\boldsymbol{\lambda}$ vanish and provide the equilibrium equation for the domain Ω:

$$\frac{\partial \Lambda}{\partial \mathbf{u}^c} \cdot \delta\mathbf{u}^c = \delta\Pi^c(\mathbf{u}^c, \delta\mathbf{u}^c) + \boldsymbol{\lambda} \cdot \frac{\partial \mathbf{R}^{\Gamma}(\mathbf{u}^c, \mathbf{u}^f)}{\partial \mathbf{u}^c}\delta\mathbf{u}^c = \mathbf{0}, \tag{3.37}$$

$$\frac{\partial \Lambda}{\partial \mathbf{u}^f} \cdot \delta\mathbf{u}^f = \delta\Pi^f(\mathbf{u}^f, \delta\mathbf{u}^f) + \boldsymbol{\lambda} \cdot \frac{\partial \mathbf{R}^{\Gamma}(\mathbf{u}^c, \mathbf{u}^f)}{\partial \mathbf{u}^f}\delta\mathbf{u}^f = \mathbf{0}, \tag{3.38}$$

$$\frac{\partial \Lambda}{\partial \boldsymbol{\lambda}} \cdot \delta\boldsymbol{\lambda} = \mathbf{R}^{\Gamma} \cdot \delta\boldsymbol{\lambda} = \mathbf{0}. \tag{3.39}$$

where the $\boldsymbol{\lambda}$ are Lagrange multipliers. It is noted that the arbitrary variation of displacement fields must be null on the Dirichlet boundary, $\delta\mathbf{u}(\mathbf{x}) = \mathbf{0} \quad \forall \mathbf{x} \in \partial\Omega_D$. The variation of the virtual works in the coarse scale $\delta\Pi^c$ and in the fine scale $\delta\Pi^f$ after discretization by finite elements are given by Eqs. (3.6) and (2.32) respectively. In the following, the choice of constraint equation (3.36) is discussed.

3.2.1 Coupling Fine-Coarse meshes

Coupling techniques can be divided into two main categories: strong and weak couplings. In strong coupling the fluctuation of microscopic displacement on the interface vanishes, while in weak coupling techniques fluctuations exist but its weighted average is zero on the coarse-fine interface. Figure 3.5 shows difference

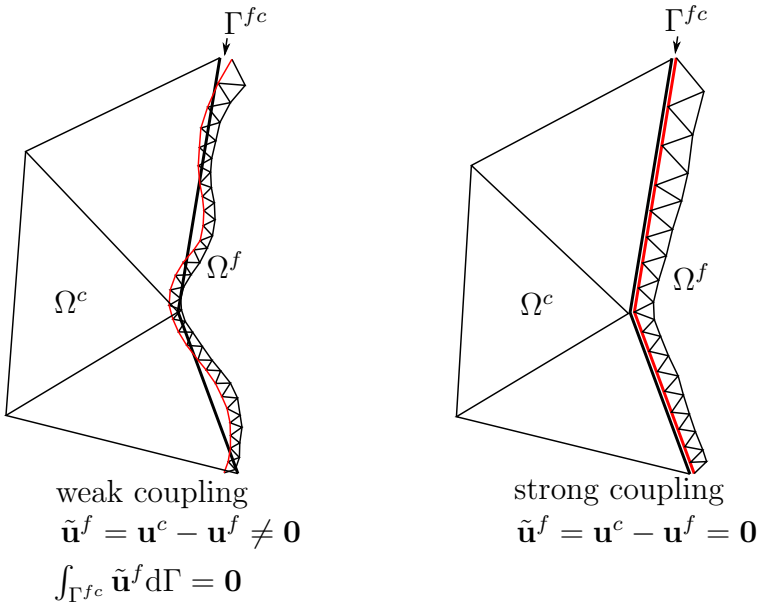

Figure 3.5: Strong coupling vs. weak coupling in non-overlapping DDM in deformed configuration.

between weak and strong coupling schematically.

For a microstructure with discrete cracks, employing a weak coupling technique increases the condition number of the global stiffness matrix, and consequently the Newton-Raphson solver requires more iteration to converge [Hund and Ramm, 2007; Ruess et al., 2011]. In other words, weak coupling techniques is more expensive in terms of computational cost. In this work, the linear multipoint constraint (LMPC) method [Abel JF, 1979; Farhat C, Lacour C, 1998] is adopted to impose a strong coupling on the displacement at the interface between the fine and the coarse meshes. This coupling technique is based on Lagrange multipliers that strongly glue the fine solution to the coarse solution along the common interface. The coarse scale is discretized by linear triangular elements, and as discussed in Chapter 2, the fine scale has been discretized by linear triangular elements, and four-node cohesive elements. The strong coupling between the fine scale nodal displacement and the coarse scale displacement at the interface Γ^{fc} is obtained by enforcing the micro nodes that belong to a macro edge to follow the edge deformation. For example, displacement of a fine mesh node i is enforced to follow the displacement of the edge of an adjacent coarse element e

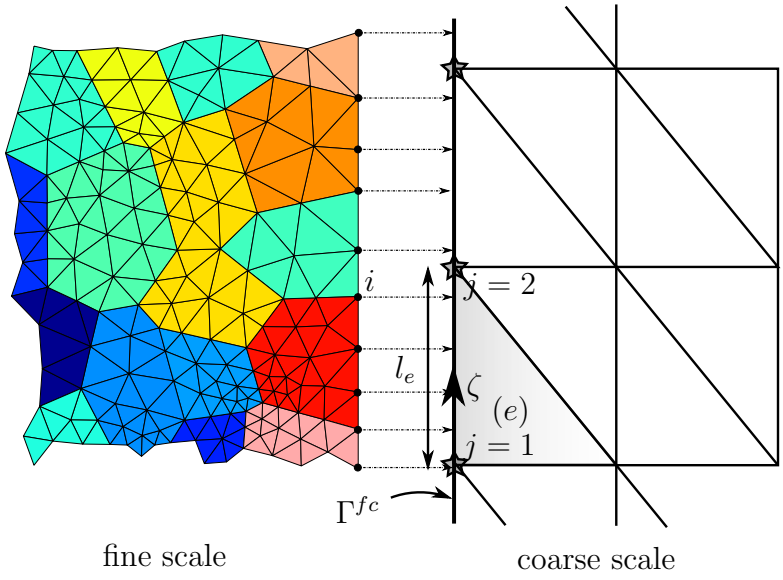

Figure 3.6: Strong coupling between the fine mesh and the coarse mesh using the linear multipoint constraint (LMPC) method.

by using the coarse element shape functions $\bar{\mathbf{N}}_e$ on the interface

$$\mathbf{R}_i^{\Gamma}\left(\mathbf{U}_e^c, \mathbf{U}_i^f\right) = \mathbf{U}_i^f - \bar{\mathbf{N}}_e(\zeta_i)\mathbf{U}_e^c = \mathbf{0}, \quad \text{on } \Gamma_e^{fc}. \tag{3.40}$$

where ζ is the local coordinate system of the coarse element e at the interface, and $\mathbf{u}_e^c$ is the nodal displacement vector of the element (e) on the interface Γ^{fc}. The shape function $\bar{\mathbf{N}}_e$ is given by

$$\bar{\mathbf{N}}_e(\zeta) = \begin{bmatrix} 1 - \frac{\zeta}{l_e} & 0 & \frac{\zeta}{l_e} & 0 \\ 0 & 1 - \frac{\zeta}{l_e} & 0 & \frac{\zeta}{l_e} \end{bmatrix} \tag{3.41}$$

where l_e is the length of edge of element (e) on the interface Γ^{fc}. Figure 3.6 displays details of the LMPC method.

Equation (3.40) provides the constraint equations for the particular node i. The global constraint equations for all the nodes on the interface Γ^{fc} is given by:

$$\mathbf{R}^{\Gamma}\left(\mathbf{U}^c, \mathbf{U}^f\right) = \mathbf{A}^f\mathbf{U}^f - \mathbf{A}^c\mathbf{U}^c = \mathbf{0}, \tag{3.42}$$

The boolean matrix $\mathbf{A}^f$ is defined to extract all nodal displacements of the fine mesh that corresponds to the interface Γ^{fc}, and $\mathbf{A}^c$ is a matrix combining the values of shape functions of the coarse nodes on the interface Γ^{fc}. Note that the coarse mesh is expected to vary due to adaptivity during the multiscale analysis. For this reason, the structure of the matrix $\mathbf{A}^c$ needs to be recomputed as soon as the coarse mesh is refined.

3.2.2 Solving the coupled problem

In this coupling technique microscopic cracks with one end on the interface Γ^{fc} cannot open due to the strong coupling of displacements imposed by coarse scale continuum displacement (see node i in Fig. 3.6), as macroscopic displacements are continuous along the coupling region. Even though we are not going to model plasticity in the grains, it is worth mentioning that the strong coupling of displacements can generate an artificial plasticity in those grains that are next to the coarse nodes on the interface Γ^{fc}. This is due to the jump of the macroscopic strain along the edge of the coarse elements and also at the coarse nodes.

By substituting the discretized form of Eqs. (3.6), (2.32) and (3.42) into the stationarity equations of Lagrangian functions (3.37), (3.38) and (3.39) a set of nonlinear equations for the domain Ω is obtained:

$$\begin{cases} \mathbf{R}^c\left(\mathbf{U}^c, \boldsymbol{\lambda}\right) = \mathbf{f}^c_{\text{int}}\left(\mathbf{U}^c\right) - \mathbf{f}^c_{\text{ext}} - \mathbf{A}^{cT}\boldsymbol{\lambda} = \mathbf{0}, \\ \mathbf{R}^f\left(\mathbf{U}^c, \boldsymbol{\lambda}\right) = \mathbf{f}^f_{\text{int}}\left(\mathbf{U}^f\right) - \mathbf{f}^f_{\text{ext}} + \mathbf{A}^{fT}\boldsymbol{\lambda} = \mathbf{0}, \\ \mathbf{R}^\Gamma\left(\mathbf{U}^c, \mathbf{U}^f\right) = \mathbf{A}^f\mathbf{U}^f - \mathbf{A}^c\mathbf{U}^c = \mathbf{0}. \end{cases} \tag{3.43}$$

Equation (3.43) is a nonlinear equation that needs to be linearised before solving by iterative solvers. The linearisation of the coarse mesh residual $\mathbf{R}^c$ with respect to its variables is given by:

$$\begin{aligned} \bar{\mathbf{R}}^c\left(\mathbf{U}^c + \delta\mathbf{U}^c, \boldsymbol{\lambda} + \delta\boldsymbol{\lambda}\right) = \mathbf{R}^c\left(\mathbf{U}^c, \boldsymbol{\lambda}\right) + \frac{\partial \mathbf{R}^c}{\partial \mathbf{U}^c}\delta\mathbf{U}^c + \frac{\partial \mathbf{R}^c}{\partial \boldsymbol{\lambda}}\delta\boldsymbol{\lambda} = \\ \mathbf{f}^c_{\text{int}}\left(\mathbf{U}^c\right) - \mathbf{f}^c_{\text{ext}} - \mathbf{A}^{cT}\boldsymbol{\lambda} + \mathbf{K}^c_T\delta\mathbf{U}^c - \mathbf{A}^{cT}\delta\boldsymbol{\lambda}. \end{aligned} \tag{3.44}$$

where $\mathbf{K}^c_T$ is the tangent stiffness of the coarse scale problem that was given in Eq. (3.12). The linearisation of the fine mesh residual $\mathbf{R}^f$ and interface residual

$\mathbf{R}^{\Gamma}$ can be done in the same way. Finally a system of linear equations is obtained:

$$\begin{bmatrix} \mathbf{K}_T^c & \mathbf{0} & -p\mathbf{A}^{cT} \\ \mathbf{0} & \mathbf{K}_T^f & p\mathbf{A}^{fT} \\ -p\mathbf{A}^c & p\mathbf{A}^f & \mathbf{0} \end{bmatrix} \begin{Bmatrix} \delta\mathbf{U}^c \\ \delta\mathbf{U}^f \\ \delta\bar{\boldsymbol{\lambda}} \end{Bmatrix} = - \begin{Bmatrix} \mathbf{R}^c \\ \mathbf{R}^f \\ \mathbf{R}^{\Gamma} \end{Bmatrix}. \tag{3.45}$$

Lagrange multipliers, $\boldsymbol{\lambda}$ are replaced by $p\bar{\boldsymbol{\lambda}}$ to avoid uncontrolled increase of the condition number of the system of equations, and $p = \max(|\mathbf{K}_{ii}^c|)$ is a scalar related to the maximum diagonal entry of the initial stiffness matrix of coarse problem and calculated once at the beginning of the simulation [Unger and Eckardt, 2011]. In Eq. (3.45) the external forces $\mathbf{f}_{\text{ext}}^c$ and $\mathbf{f}_{\text{ext}}^f$ are updated at each increment of the time step while the tangent stiffness matrices $\mathbf{K}_T^c$ and $\mathbf{K}_T^f$, and internal forces $\mathbf{f}_{\text{int}}^c$ and $\mathbf{f}_{\text{int}}^f$ are updated at each iteration due to the change in the displacement and the Lagrange multipliers:

$$\mathbf{U}_{|i}^c = \mathbf{U}_{|i-1}^c + \delta\mathbf{U}_{|i}^c, \tag{3.46}$$

$$\mathbf{U}_{|i}^f = \mathbf{U}_{|i-1}^f + \delta\mathbf{U}_{|i}^f, \tag{3.47}$$

$$\boldsymbol{\lambda}_{|i} = \boldsymbol{\lambda}_{|i-1} + \delta\boldsymbol{\lambda}_{|i}, \tag{3.48}$$

where subscripts $|i-1$ and $|i$ indicate the results for the previous iteration and the current iteration respectively.

3.2.3 Convergence Criteria

In the Newton-Raphson iterative schemes, after each increment, the initial residual forces are out of balance, $\mathbf{R}_{|i=0} \neq \mathbf{0}$. The resolution process is stopped when residual forces are smaller than an acceptable tolerance:

$$\frac{\parallel \mathbf{R}_{|i} \parallel}{\parallel \mathbf{R}_{|i=0} \parallel} < \epsilon_{\mathbf{R}}, \tag{3.49}$$

where $\epsilon_{\mathbf{R}}$ is the required relative precisions for the residual forces [Besson et al., 2010]. In the current time step, if the norm of residual force at iteration i, $\parallel \mathbf{R}_{|i} \parallel$,is smaller than a fraction of the norm of initial residual force, $\epsilon_{\mathbf{R}} \parallel \mathbf{R}_{|i=0} \parallel$,

then the Newton-Raphson solver has converged. Depending on the required precision, $\epsilon_{\mathbf{R}}$ can be selected between 10^{-2} to 10^{-12}.

In our problem, the residual and displacements vectors are not homogeneous. Since the Lagrange multipliers are used to couple displacements of the fine and the coarse meshes, the residual force vector is composed of the out of balance vector $\left[\mathbf{R}^c,\ \mathbf{R}^f\right]^T$ and residual of the constraint equation $\mathbf{R}^\Gamma$ which may have values of different orders of magnitude. One must then normalize with predetermined quantities the various components of the residual or displacements vectors before assessing the convergence. In this DDM, the residual of the interface constraint is normalized using a scalar parameter, $\mathbf{R}^{\Gamma *} = p\mathbf{R}^\Gamma$ where $p = \max\left(|\mathbf{K}^c_{ii}|\right)$.

However it is known that $\| \mathbf{R} \| \leq N \max_{j \in \{1,\ \dots\ N\}} (| R_j |)$ where max denotes the maximum, $| R_j |$ and $\| \mathbf{R} \|$ are the absolute jth component and the Euclidean norm of the residual force $\mathbf{R}$ respectively, and N is the total number of components of the residual force. Since the computation of $\max_{j \in \{1,\ \dots\ N\}} (| R_j |)$ is faster than the computation of $\| \mathbf{R} \|$, then a cheaper criterion than one given in Eq. (3.49) can be proposed:

$$\frac{N \max\limits_{j \in \{1,\ \dots\ N\}} | R_j |}{\| \mathbf{R}_{|i=0} \|} < \epsilon_{\mathbf{R}}, \tag{3.50}$$

3.3 Conclusion

In this chapter, the classical computational homogenisation and the domain decomposition multiscale methods were explained. Homogenisation and domain decomposition are two bases for a broad range of multiscale methods in solid and fracture mechanics. In computational homogenisation methods, the macroscopic constitutive relations are implicitly obtained by defining and solving a boundary value problem over a sample of microscale structure called Representative Volume Element (RVE). Incremental macroscopic stress-strain relationship is obtained on-the-fly during the macroscopic solution process by solving the boundary value problem associated with the RVE at each (quadrature) point of the macroscopic problem. The displacement boundary condition of the RVE were strongly defined by the macroscopic strain, and imposed by Lagrange multipliers technique.

Domain decomposition technique was used to simulate polycrystalline material failure by splitting the domain into the fine scale and the coarse scale sub-domains. A strong connection between the non-conforming fine and coarse meshes was accomplished by adopting the Lagrange multipliers technique. The global solution is obtained by solving fine and coarse meshes concurrently. In this sense, domain decomposition technique can be categorised as a concurrent multiscale method [Amini et al., 2009].

In the next chapter, a hybrid multiscale method, a combination of both the homogenisation and the domain decomposition techniques, will be proposed for modelling of fracture in polycrystalline materials. A new criterion for the scale adaptation and the crack propagation will be adapted, and a local arc-length method will be developed to handle the instability involved in the failure of polycrystalline microstructure.

Chapter 4

Solution Procedure

In order to model polycrystalline microstructures, the previous chapter presented a combination of two methods: a hierarchical multiscale method based on computational homogenisation (FE^2), and a concurrent multiscale method based on non-overlapping domain decomposition. The FE^2 method is unable to simulate materials in the region where localisation occurs (the corresponding RVE is in softening regime) or in a region where the homogenisation assumptions are not valid. In other words, when the balance equations of an RVE lose ellipticity, the principle of scale separation is not satisfied for that size of an RVE. Consequently, the averaging theorem on which FE^2 relies is not valid in the corresponding region. In contrast, concurrent multiscale methods can simulate localisation phenomena by splitting the domain into the damaging (or critical regions) and loading regions.

We propose a hybrid method, a combination of the FE^2 method and domain decomposition, which removes these shortcomings. The FE^2 technique is used in the regions of the structure that are in a loading regime, i.e not damaging beyond the material stability limit, where representative volume elements satisfy the principle of scale separation. In the critical regions where localisation occurs, a domain decomposition scheme is used to solve the problem exactly at the scale of the material heterogeneities. In order to control the precision of the simulations, error estimation for the up-scaling strategy is carried out at each step of the time integration algorithm. Based on this estimation, the coarse elements are refined hierarchically where needed. When the homogenisation error exceeds a

critical value the homogenisation step is bypassed, and the corresponding critical region is modelled directly at the microscale. First a zoom-in [Lloberas-Valls et al., 2012] process is performed in which the critical region fully resolved at the microscale using boundary conditions based on the history of displacement of the corresponding coarse elements. The fully resolved region is coupled to the coarse mesh and a relaxation process is performed to eliminate the out-of-balance internal forces due to the replacement of the critical coarse elements by the new finer mesh. Thereafter, the fully resolved region and homogenised region are solved concurrently in the domain decomposition framework (LMPC) which was explained in Section 3.2.1. In order to follow progressive failure, the fully resolved region can be adaptively extended.

Inspired by [Lorentz and Badel, 2004] and [Kerfriden et al., 2011], a local arc-length technique is developed for the multiscale domain decomposition problem which follows the load-displacement curve by imposing a constraint over the maximum increment for the jump of all cohesive interface within the fully resolved regions. This is detailed in the following section.

4.1 Local Arc-length technique

When a cohesive interface fails, two operations are performed simultaneously: the traction at the cohesive interface decreases, and the elastic grains unload. Because the grains are elastic and cohesive crack failure is not ductile, the energy released by unloaded grains provides more energy than necessary for the cohesive crack growth. Also due to the unloading in the elastic region a snap-back behaviour is expected. Therefore, an equilibrium state cannot be found for either an increment of external load or an increment of applied displacement boundary condition (see Fig. 4.1). In another words, load incremental strategy and displacement incremental strategy are not able to trace the solution path in the snap-back regime. The arc-length method is a numerical procedure that is used to follow the solution path in nonlinear problems. This method was originally proposed by [Wempner, 1971] and [Riks, 1972], developed by [Crisfield, 1982] and later modified by several researchers. In the arc-length method, a continuous path of equilibrium can be traced by considering a feasible constraint equation. The

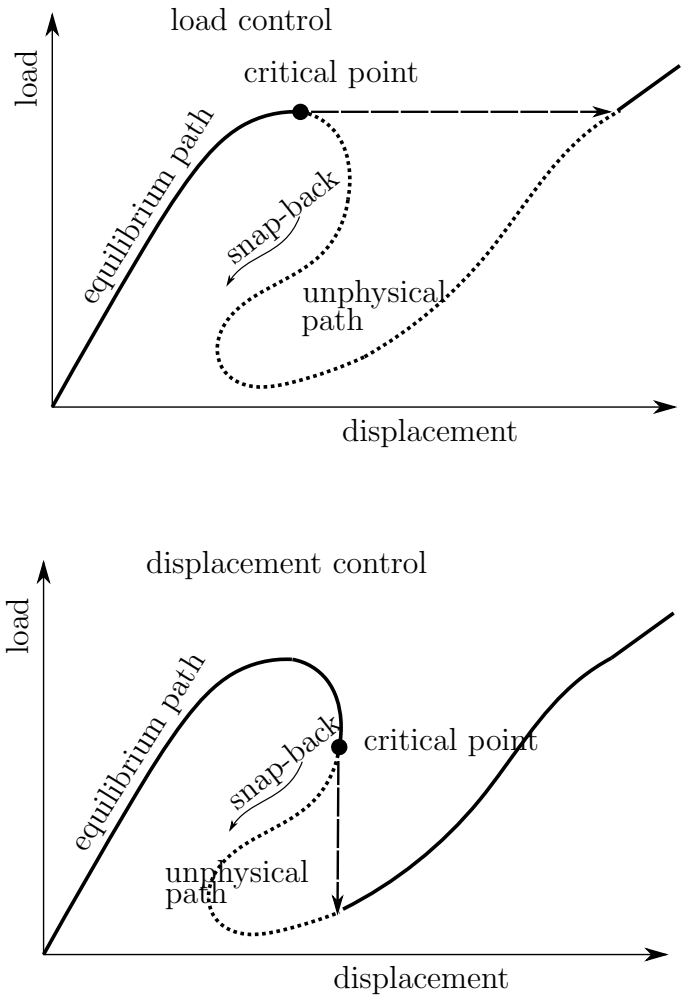

Figure 4.1: Load-displacement equilibrium obtained by the load control and displacement control procedures. The unphysical equilibrium path, shown by dash-line, cannot be followed by the load control and displacement control procedures.

constraint equation adds one unknown variable and one equation to the nonlinear system of equations. Comprehensive reviews of several arc-length methods can be found in [Crisfield, 1997; Geers, 1999]. Two classes of arc-length methods exist. The first group contains global arc-length techniques which define a constraint over the whole of the solution space and can follow smooth load-displacement curves [Crisfield, 1982; Memon et al., 2004]. The second group are called local arc-length methods. They impose a constraint equation on a local region and can trace nonlinear solutions with very sharp snap-back [Schellekens and Borst, 1993; Allix et al., 2010].

In this work, when a fully resolved region occurs in the simulated structure, the incremental force procedure is switched to a local arc-length procedure. In this local arc-length method, a constraint equation is introduced so that at each time step, the maximum local increment in the displacement jump $\Delta[\![\mathbf{u}^f]\!](\zeta_{\mathrm{m}})$ over the mid-point ζ_{m} of all the cohesive elements (whose stiffness is positive) takes a predefined value Δl over the current time step $[t,\ t+\Delta t]$:

$$\forall e \in \Gamma^f, \quad \mathbf{P}_e\ \Delta[\![\mathbf{u}^f_m]\!]_e \leq \Delta l, \tag{4.1}$$

where e refers to the cohesive elements on the cohesive interface Γ^f, and $\mathbf{P}_e = \dfrac{[\![\mathbf{u}^f]\!]_e^T}{\|[\![\mathbf{u}^f]\!]_e\|}$ is the jump direction of the cohesive element e at the last time step $[t-\Delta t,\ t]$. More detail can be seen in Fig. 4.2.

To control the external load at the coarse scale, this constraint is defined at the fine scale and linked to an unknown parameter γ which is the amplitude of the external load $\mathbf{F}$. The constraint equation (4.1) is added to the system of equilibrium equations (3.43), thus the algebraic nonlinear problem to solve, in the concurrent multiscale phase, reads:

$$\begin{cases} \mathbf{R}^c\left(\mathbf{U}^c, \boldsymbol{\lambda}, \gamma\right) = \mathbf{f}^c_{\mathrm{int}}\left(\mathbf{U}^c\right) - \gamma \mathbf{f}^c_{\mathrm{ext}} - \mathbf{A}^{cT}\boldsymbol{\lambda} = \mathbf{0}, \\ \mathbf{R}^f\left(\mathbf{U}^f, \boldsymbol{\lambda}, \gamma\right) = \mathbf{f}^f_{\mathrm{int}}\left(\mathbf{U}^f\right) - \gamma \mathbf{f}^f_{\mathrm{ext}} + \mathbf{A}^{fT}\boldsymbol{\lambda} = \mathbf{0}, \\ \mathbf{R}^\Gamma\left(\mathbf{U}^c, \mathbf{U}^f\right) = \mathbf{A}^f\mathbf{U}^f - \mathbf{A}^c\mathbf{U}^c = \mathbf{0}, \\ \forall e \in \Gamma^f, \quad \mathbf{P}_e\ \mathbf{B}^\Gamma_{e_m} \Delta \mathbf{U}^f_e \leq \Delta l, \end{cases} \tag{4.2}$$

where $\mathbf{B}^\Gamma_{e_m} = \mathbf{B}^\Gamma_e(\zeta_m)$ is the jump extractor matrix for the mid-point of the co-

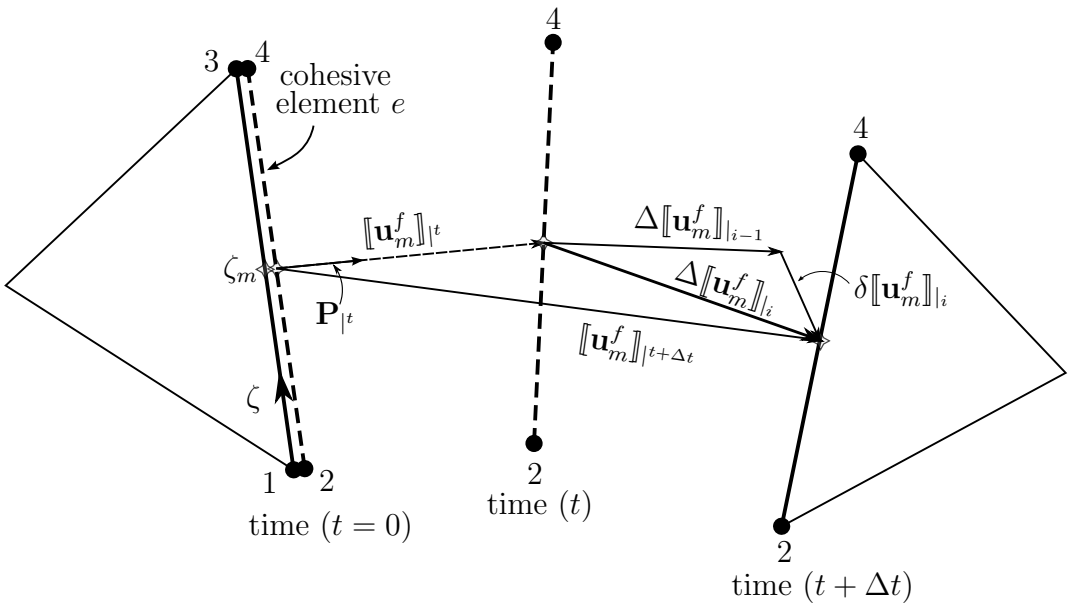

Figure 4.2: The variation of the displacement jump $[\![\mathbf{u}^f]\!]$ at the middle point ζ_m of cohesive element e

hesive element e that is given by Eq. (2.42). According to [Lorentz and Badel, 2004], the nonlinear Eqs. (4.2) can be solved by linearisation of the first three equations, and a direct solution procedure is carried out for the arc-length constraint equation. The linearised form of the equations is given by:

$$\begin{bmatrix} \mathbf{K}_T^c & \mathbf{0} & -p\mathbf{A}^{cT} \\ \mathbf{0} & \mathbf{K}_T^f & p\mathbf{A}^{fT} \\ -p\mathbf{A}^c & p\mathbf{A}^f & \mathbf{0} \end{bmatrix} \begin{Bmatrix} \delta\mathbf{U}^c \\ \delta\mathbf{U}^f \\ \delta\bar{\boldsymbol{\lambda}} \end{Bmatrix} = - \begin{Bmatrix} \mathbf{R}^c \\ \mathbf{R}^f \\ \mathbf{R}^\Gamma \end{Bmatrix} + \begin{Bmatrix} \mathbf{f}_{\text{ext}}^c \\ \mathbf{f}_{\text{ext}}^f \\ \mathbf{0} \end{Bmatrix} \delta\gamma. \tag{4.3}$$

Lagrange multipliers $\boldsymbol{\lambda}$ are replaced by $p\bar{\boldsymbol{\lambda}}$ to avoid the conditioning number of the system of equations being affected by the heterogeneity of the unknown vector. p was introduced in Eq. (3.45). Eq. (4.3) cannot be solved, Because $\delta\gamma$ is unknown, however a relationship between unknown vector on LHS and $\delta\gamma$ can

be found:

$$\begin{Bmatrix} \delta\mathbf{U}^c \\ \delta\mathbf{U}^f \\ \delta\bar{\boldsymbol{\lambda}} \end{Bmatrix} = -\begin{Bmatrix} \mathbf{a}^c \\ \mathbf{a}^f \\ \mathbf{a}^\Gamma \end{Bmatrix} + \begin{Bmatrix} \mathbf{b}^c \\ \mathbf{b}^f \\ \mathbf{b}^\Gamma \end{Bmatrix} \delta\gamma, \tag{4.4}$$

where

$$\begin{Bmatrix} \mathbf{a}^c \\ \mathbf{a}^f \\ \mathbf{a}^\Gamma \end{Bmatrix} = \begin{bmatrix} \mathbf{K}_T^c & \mathbf{0} & -p\mathbf{A}^{cT} \\ \mathbf{0} & \mathbf{K}_T^f & p\mathbf{A}^{fT} \\ -p\mathbf{A}^c & p\mathbf{A}^f & \mathbf{0} \end{bmatrix}^{-1} \begin{Bmatrix} \mathbf{R}^c \\ \mathbf{R}^f \\ \mathbf{R}^\Gamma \end{Bmatrix}, \tag{4.5}$$

and

$$\begin{Bmatrix} \mathbf{b}^c \\ \mathbf{b}^f \\ \mathbf{b}^\Gamma \end{Bmatrix} = \begin{bmatrix} \mathbf{K}_T^c & \mathbf{0} & -p\mathbf{A}^{cT} \\ \mathbf{0} & \mathbf{K}_T^f & p\mathbf{A}^{fT} \\ -p\mathbf{A}^c & p\mathbf{A}^f & \mathbf{0} \end{bmatrix}^{-1} \begin{Bmatrix} \mathbf{f}_{\text{ext}}^c \\ \mathbf{f}_{\text{ext}}^f \\ \mathbf{0} \end{Bmatrix}. \tag{4.6}$$

In order to obtain $\delta\gamma$, the middle line of Eq.(4.4), $\delta\mathbf{U}^f = -\mathbf{a}^f + \mathbf{b}^f\delta\gamma$, is substituted into the arc-length constraint equation (4.2):

$$\forall e \in \Gamma^f, \quad \mathbf{P}_e\mathbf{B}_{e_m}^\Gamma \overbrace{\left(\Delta\mathbf{U}_{e\,|_{i-1}}^f - \mathbf{a}^f + \mathbf{b}^f\delta\gamma\right)}^{\Delta\mathbf{U}_{e\,|_i}^f} \leq \Delta l, \tag{4.7}$$

where at each time step, $\Delta\mathbf{U}^f{}_{|_i} = \Delta\mathbf{U}^f{}_{|_{i-1}} + \delta\mathbf{U}^f{}_{|_i}$ is the total variation of displacement, and $\delta\mathbf{U}^f{}_{|_i}$ is the variation of displacement at the current iteration $|_i$ which was replaced by $-\mathbf{a}^f + \mathbf{b}^f\delta\gamma$ according to Eq. 4.4. Rearranging Eq. (4.7):

$$\forall e \in \Gamma^f, \quad f_e(\delta\gamma) = \mathbf{P}_e\mathbf{B}_{e_m}^\Gamma\left(\Delta\mathbf{U}_{e\,|_{i-1}}^f - \mathbf{a}^f\right) + \mathbf{P}_e\mathbf{B}_{e_m}^\Gamma\mathbf{b}^f\delta\gamma \leq \Delta l, \tag{4.8}$$

where $f_e(\delta\gamma)$ is a linear equation in $\delta\gamma$ which will always yield a value of $\delta\gamma$ that satisfies $f_e(\delta\gamma_e) = \Delta l$. Therefore, for each cohesive element e an admissible domain S_e exists such that:

$$S_e = \{\delta\gamma | \delta\gamma \in \mathbb{R},\ f_e(\delta\gamma) \leq \Delta l\}. \tag{4.9}$$

Finally, the common interval between all admissible intervals S provides an admissible interval S_a for all the cohesive elements which have not been fully damaged:

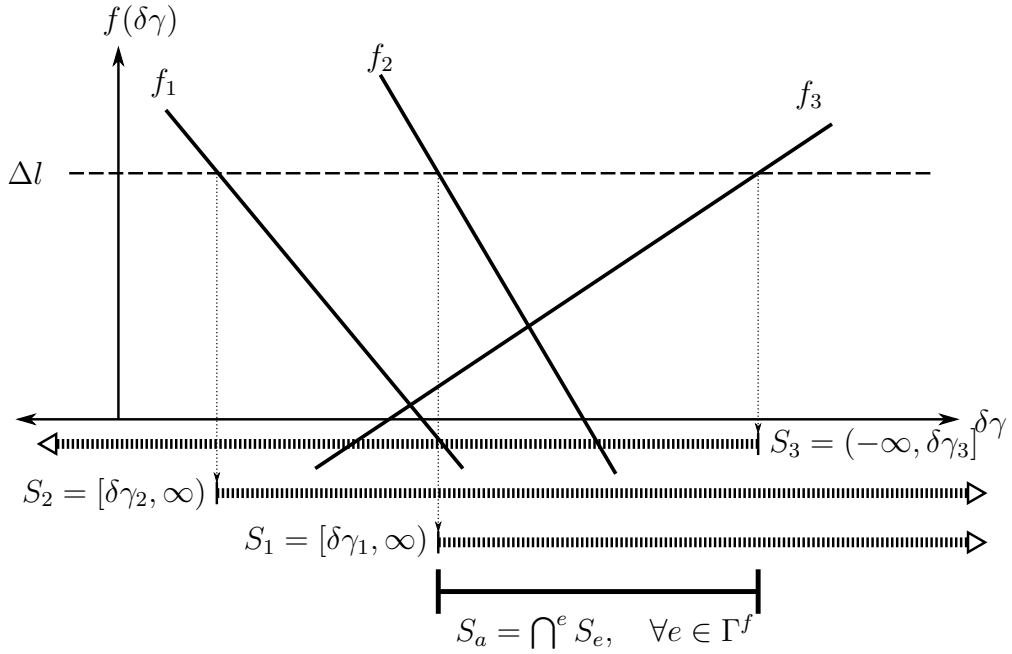

Figure 4.3: The evaluation of the admissible interval S_a for the variational load factor $\delta\gamma$ in the local arc-length method.

$$\forall e \in \Gamma^f, \text{ and } d_e(\zeta_m) < 1, \quad S_a = [\delta\gamma_l,\ \delta\gamma_r] = \bigcap^e S_e. \tag{4.10}$$

where $\delta\gamma_l$ and $\delta\gamma_r$ are the minimum and maximum values of the admissible interval S_a. In fact, the variation of the jump in fully opened cohesive cracks (dead cracks) is not controlled, so their admissible intervals are not considered when determining the global admissible interval S_a. A schematic for the evaluation of the admissible interval of $\delta\gamma$ for all cohesive elements is given in Figure 4.3. However, it is possible that a common interval cannot be found for all active cohesive elements, in which case, this time step is repeated with a slightly different (larger/smaller) value of Δl. A bound for Δl must be considered to avoid very large jumps at cohesive interfaces. Based on the critical displacement jump of cohesive interfaces $[\![\mathbf{u}]\!]_{\text{full}}$ (see Eq. (2.27)), a bound for the maximum variation of displacement jump is determined:

$$0.01[\![\mathbf{u}]\!]_{\text{full}} < \Delta l < [\![\mathbf{u}]\!]_{\text{full}} \tag{4.11}$$

In this local arc-length method, an admissible interval for $[\delta\gamma_l,\ \delta\gamma_r]$ is determined, but the value of $\delta\gamma \in [\delta\gamma_l,\ \delta\gamma_r]$ which minimises the residuals in Eq. (4.2) remains unknown. In this thesis, the maximum variation of load factor $\delta\gamma_r$ is chosen which maximises the load factor γ.

4.2 Error Estimation and Adaptive Mesh Refinement

Errors arisen from the finite element solution of an engineering problem can be categorised into three groups:

- modelling error: This error is related to the mathematical modelling of the problem, e.g. mathematical model for the constitutive relationship and boundary conditions. In FE^2 method, the error in homogenisation can be interpreted as the modelling error.
- discretisation error: This error arises from representing the continuous solution space of the mathematical model by the discretised solution of finite element method.
- solution error: This source of the error is due to the computational process of the finite element solution, e.g. numerical integration.

The finite element method provides an approximation for the exact solution, and the difference between these two solutions is called the discretisation error,e_d , which can usually be reduced by the refinement of elements. Several discretisation error estimators have been developed in the literature which can be classified as *a posteriori* and *a priori* [Ainsworth and Oden, 1997; Bordas and Duflot, 2007]. In this thesis, an *a posteriori* Zienkiewicz-Zhu recovery-based error estimator is adopted to control the coarse scale discretisation error by the local refinement of coarse elements.

In addition to the discretisation error, an FE^2 solution can be polluted by a homogenisation error, e_h, caused by the partial fulfilment of the scale separation assumption, the boundary conditions and the finite element discretisation

of the RVE [Larsson and Runesson, 2011; Temizer and Wriggers, 2011]. In this work, errors emanating from the boundary condition and the finite element discretisation of the RVE are not considered. In first order homogenisation, it is assumed that the macroscopic strain is constant in the vicinity of the sampling point corresponding to each RVE. This assumption is violated in regions with highly localised deformation. In such regions, second order homogenisation can provide more accurate results in comparison to first order homogenisation since the gradient of strain field is not truncated in second order homogenisation. The modelling error indicator for first order homogenisation, proposed by [Temizer and Wriggers, 2011], is adopted to measure the homogenisation error in the FE^2 method. Thereafter, a critical value can be defined for the first order homogenisation error, which controls the scale adaptation procedure.

4.2.1 Homogenisation error

In order to determine the loss of accuracy for first order homogenisation [Temizer and Wriggers, 2011] and [Vernerey and Kabiri, 2012] developed two error indicators. The main concept of their error indicators is based on the difference between the strain energy from second order homogenisation and the strain energy from the first order homogenisation. [Temizer and Wriggers, 2011] solved homogenisation of a hyperelastic unit cell with differing degrees of material heterogeneity, and different deformation and gradient of deformation at the macroscale. By comparing the results from first order and second order homogenisation, they have shown that the major quantity controlling the deviation from a first-order framework is $L_{\mathcal{V}}||\nabla\nabla\mathbf{u}^c||$ which they referred to as the strain-gradient sensitivity. $L_{\mathcal{V}}$ is the size of the RVE, and $||\nabla\nabla\mathbf{u}^c||$ is the L_2 norm of the second gradient of the displacement field that can be written in indicial notation as $||\nabla\nabla\mathbf{u}^c|| = \sqrt{u^c_{i,jk}u^c_{i,jk}}$. Inspiring by [Vernerey and Kabiri, 2012] and [Temizer and Wriggers, 2011], the strain-gradient sensitivity $e_h = L_{\mathcal{V}}||\nabla\nabla\mathbf{u}^c||$ is considered as the error of first order homogenisation e_h by assuming that the effect of microstructure heterogeneity on the homogenisation error is bounded.

Since the second displacement gradient varies proportionally to the inverse of the coarse scale element size $||\nabla\nabla\mathbf{u}^c|| \propto \frac{1}{h}$ [Temizer and Wriggers, 2011], coarse

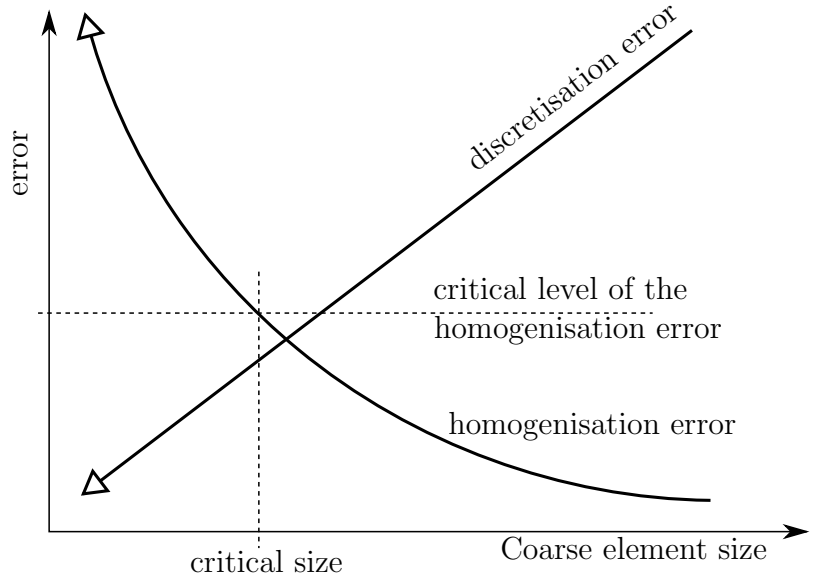

Figure 4.4: The variation of homogenisation error and discretisation error with respect to the coarse element size in FE^2 [Vernerey and Kabiri, 2012].

mesh refinement on the one hand decrease the discretisation error, and on the other hand, increases the homogenisation error. The variation of homogenisation error and discretisation error versus the coarse element size are depicted in Fig. 4.4. In [Vernerey and Kabiri, 2012], a critical size for the coarse element has been defined such that if the size of a coarse element is less than the critical size, then homogenisation is bypassed, since the homogenisation error is beyond the permissible value.

In this thesis, instead of choosing a critical element size, a critical value for the homogenisation error $e_h^{\text{crit}} = 0.01$ is directly considered as a flag for adaptation of scale such that if:

$$L_V ||\nabla\nabla \mathbf{u}^c||_e > e_h^{\text{crit}}, \tag{4.12}$$

then the corresponding coarse element e must be replaced by a model of the background microscopic structure. Due to the coarse linear elements employed in this work, the second gradient of the macroscopic displacement is zero everywhere. Therefore the method proposed in [Temizer and Wriggers, 2011] which relies on a non-zero second displacement gradient, cannot be used directly. To have a non-

zero gradient of strain field at the coarse scale, we propose to adopt the averaging technique used in recovery-based error estimation [Zienkiewicz and Zhu, 1987] to obtain nodal values of the displacement gradient, and consequently, a constant stepwise second displacement gradient is obtained over the coarse elements. The displacement gradient tensor for each element $\nabla \mathbf{u}^c = \frac{\partial u_i}{\partial x_j}$ can be be obtained in vector form:

$$\forall e \in \Omega^c, \quad \nabla \mathbf{u}_e^c = \begin{Bmatrix} \frac{\partial u^c}{\partial x} \\ \frac{\partial v^c}{\partial y} \\ \frac{\partial u^c}{\partial y} \\ \frac{\partial v^c}{\partial x} \end{Bmatrix}_e = \begin{bmatrix} \frac{\partial N_1}{\partial x} & 0 & \frac{\partial N_2}{\partial x} & 0 & \frac{\partial N_3}{\partial x} & 0 \\ 0 & \frac{\partial N_1}{\partial y} & 0 & \frac{\partial N_2}{\partial y} & 0 & \frac{\partial N_3}{\partial y} \\ \frac{\partial N_1}{\partial y} & 0 & \frac{\partial N_2}{\partial y} & 0 & \frac{\partial N_3}{\partial y} & 0 \\ 0 & \frac{\partial N_1}{\partial x} & 0 & \frac{\partial N_2}{\partial x} & 0 & \frac{\partial N_3}{\partial x} \end{bmatrix}_e \begin{Bmatrix} U_1^c \\ V_1^c \\ U_2^c \\ V_2^c \\ U_3^c \\ V_3^c \end{Bmatrix}_e . \tag{4.13}$$

Since linear shape functions are employed, the displacement gradient over each element is constant (see Fig. 4.5). By making use of a simple averaging technique, the nodal value of the displacement gradient tensor are obtained:

$$\bar{\nabla}_I \mathbf{u}^c = \frac{1}{n_I} \sum_{e=1}^{n_I} \nabla \mathbf{u}^c. \tag{4.14}$$

where $\bar{\nabla}_I$ stands for the nodal value of gradient and n_I is the number of elements related to node I.

Then, an approximation of exact displacement gradient can be obtained by interpolating the nodal values of displacement gradient:

$$\forall \mathbf{x} \in \Omega_e^c, \quad \nabla^* \mathbf{u}^c(\mathbf{x}) = \sum_I N_I(\mathbf{x}) \bar{\nabla}_I \mathbf{u}^c, \tag{4.15}$$

where ∇^* indicates the recovery-based gradient, and N_I is the nodal shape function that is being used for displacement interpolation.

Finally, the second displacement gradient can be derived from the recovery-based first displacement gradient field:

$$\forall \mathbf{x} \in \Omega_e^c, \quad \nabla \nabla^* \mathbf{u}^c(\mathbf{x}) = \sum_I \mathbf{B}_I(\mathbf{x}) \bar{\nabla} \mathbf{u}_e^c, \tag{4.16}$$

where $\mathbf{B}_I$ is a matrix that contains the shape function gradients for node I:

$$\mathbf{B}_I = \begin{bmatrix} \frac{\partial N_I}{\partial x} & 0 & 0 & 0 \\ 0 & \frac{\partial N_I}{\partial y} & 0 & 0 \\ \frac{\partial N_I}{\partial y} & 0 & 0 & 0 \\ 0 & 0 & \frac{\partial N_I}{\partial x} & 0 \\ 0 & \frac{\partial N_I}{\partial x} & 0 & 0 \\ 0 & 0 & 0 & \frac{\partial N_I}{\partial y} \\ 0 & 0 & \frac{\partial N_I}{\partial y} & 0 \\ 0 & 0 & 0 & \frac{\partial N_I}{\partial x} \end{bmatrix}, \tag{4.17}$$

and consequently, the second gradient tensor is given in vector form:

$$\nabla\nabla^*\mathbf{u}^c(\mathbf{x}) = \left[\frac{\partial^2 u}{\partial x^2}, \quad \frac{\partial^2 v}{\partial y^2}, \quad \frac{\partial^2 u}{\partial x \partial y}, \quad \frac{\partial^2 u}{\partial y \partial x}, \quad \frac{\partial^2 v}{\partial x \partial y}, \quad \frac{\partial^2 v}{\partial y \partial x}, \quad \frac{\partial^2 u}{\partial y^2}, \quad \frac{\partial^2 v}{\partial x^2}\right]^T \tag{4.18}$$

At the end, the norm of second displacement gradient for each element is approximated by the square root of the inner product of $\nabla\nabla^*\mathbf{u}^c(\mathbf{x})$

$$||\nabla\nabla\mathbf{u}^c|| = \sqrt{\nabla\nabla\mathbf{u}^c : \nabla\nabla\mathbf{u}^c} \simeq \sqrt{(\nabla\nabla^*\mathbf{u}^c)^T \nabla\nabla^*\mathbf{u}^c} \tag{4.19}$$

In Figure 4.5, the evaluation of the second displacement gradient $\dfrac{\mathrm{d}^2 u}{\mathrm{d}x^2}$, corresponding to a linear interpolation of u, is depicted for a one-dimensional problem.

4.2.2 Zienkiewicz-Zhu error estimation

In order to control discretisation error at the coarse scale a simple recovery-based error estimator, proposed by [Zienkiewicz and Zhu, 1987], is employed. The Zienkiewicz-Zhu (ZZ) technique is chosen since it is a computationally cheap *a posteriori* error estimator that can easily be incorporated into existing finite element codes. In the ZZ approach, to calculate the error, an approximation for the exact solution is determined by using an averaging technique. After solving finite element problems, a point-wise definition of strain and stress errors at the

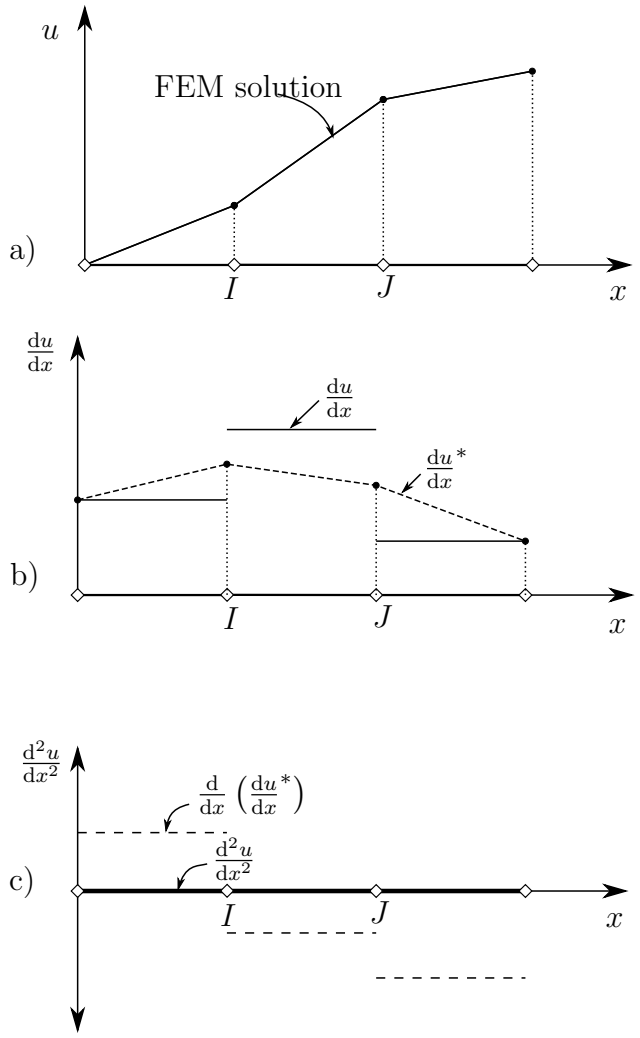

Figure 4.5: First displacement gradient, $\nabla\mathbf{u}$, second displacement gradient, $\nabla\nabla\mathbf{u}$, and the recovery-based second displacement gradient, $\nabla\nabla^*\mathbf{u}$, for a one-dimensional problem and linear shape functions.

coarse scale point $\mathbf{x} \in \Gamma^c$ are given by

$$\mathbf{e}_\varepsilon(\mathbf{x}) = \boldsymbol{\varepsilon}^*(\mathbf{x}) - \boldsymbol{\varepsilon}^c(\mathbf{x}) \ , \tag{4.20}$$

$$\mathbf{e}_\sigma(\mathbf{x}) = \boldsymbol{\sigma}^*(\mathbf{x}) - \boldsymbol{\sigma}^c(\mathbf{x}) \ , \tag{4.21}$$

where $\mathbf{e}_\varepsilon$ and $\mathbf{e}_\sigma$ are the approximated error in the strain and stress fields, respectively, and $\boldsymbol{\varepsilon}^c$ and $\boldsymbol{\sigma}^c$ are the strain and stress obtained from the finite element solution at the coarse scale. $\boldsymbol{\varepsilon}^*$ and $\boldsymbol{\sigma}^*$ are the approximations of the exact strain and stress which are obtained by interpolating over the nodal values of strain and stress:

$$\forall \mathbf{x} \in \Omega_e, \quad \boldsymbol{\varepsilon}^*(\mathbf{x}) = \mathbf{N}_e(\mathbf{x})\bar{\boldsymbol{\varepsilon}}_e, \tag{4.22}$$

$$\forall \mathbf{x} \in \Omega_e, \quad \boldsymbol{\sigma}^*(\mathbf{x}) = \mathbf{N}_e(\mathbf{x})\bar{\boldsymbol{\sigma}}_e, \tag{4.23}$$

where $\mathbf{N}_e$ is the matrix of shape functions for the coarse element e, and the nodal averages of stress and strain are denoted by $\bar{\boldsymbol{\sigma}}_e$ and $\bar{\boldsymbol{\varepsilon}}_e$ for the nodes of element e. In order to determine the nodal values of stress $\bar{\boldsymbol{\sigma}}$ and strain $\bar{\boldsymbol{\varepsilon}}$ several methods have been proposed in literature [Zienkiewicz and Zhu, 1992; Boroomand and Zienkiewicz, 1997; Yazdani et al., 1998]. In this thesis, a simple averaging technique is used to obtain the nodal value of stress and strain. For example, nodal stress $\bar{\boldsymbol{\sigma}}_I$ at node I is obtained by averaging the stress over all corresponding elements:

$$\bar{\boldsymbol{\sigma}}_I = \frac{1}{n_I} \sum_{e=1}^{n_I} \boldsymbol{\sigma}_e^c. \tag{4.24}$$

Finally the energy norm of the error for the coarse domain is given by:

$$\forall e \in \Omega^c, \quad ||\mathbf{e}|| = \left(\sum_e ||\mathbf{e}||_e^2 \right)^{\frac{1}{2}}, \tag{4.25}$$

where the energy norm of the error for element e is determined by

$$||\mathbf{e}||_e^2 = \int_{\Omega_e^c} \mathbf{e}_\sigma^T \mathbf{e}_\varepsilon \ \mathrm{d}\Omega \tag{4.26}$$

where $\mathbf{e}_\varepsilon$ and $\mathbf{e}_\sigma$ are defined in Eqs. (4.20) and (4.21), respectively.

The energy norm of error $||\mathbf{e}||$ is normalised by a weighted energy of the system to obtain the relative percentage error η:

$$\eta = \frac{||\mathbf{e}||}{\sqrt{||\mathbf{u}||^2 + ||\mathbf{e}||^2}} \times 100\%, \tag{4.27}$$

where the weighted energy of the system is given by:

$$||\mathbf{u}|| = \left(\int_{\Omega^c} \boldsymbol{\sigma}^{*T} \boldsymbol{\varepsilon}^* \, \mathrm{d}\Omega \right)^{\frac{1}{2}}. \tag{4.28}$$

A maximum permissible error $\bar{\eta}$ is defined, and the following condition is checked after each time step:

$$\eta \leq \bar{\eta}. \tag{4.29}$$

If the condition above is satisfied, the next time step can be started, otherwise, a mesh refinement procedure is triggered.

4.2.3 Coarse mesh refinement procedure

After convergence of the hybrid multiscale problem at each time step, the ZZ approach is used to measure the energy norm of the error at the coarse mesh. If the inequality (4.29) is not satisfied one must determine which elements to refine. According to the ZZ procedure, the following inequality

$$\frac{||\mathbf{e}||_e}{\bar{e}_m} > 1, \tag{4.30}$$

defines the coarse elements which are to be refined, where $||\mathbf{e}||_i$ is defined in Eq. (4.26), and

$$\bar{e}_m = \bar{\eta} \left(\frac{||\mathbf{u}||^2 + ||\mathbf{e}||^2}{m} \right)^{\frac{1}{2}} \tag{4.31}$$

and m is the number of coarse elements. The elements which satisfy (4.30) are refined by splitting into four smaller elements. In order to have a compatible mesh, the adjacent elements are also split. In Fig. 4.6, the coarse mesh refinement is depicted. In the adaptive multiscale method after each mesh refinement some

modification is required before starting a new time step:

- RVEs corresponding to the parent elements are copied to the new, finer elements,
- matrix $\mathbf{A}_c$ used in Eq. (3.42) must be recomputed in order to be compatible with the new configuration of nodes on the interface of coarse-fine meshes.
- the homogenisation error is computed and the scale adaptation condition (4.12) is checked.
  - if $e_h \leq e_h^{\text{crit}}$ the microstructure adaptation is bypassed,
  - if $e_h > e_h^{\text{crit}}$ the coarse element i is replaced by an explicit representation of the microstrcuture. The adaptation of fully resolved regions is explained in the next section.
- after mesh refinement or microstructure adaptation the residual force will be out of balance due to disturbances in the internal force. Thus, a relaxation procedure is required to minimise the residual force before starting the next time step. See Section 4.3.2.

4.3 Adaptive expansion of fully resolved region

The fully resolved regions are adaptively expanded to the new critical zones where the coarse elements have a modeling error $e_h > e_h^{\text{crit}}$ or when their corresponding RVEs have already lost the stability. Figure 4.7 demonstrates the procedure of the development of a fully resolved region schematically. The procedure is slightly different for the initiation of a fully resolved region than the extension of it. A five-step zoom-in procedure can be employed for the extension of an existing fully resolved region (the right column in Fig. 4.7), while the third step can be skipped for the initiation of the fully resolved region (the left column in Fig. 4.7).

A zoom-in procedure is started when a critical zone appears at the coarse scale due to the high homogenisation error. The underlying microstructre of the critical zone is determined by opening a window to the actual microstructure. It

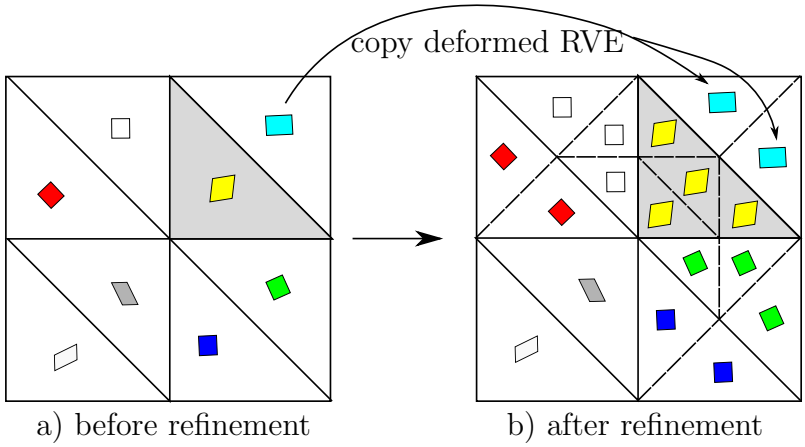

Figure 4.6: Coarse mesh refinement in FE^2 method, and copying the RVEs from old mesh to the new mesh. An edge bisection method is used. The deformed quadrilaterals represents the underlying RVE corresponding to each coarse element.

is assumed that the actual geometry of the microstructure is known *a priori*. In the third step, if the new critical zone is an extension to an existing fully resolved region, then those grains that are common between the existing fully resolved region and its extension are attached to the extension part, and all related data are dismissed. In the fourth step, the extension part is meshed in such a way that the mesh is compatible with the adjacent coarse mesh and fully matches with the adjacent fully resolved regions. The fourth step also consists of an equalisation process that solves the new fully resolved region boundary value problem based on the history of displacement field that has been experienced by the critical zone. Equalisation process is detailed in Section 4.3.1. At the end of equalisation process, the displacement field of the new fully resolved region is compatible with the surrounding meshes, and the level of energy saved in the high resolution region is approximately equal to the amount of strain energy in the coarse elements before adaptation. The equalisation process will be explained in the next section. In the next step, the Linear Multiple Point Constraint (LMPC) technique is used to couple the the new fully resolved region to the rest of the domain. Finally, before continuing the simulation, a relaxation procedure is performed to minimise the out-of-balance residual force as described in Section 4.3.2.

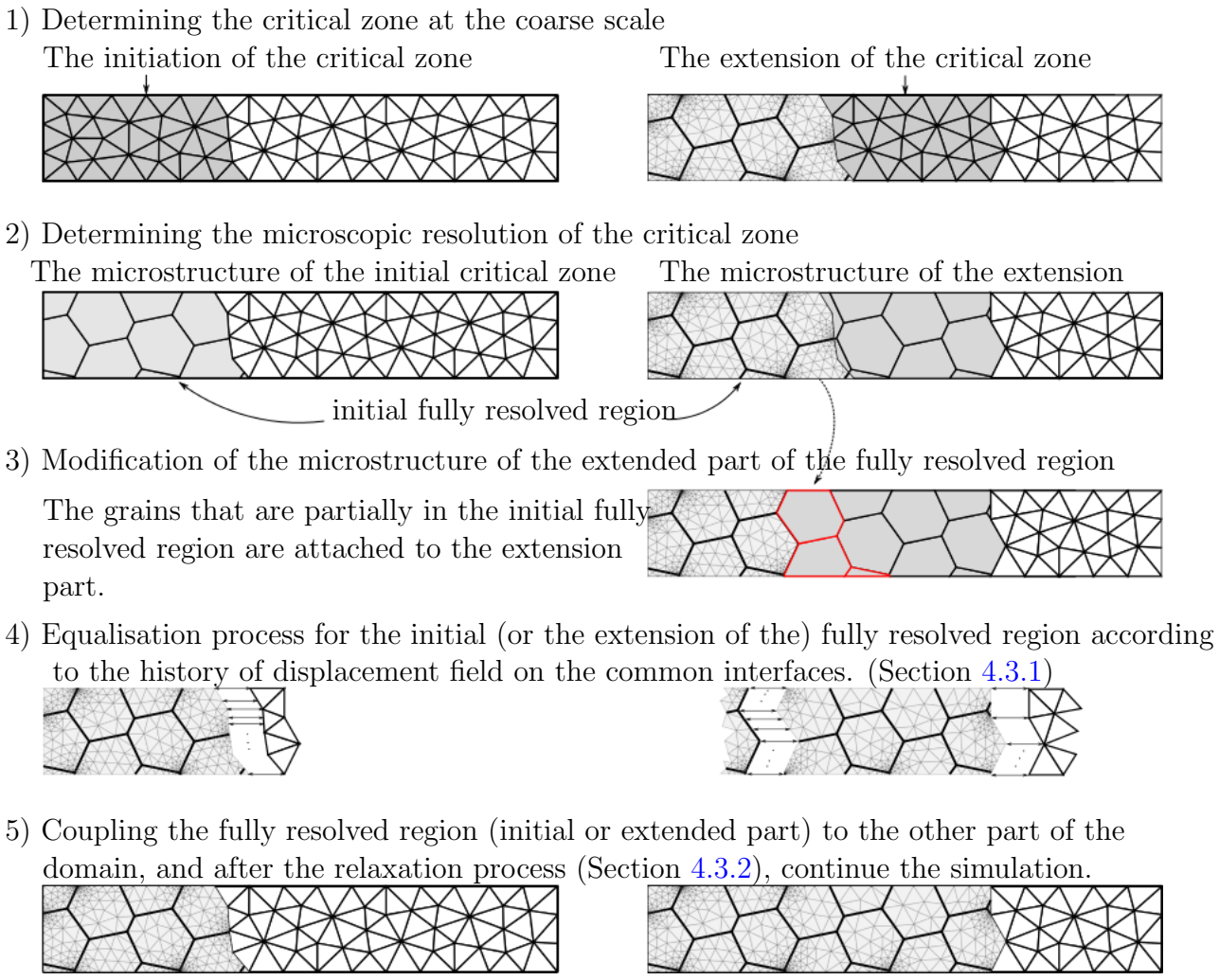

Figure 4.7: The procedure of the development of the fully resolved region

4.3.1 Equalisation process

When the critical coarse elements are replaced by a fully resolved region, it is necessary to ensure that the high resolution region and critical coarse elements have equivalent strain energy and deformation states. In our problem, the two physical models are equivalent if the level of damage, or more precisely, their capacity to store strain energy with the same deformed shape, are equal. The undamaged microstructure saves more strain energy rather than the coarse scale critical zone due to its un-degraded stiffness. The equalisation process is performed to acquire

an approximately equivalent fully resolved region. In the equalisation process, a BVP is defined for the undamaged high resolution domain. The boundary conditions are defined from the displacements experienced by the critical zone during the simulation up until the current time step ($t \in [0, \tau]$). Figure 4.8 illustrates equalisation process for a fully resolved region based on the displacement history of the critical zone. For linear elastic microstructures, the whole history of displacement can be imposed by a single time step only since the material capacity for storing strain energy is not changed by loading. Similar to Section 3.2.1, the LMPC method is adopted to impose the displacement boundary conditions. At this stage, no arc-length technique is required since the external load (displacement history) is known for all previous time steps. After accomplishment of the equalisation process, the fully resolved region is embedded into the coarse scale by making use of the LMPC technique. The coupling technique between the fine and the coarse meshes was explained in Section, 3.2.1.

4.3.2 Relaxation

After the equalisation process, the embedding of the fully resolved region into the coarse scale, and before starting the new time step, the residual force vector must again again be minimised. After every mesh refinement or adaptation of the high resolution scale, the internal forces change. Therefore, the simulation is continued at the current time step until the norm of the residual force vector reduced to a certain permissible value (see Section 3.2.3).

4.4 Conclusion

After introducing a hierarchical multiscale method based on the computational homogenisation (FE^2), and a concurrent multiscale method based on the non-overlapping domain decomposition in Chapter 3, a hybrid multiscale method was proposed and detailed in this Chapter. The proposed method is a smart combination of the FE^2 and domain decomposition in which the both dicretisation and homogenisation errors are controlled. To control the discretisation error at the coarse scale, the coarse mesh is adaptively refined based on an *a posteriori*

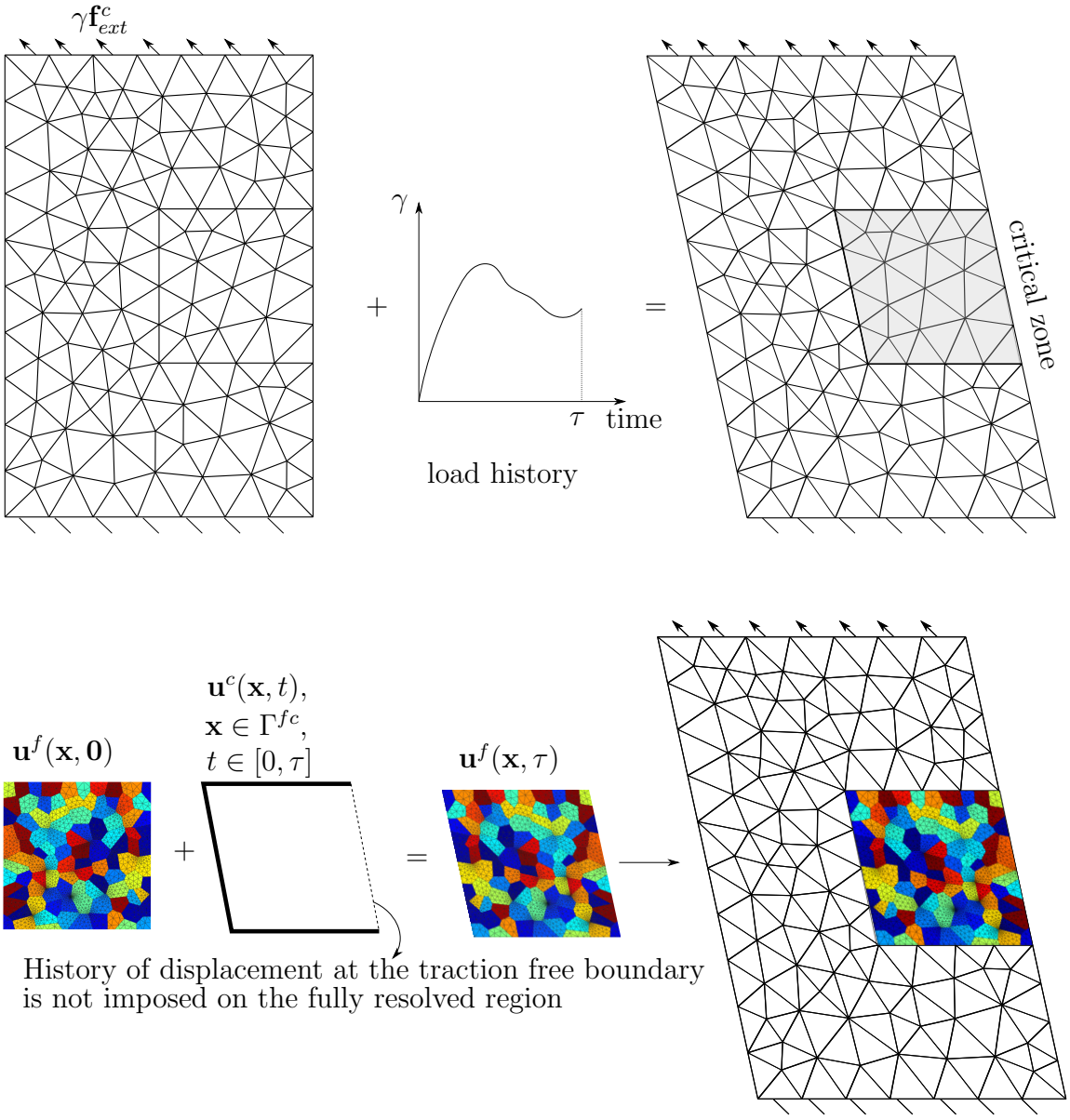

Figure 4.8: Solving the fully resolved region using a boundary condition based on the displacement history of the corresponding critical zone.

error estimator. A mapping procedure was defined to copy data from the parent elements to the new elements. We also designed a procedure for adaptive expansion of the microstructure in the coarse mesh which consequently allows the coalescence and propagation of micro-cracks in the macro scale domain. The extension of microscopic region is triggered if the homogenisation error in a coarse element reaches a critical value. Difference between the average of strain energy density in the second order homogenisation and the first order homogenisation provides an indicator for the error in our homogenisation model. To calculate the homogenisation error, the second gradient of coarse scale displacement field is required. Since the second gradient of displacement in the linear element are always zero, a smoothing process was carried out on the first gradient of displacement to obtain a non-zero field for the second gradient of displacement. The propagation of microstructure in the coarse scale requires to design some preprocessing tasks: zoom-in, equalisation and relaxation which were explained in this Chapter. A local arc-length technique was also developed for the multiscale domain decomposition problem that can robustly follow the load-displacement curve by imposing a constraint over the maximum increment of the jump of all cohesive cracks within the fully resolved regions.

Chapter 5

Example Applications

In this chapter, the proposed adaptive multiscale method for polycrystalline failure presented in Chapters 3 and 4 is tested. First, the size of RVE used in the FE^2 is determined by performing a statistical study. Then, a notched beam under uniaxial load is considered as a test case for the adaptive multiscale method. A direct numerical solution (DNS) where the whole microstructure is explicitly simulated over the whole computational domain for comparison of the results.

5.1 Determining the size of RVE

Numerical-statistical method is used to determine the RVE size. In the literature, several definitions can be found for RVEs. Depending on the definition it may lead to different permissible size for the RVE. According to [Gitman et al., 2007], for a non-periodic microstructure, RVE is a "*volume containing a very large (mathematically infinite) set of micro-scale elements (e.g. grains), possessing statistically homogeneous and ergodic properties*". In other words an RVE must be large enough to ensure that it statistically contains all heterogeneities of the microscale and also its behaviour is independence of the microscopic boundary conditions. However the increment in the size of an RVE should not lead to changes in the macroscopic material properties. From the aspect of computational efficiency, it is preferred to have as small an RVE as possible while still conserve the admissible level of modelling error. In this study, a non-regular

Table 5.1: Material properties and parameters for grain and cohesive interfaces at the microscale.

grain			cohesive interface			
E	ν	l_g	$\sigma_{\max} = \tau_{\max}$	$G_{Ic} = G_{IIc}$	κ_{ini}	n
384.6GPa	0.237	25μm	1 GPa	35 Jm^{-2}	0	0.5

shape RVE with periodic structure is considered (see Fig. 5.1). The microstructure properties have been defined in Chapter 2. In order to find the minimum possible size, a statistical analysis is performed by considering the various RVE sizes. For each RVE size, in addition to the stress-strain curves, the yield surface of RVEs is analysed. To determine the yield surface for a range of biaxial displacement loads (from compressive to tensile), macroscopic strains are imposed on each RVE.

A range of different RVE sizes from 4 to 256 grains are considered in the numerical-statistical analysis. Figure 5.1 shows the RVEs with 4, 9 and 36 grains with and without their finite element mesh.

Polycrystalline alumina, Al_2O_3, was chosen to be studied in this thesis. The material properties of bulk grains and cohesive interfaces are given in table 5.1 [Shabir et al., 2011]. In Table 5.1, E is the Young's modulus and ν is the Poisson's ratio of bulk grains. The average size of grains is l_g (see 36-grain RVE in Fig. 5.1). The normal strength $\sigma_{\max}$, tangential strength $\tau_{\max}$, damage initiation parameter κ_{ini}, and traction-separation shape parameter n of cohesive interfaces were introduced in Chapter 2. The effect of n on the traction-separation law was shown in Fig. 2.6.

Figure 5.2 shows the results of the statistical analysis on the macroscopic yield surface that are obtained from the failure point of RVEs with different size . Each yield surface is obtained by imposing a varying macroscopic strain tensor from compressive to tensile configuration. The variation of the macroscopic strain vector $\boldsymbol{\varepsilon}^c$ at each time step is given by:

$$\Delta\boldsymbol{\varepsilon}^c(\theta) = \frac{[\![u^f]\!]_{\text{full}}}{2L_{\mathcal{V}}} \begin{Bmatrix} \cos(\theta) \\ \sin(\theta) \\ 0 \end{Bmatrix}, \quad -\frac{5\pi}{12} \leq \theta \leq \frac{\pi}{4}, \tag{5.1}$$

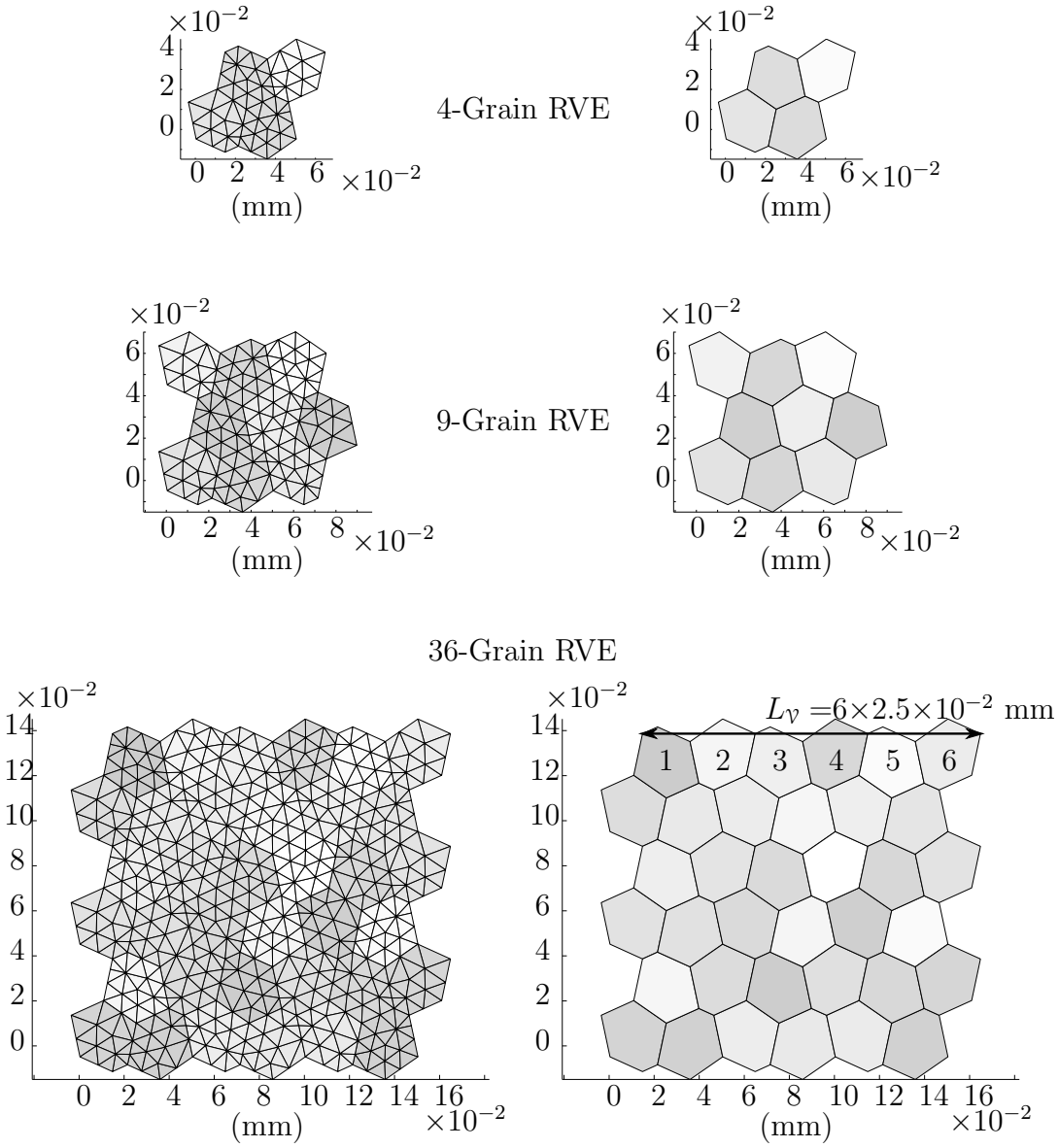

Figure 5.1: Different size of non-regular RVEs. The sizes are in mm.

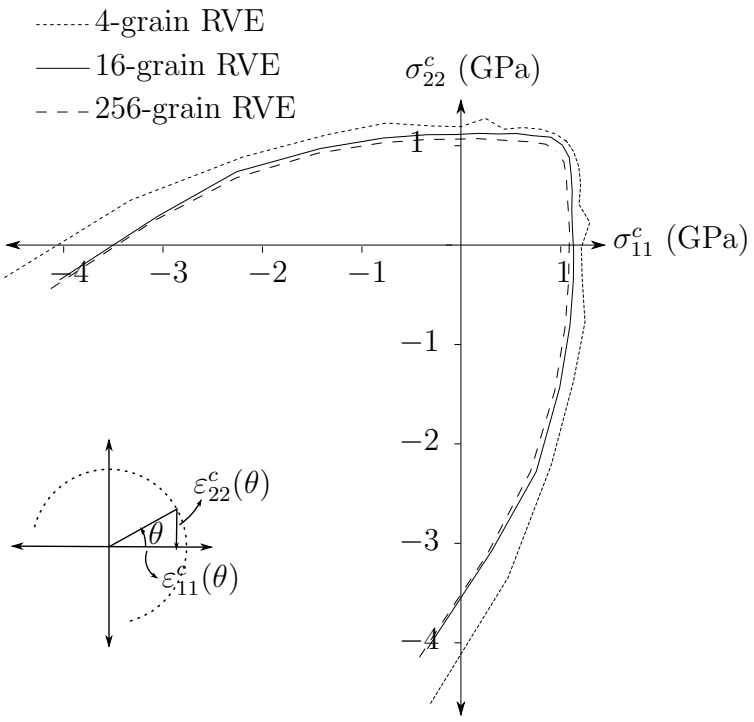

Figure 5.2: Macroscopic yield surface obtained form different size of RVEs.

where $L_\mathcal{V}$ is the average size of the RVE (see Fig. 5.2), and $[\![u^f]\!]$ is the minimum jump corresponding to the fully damaged interface which is given by Eq. (2.27). Due to the symmetry of the problem, only half of the yield surface is computed. For each configuration θ, the computational homogenisation is performed in several time steps until the RVE loses stability. The macroscopic yield surface is given by principal stresses (σ_{11} and σ_{22}) that are obtained by homogenisation of the RVE one step before failure (see Eq. (3.30)). It can be deduced from the results that the size of the RVE does not have significant influence on the failure surface for RVE with more that 16 grains.

To determine the RVE size, the macroscopic stress-strain curves are traced by homogenising different size of RVEs. To obtain these curves, a biaxial macroscopic strain $\boldsymbol{\varepsilon}^c = [\varepsilon_{xx},\ \varepsilon_{yy} = \varepsilon_{xx},\ \varepsilon_{xy} = 0]^T$ is gradually imposed onto the RVEs. The results are illustrated in Fig. 5.3. Accordingly, the smaller the RVE, the stiffer the response. This behaviour is due to the strong Dirichlet boundary conditions imposed upon the RVE that do not allow the cohesive cracks to open along the

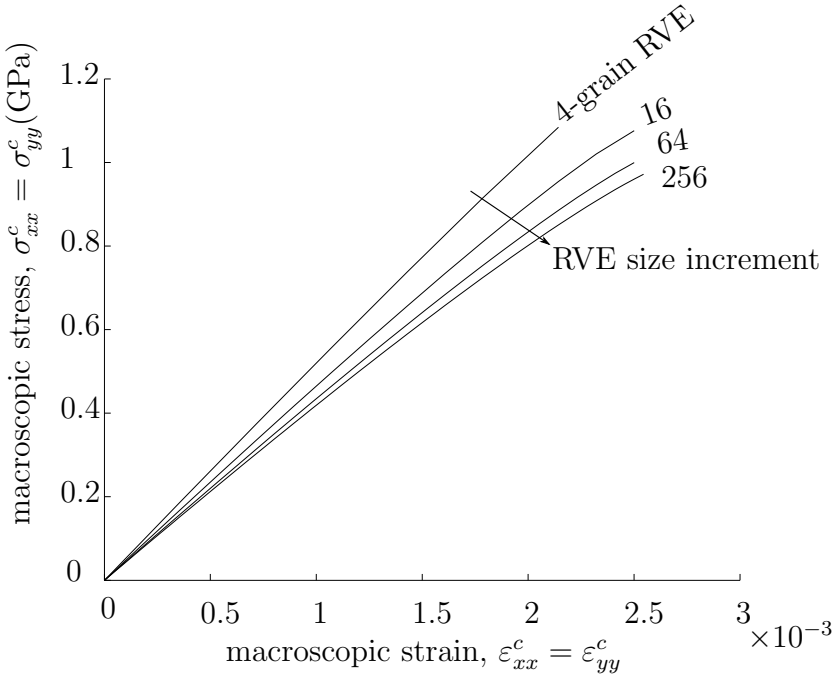

Figure 5.3: Macroscopic stress-strain curve.

boundary. However, by increasing the size of the RVE, the effect of the boundary conditions reduces.

The ratio of dissipated energy in each RVE before material instability (Chapter 6 of [Ogden, 1997]) are illustrated in Figure 5.4. The ratio of dissipated energy is obtained by dividing the total dissipated energy by the total work done by the external load. From the figure, it can be seen that the the ratio of dissipated energy for RVEs with 16 grains is 12.3% less than 256-grain RVE, while this value for the 9-grain RVE is 35% less than it for the RVE with 256 grains. As matter of fact, the stiff boundary condition of the RVE refrains the cohesive interfaces on the boundary to dissipate energy. By increasing the RVE size, the effect of the boundary condition reduces.

The macroscopic Young's Modulus obtained form the secant tangent of stress-strain curve at yielding point is shown in Fig. 5.5. The effective Young's modulus for the biaxial load is obtained by:

$$E = \frac{\sigma^c_{xx}}{\varepsilon^c_{xx}}|_{\text{failure point}}, \tag{5.2}$$

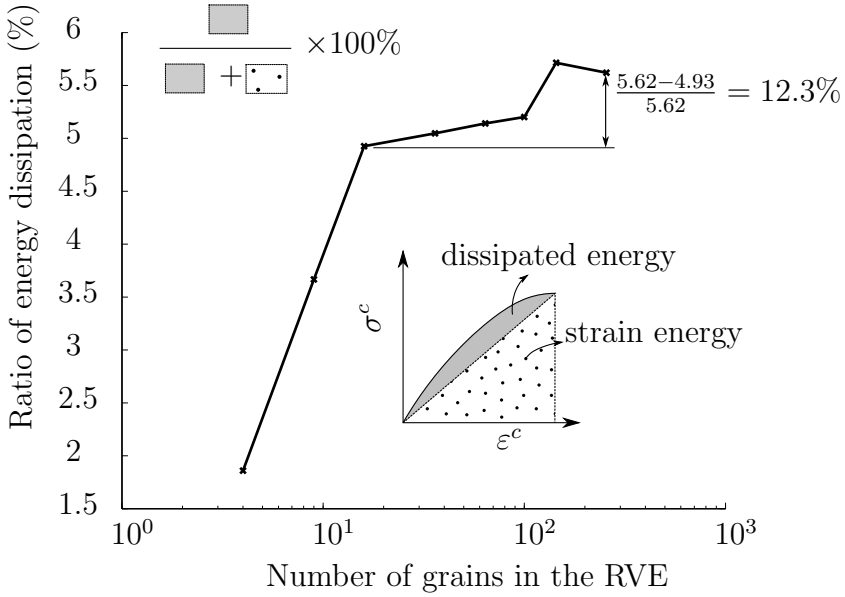

Figure 5.4: The ratio of energy dissipation increases by increasing the RVE size. The average grain size is maintained constant ($l_g = 25\mu$m).

A relative error in Young's modulus is also given in Fig. 5.6 which indicates the relative difference between the Young's modulus of the largest RVE E_{256} to the Young's modulus of a particular RVE. These results show that the macroscopic Young's modulus converges fast with increasing size of the RVE, and the rate of convergence decreases by increasing the size of RVE.

In the rest of this thesis, an RVE with 16 grains is used to obtain homogenised constitutive relations at the coarse scale. According to Fig. 5.6, although the relative differences in the Young's modulus of a 16-grains RVE is 12.7% with respect to the 265-grains RVE, the former is almost 16 times faster in terms of computational time. As shown in Fig. 5.4, the 16-grain RVE dissipates 12.3% of the external work in comparison to the 256-grain RVE before losing stability.

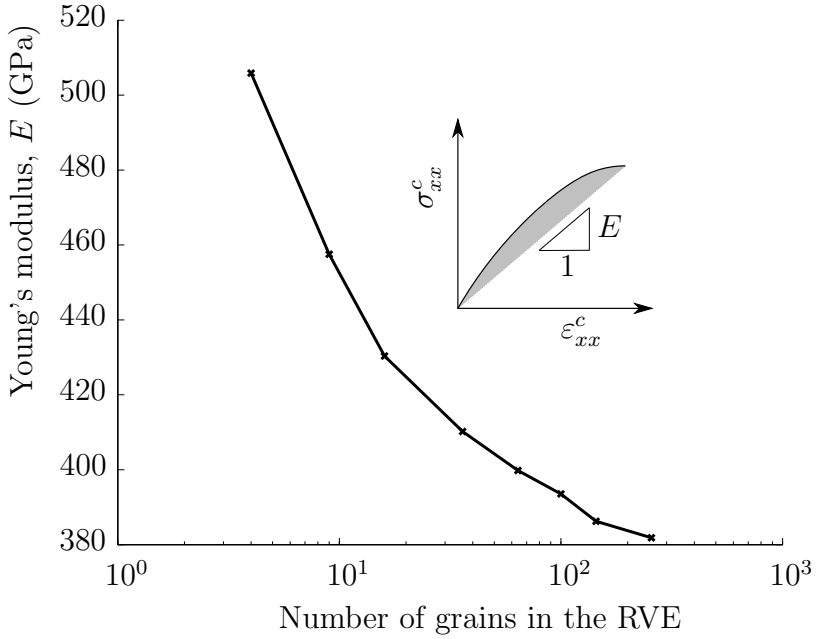

Figure 5.5: Macroscopic Young's modulus obtained from homogenisation of RVEs under biaxial load.

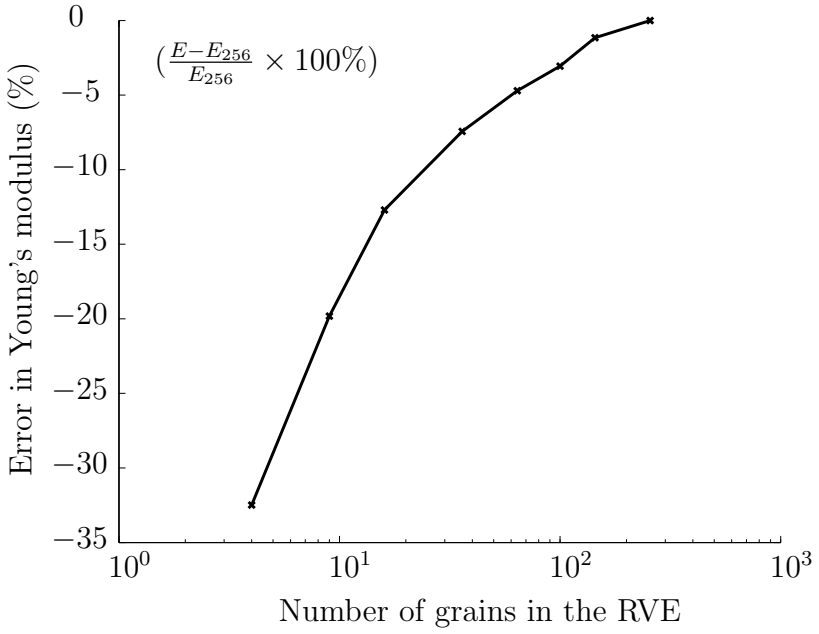

Figure 5.6: Relative error in the macroscopic Young's Modulus.

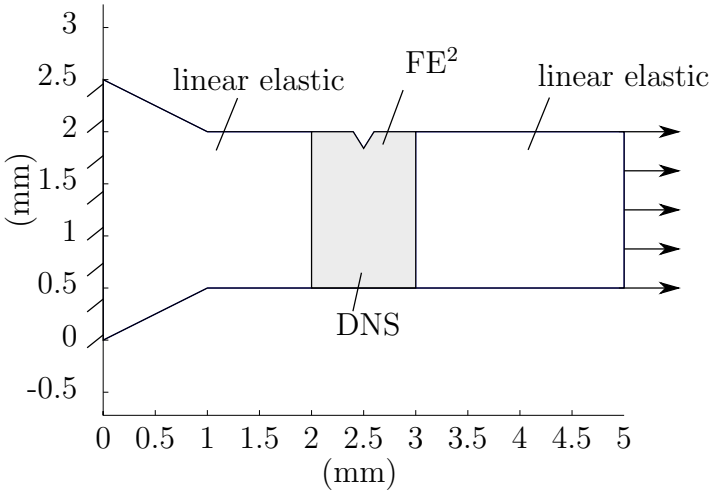

Figure 5.7: A single-notched beam under uniaxial tensile load.

5.2 Numerical Example

5.2.1 Notched Beam

As an example, a single-notched beam under uniaxial load is considered, shown in Fig. 5.7. The results from the proposed multiscale framework are compared to those from a direct numerical solution (DNS). The beam is made of a polycrystalline material, for which the constitutive equations were introduced in Chapter 2, and the mechanical properties of the grains are given in Table 5.1. In order to decrease the computational cost, the FE^2 method is only implemented in the middle part of the beam (grey region in Fig. 5.7), and a constant linear elastic homogenised model with Young's modulus $E = 386.4$ GPa and Poisson's Ratio $\nu = 0.237$ is considered for the rest of the domain. Furthermore, for the DNS problem, only the middle region is resolved at the microscale.

Distribution of the von Mises stress over the notched beam are shown in Fig. 5.8 for the DNS and the adaptive multiscale solution. Not perfectly matching but a very similar distribution of the von Mises stress can be seen in both cases. The maximum stress appeared at the crack tip as expected. Note that in the cohesive interface models, the crack tip stress is not infinite, and it is related to the maximum failure stress of the cohesive interface (see Eq. (2.26)).

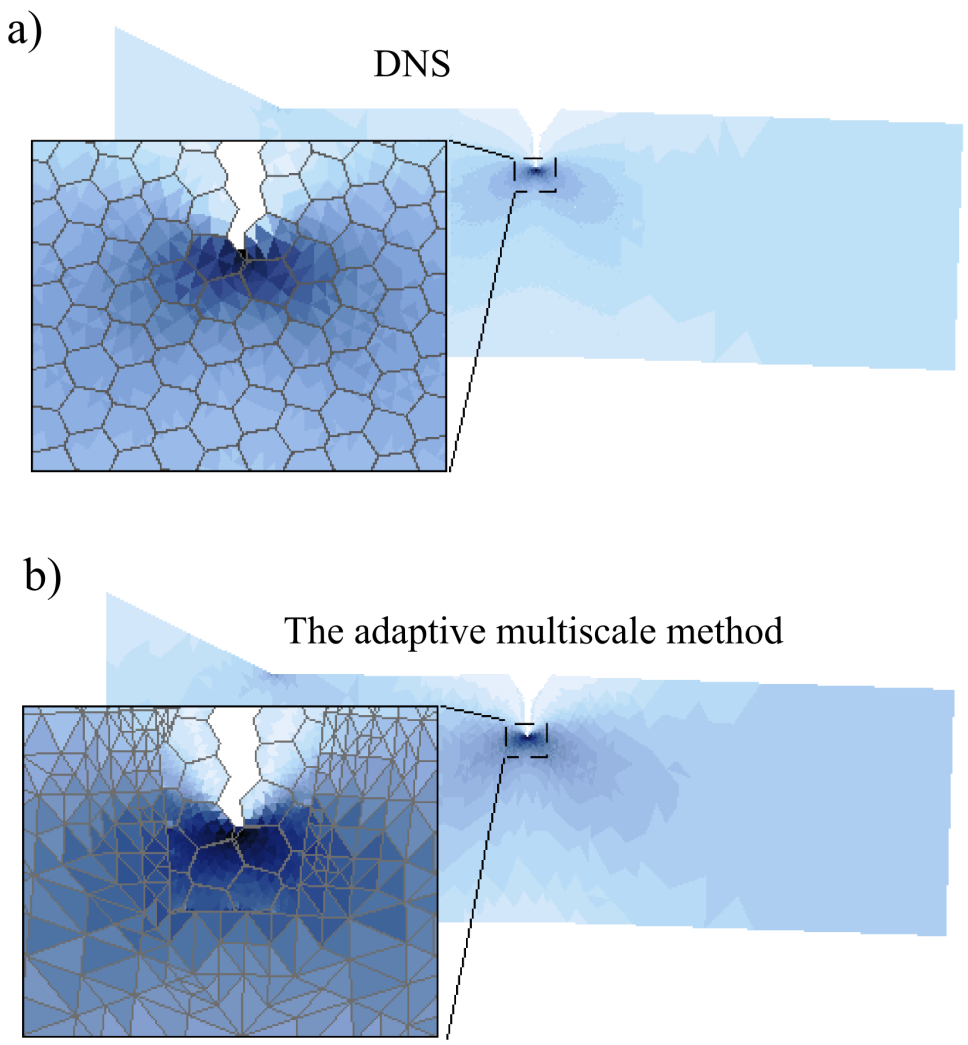

Figure 5.8: von Mises stress distribution in the notched bar a) DNS, b) Adaptive multiscale solution. Deformation is magnified by 100.

As explained in Chapter 4, the ZZ error estimator is employed for the control of the discretisation error, and the strain-gradient sensitivity is used as a measurement for the homogenisation error. The maximum permissible discretisation error is $\bar{\eta} = 5\%$. If the strain-gradient sensitivity of a coarse element $L_V||\nabla\nabla\mathbf{u}^c||_e$ is higher than the critical value of the homogenisation error then the microstructure is fully resolved for that element. In this study, $e_h^{\text{crit}} = 0.01$ is considered as the critical value of homogenisation error. The value of critical error is needed to be investigated in the future studies.

The distribution of the strain-gradient sensitivity of the coarse mesh is illustrated in Fig. 5.9. The homogenisation error is small at the beginning of the simulation. By increasing the load, homogenisation error increases at the notch point, and consequently the coarse elements with high error are replaced by the underlying microstructure (Time steps>5). Continuing the simulation, cracks are initiated and propagate through the grain boundaries. Microscopic crack direction is implicitly defined by solving the equilibrium equations. It is observed that the mostly the coarse elements in the vicinity of the crack tip have the high strain-gradient sensitivity (the homogenisation error). As shown in this figure, this homogenisation error indicator can accurately predict the most likely direction of the crack propagation before inserting the microstructure, which is the main advantage of this scale adaptation criterion. In the literature, the length scale ratio [Unger and Eckardt, 2011; Ghosh et al., 2007] have been used as the scale adaptation criterion in multiscale fracture modelling. This usually lead to a large fully resolved region at the coarse scale. In scale adaptation based on the length scale ratio, if the ratio of the coarse element size to the RVE size is less than a critical value, then the microstrucute is directly resolved at those elements.

In Fig. 5.10, the coarse mesh in the vicinity of the fully resolved region is shown. Although some coarse elements are smaller than the size of a grain, which means that they are at the same scale, according to the homogenisation error criterion, it is still allowed to employ the FE^2 method. It is worth to mention that, if scale size ratio was used as scale adaptation criterion, the most of these coarse elements in the vicinity of the microscopic region must be fully resolved at the microscale, while the strain-gradient sensitivity of those elements is still less that the critical value $e_h^{\text{crit}} = 0.01$.

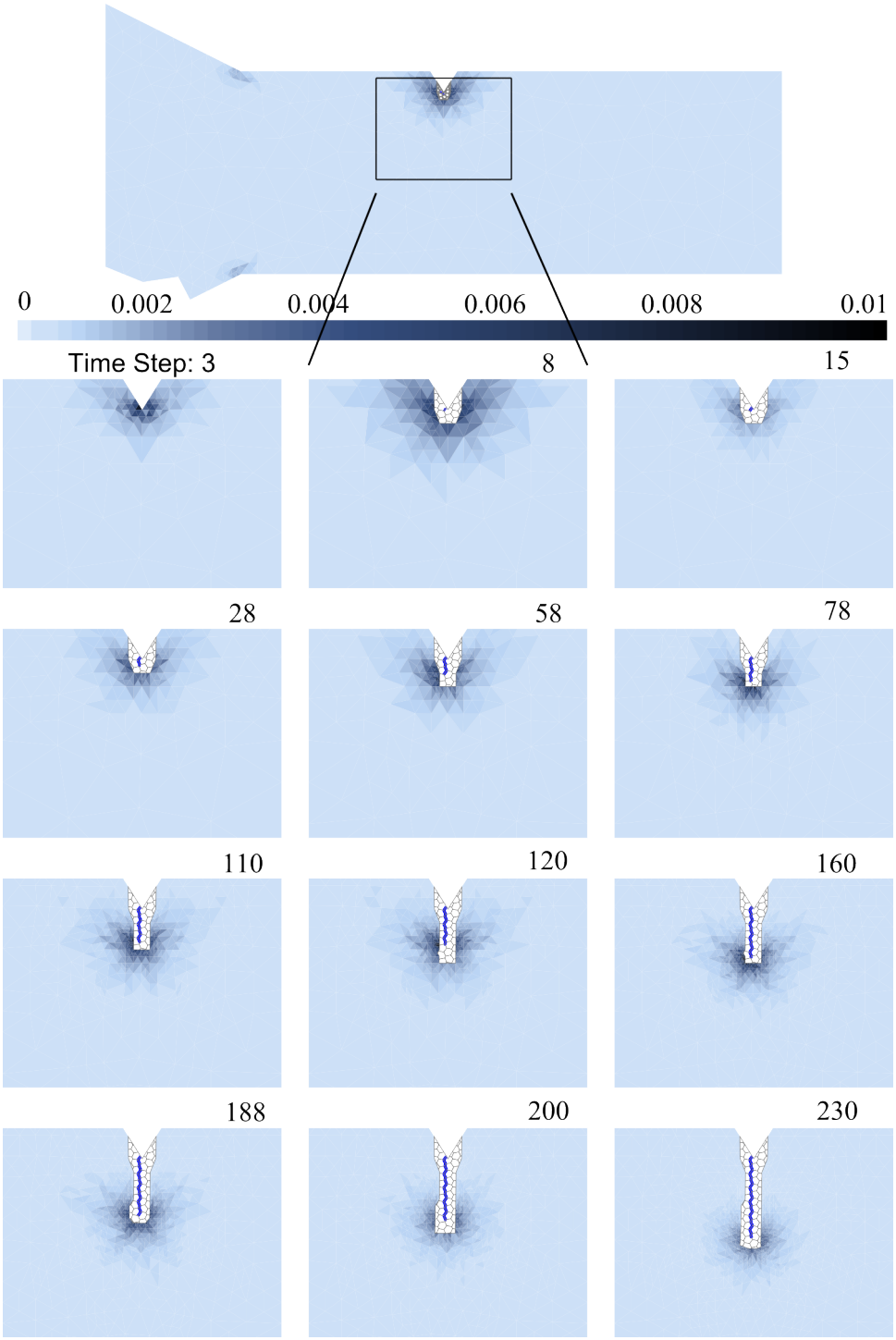

Figure 5.9: The distribution of strain-gradient sensitivity $L_{\mathcal{V}}||\nabla\nabla\mathbf{u}^c||_e$ at the coarse scale, and the adaptive development of the fully resolved region.

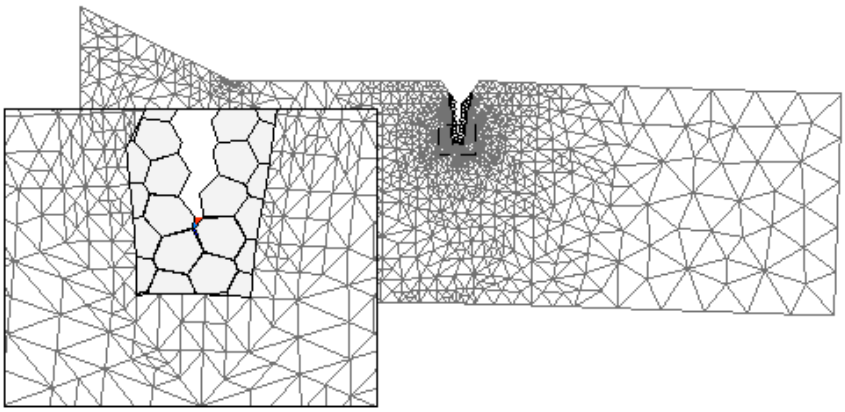

Figure 5.10: Coarse mesh in the adaptive multiscale at Time step 200. Deformation is magnified by 100.

For the notched beam, the variation of the external work W_{ext}, total strain energy W_{int}, and the dissipated energy D versus the time steps are shown in Fig. 5.11. The beam reaches its maximum strain energy at time step 8. In the next time steps, the arc-length method decreases the external load in order to track the snap-back behaviour of the load-displacement curve, and therefore, the level of the external work and the strain energy of the beam drop dramatically (Time step 15). In this stage, the grains around the notch are separated, and a macro-crack is nucleated. Although the strain energy and the external work show oscillation, the dissipated energy of the beam is monotonically increasing. This is because the local arc-length enforces the cohesive cracks to dissipate energy at each time step according to the constraint equation (4.1). Therefore, even if the external load decreases at least one of the cohesive cracks dissipates energy. The external work W_{ext}, the total strain energy W_{int} and the dissipated energy D of

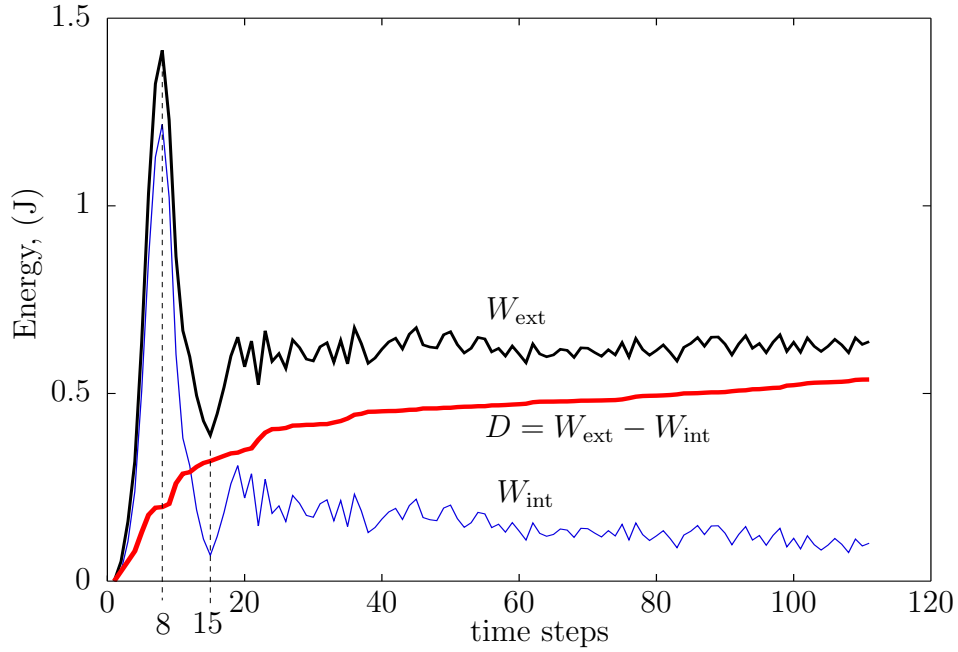

Figure 5.11: Variation of the external work W_{ext}, the strain energy W_{int}, and the dissipated energy D in a notched beam under a uniaxial load.

the beam at time τ are obtained by the following equations:

$$W_{\text{ext}}(\tau) = \int_{t=0}^{\tau} \int_{\partial\Omega_N} \mathbf{F} \cdot \Delta\mathbf{u}^{\mathbf{c}}(t) \, \mathrm{d}\Gamma \, \mathrm{d}t, \tag{5.3}$$

$$W_{\text{int}}(\tau) = 0.5 \int_{\partial\Omega_N} \mathbf{F} \cdot \mathbf{u}^{\mathbf{c}}(\tau) \, \mathrm{d}\Gamma, \tag{5.4}$$

$$D(\tau) = W_{\text{ext}} - W_{\text{int}}, \tag{5.5}$$

where t is the time, $\Delta\mathbf{u}^{\mathbf{c}}$ is the variation of the macroscopic displacement in each time step, and $\mathbf{F}$ is the external traction load on the Neumann boundary, $\partial\Omega_N$.

In Fig. 5.12, the deformation of the fully resolved region at two time steps is shown: 1) time step 8 when the domain is experiencing its maximum level of strain energy, and 2) time step 15 when the crack is initiated and the strain energy of the domain drops. Due to the micro-crack nucleation at time step 15, the beam is unloaded and therefore the V-shape notch is less deformed in comparison with

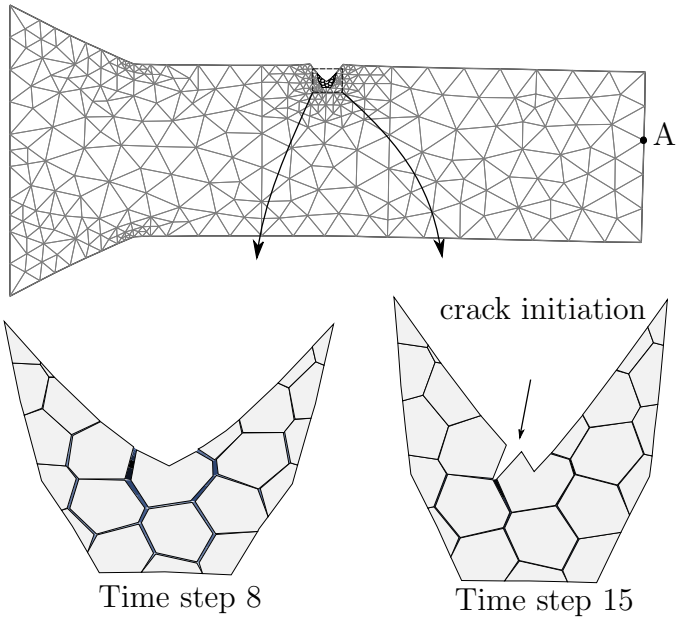

Figure 5.12: Capturing the crack initiation at the grain scale using adaptive multiscale method. Deformation is magnified by 100.

the deformation at time step 8. As shown in the Figure 5.11, the total energy at time step 15 is less than the total energy at time step 8.

The energy dissipation in the beam versus the displacement at the tip of the beam is shown in Fig. 5.13. In this figure, the result from the adaptive multiscale method is compared with DNS results. It is observed that the total dissipated energy D obtained from the adaptive multiscale method is less than the dissipated energy from the DNS for the same displacement. This is attributed to the small RVE size. As shown in the Fig. 5.4, the 16-grain RVE dissipates approximately 12% less energy than 256-grain RVE. As expected, any variation of displacement causes an increase in the total dissipated energy.

In Fig. 5.14, the dissipated energy in terms of crack length is shown for the adaptive multiscale method and the DNS. In calculating the crack length, the cohesive cracks with the damage parameter d larger than 0.423 is considered as a fully opened crack. This is because the traction-separation law transitions to the softening regime when $d > 1 - (\frac{n}{n+1})^n$. In this study $n = 0.5$ (See Section 2.3.2). The initially dissipated energy before the macro-crack initiation in the

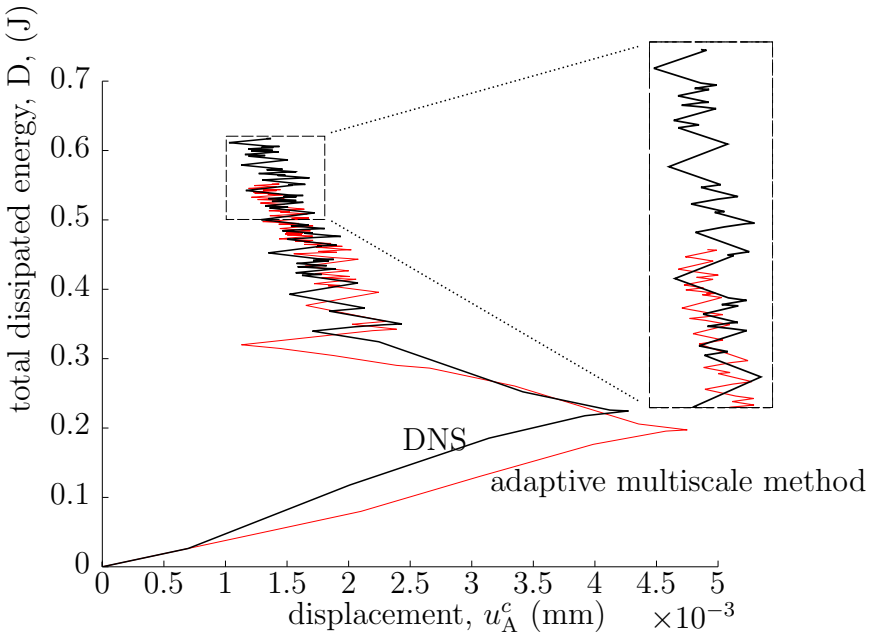

Figure 5.13: The variation of dissipated energy D versus displacement at the Neumann boundary of notched beam (Point A in Fig. 5.12).

DNS is 10% more than that in the adaptive multiscale method. This is due to the fact that the larger fully resolved region of the DNS allows the damage to diffuse into a wider area, and consequently, dissipates more energy before the crack initiation. In contrast, the adaptive multiscale model dissipates less energy before the macro-crack initiation, because of 1) the small fully resolved region stops the cohesive cracks on the coarse-fine mesh interface Γ^{fc} to dissipate energy before initiation of the first crack, and 2) the coarse elements dissipate less energy due to the small size of the RVE employed for homogenisation. In addition, the rate of energy dissipation in the DNS is higher than that in the adaptive multiscale method.

The load-displacement curve obtained from the adaptive multiscale method is compared with DNS result in Fig. 5.15. It is observed that the adaptive multiscale method shows the higher value for the yield strength and stiffness in compare to the DNS. It can be seen that the local arc-length method is able to follow a high oscillatory behaviour of load-displacement curve.

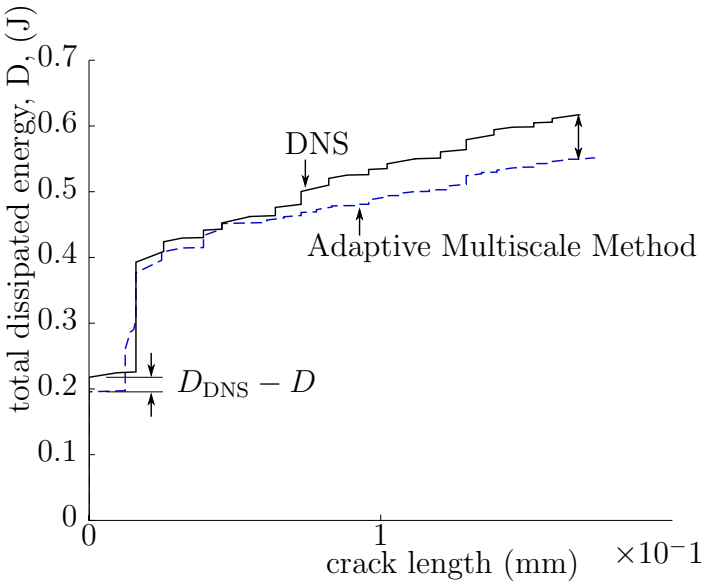

Figure 5.14: The variation of dissipated energy D versus crack length.

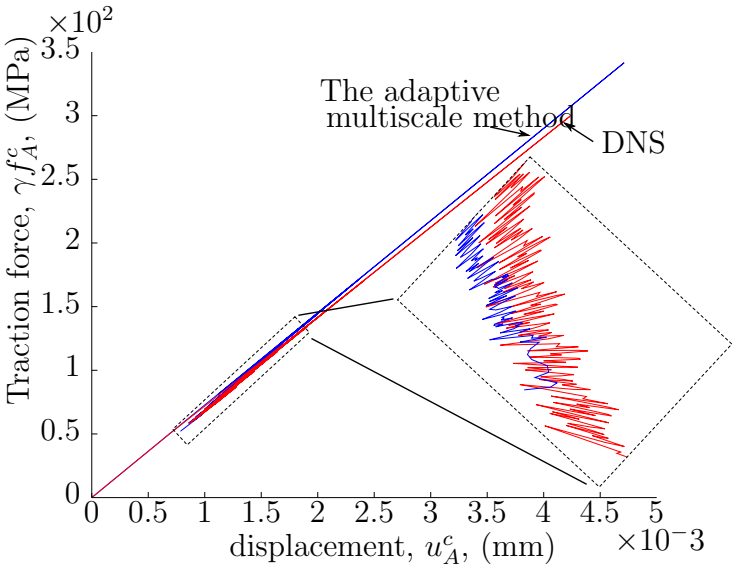

Figure 5.15: The load-displacement curve for the single notched beam.

Chapter 6

Conclusions and outlook

For modelling failure in polycrystalline materials, an hybrid-adaptive multiscale framework was designed. At the microscale, a polycrystalline structure with randomly distributed grains were considered. A thermodynamically consistent cohesive crack model was adapted to model the interface between the grains, and the grains were modelled as a orthotropic material.

The classical homogenisation technique (FE^2) is employed to obtain the macroscopic response of the heterogeneous microstructure at each load step. FE^2 is used in the safe regions of the heterogeneous structure, where representative volume elements are far from losing ellipticity, and the homogenisation error is low. In the region where localisation appears, a domain decomposition scheme is adopted to solve the problem exactly at the scale of the material heterogeneities. Lagrange multipliers are used to glue the coarse mesh strongly to the fine mesh at the interface of the scales. The homogenisation and the domain decomposition techniques have been explained in detail in Chapter 3. The main feature of the proposed framework is that the method is able to control both discretisation and modelling (homogenisation) errors in a failure problem. Due to the non-linear behaviour of the microstructure a nonlinear finite element solver based on the Newton-Raphson technique is employed at both scales. The Zienkiewicz-Zhu error estimator was used to control the discretisation error at the coarse scale. Accordingly, the coarse elements are adaptively refined, and the corresponding underlying RVEs are copied from the parent elements to the newly born elements after every mesh refinement. The homogenisation error measurement, devised

by [Temizer and Wriggers, 2011], was implemented to control the modelling error. When the homogenisation error exceeds a critical value, the corresponding coarse element is replaced by underlying microstructure. This fully resolved region is extended adaptively in order to control the modelling and discretisation errors. These errors increase by propagation of the cracks. In order to extend the fully resolved region into the coarse scale several pre-processing tasks were designed, i.e. zoom-in, equalisation and relaxation which were explained in Chapter 4. To follow the highly non-linear load-displacement curve, a local arc-length technique has been devised for the adaptive multiscale framework. In the arc-length technique, maximum variation of the microscopic crack opening in each time step is limited to a certain value by controlling the external macroscopic load. In the results chapter, a numerical investigation was carried out to determine the minimum size of RVE for the polycrystalline microstructure. Then, a two dimensional notched bar was considered as a case study to show the robustness of the proposed adaptive multiscale technique. The results from the proposed method were compared with the results from direct numerical solution.

6.1 New developments

The following contributions were made to the existing computational multiscale techniques for the modelling of fracture in polycrystalline materials:

- A thermodynamically consistent cohesive law was proposed to model intergranular fracture.
- A robust local arc-length technique was designed for concurrent multiscale methods that can follow sharp snap-back in the load-displacement curve by controlling the opening of cracks at the microscale.
- The proposed multiscale method for modelling fracture was equipped with 1) an adaptive unstructured coarse mesh, and 2) a progressive fully resolved region that makes it possible to model crack propagation.
- A procedure was devised that allows to adaptively expand the fully resolved region, which contains nonlinear cohesive cracks, into the coarse scale mesh.

- Discretisation and homogenisation model error estimators were employed to control both the adaptivity of the coarse mesh and the extension of the fully resolved region. The discretisation error at the coarse scale was controlled by the Zienkiewicz-Zhu procedure, and strain-gradient sensitivity was used to measure the homogenisation error. To obtain the second displacement gradient when using triangular linear elements, an averaging technique was proposed to obtain a smoothed field for the first displacement gradient. Then the second displacement gradient with C_0 continuity was obtained from the smoothed field of the first displacement gradient.

- The multiscale method was shown, numerically to produce results which are almost identical to direct numerical simulations.

6.2 Conclusions

The following conclusions can be drown from an examination of the RVE size for polycrystalline materials:

- Smaller RVE shows stiffer behaviour in comparison to the larger RVE. This is due to the boundary effect of the RVE. The effect of the boundary condition of the RVE reduces when the RVE size increases.

- The failure surface of the RVEs is not affected severely by the variation of the RVE size. In Chapter 5, to obtain the minimum size of the RVE for the polycrystalline microstructure, in addition to the load-displacement curve, the failure surface of the RVE was also studied. It was observed that the failure surface is not significantly sensitive to the RVE size.

- The dissipated energy per unit surface (unit volume for three dimensional problems) increases by increasing the size of the RVE. Again, this is due to the boundary condition of the RVE. The uniform displacement boundary condition of the RVE prevents the dissipation of energy in the cohesive interfaces near the boundaries.

The fracture of a notched beam under a uniaxial load was modelled by the proposed adaptive multiscale method. According to the results, one can conclude that:

- The strain-gradient sensitivity criterion is able to predict the direction of the crack propagation by defining the critical region for scale adaptation.
- The size of the critical region flagged by the strain-gradient sensitivity is smaller than the size of the critical region flagged by the scale ratio criterion. In other words, it was shown that the FE^2 method can be used for coarse elements that are even smaller than the RVE size if the strain-gradient sensitivity does not exceed its critical value.
- The adaptive multiscale method shows less energy dissipation in comparison to the DNS. This is due to the strong connection between the coarse mesh and the fine mesh which prevents the micro cracks near the common interface from dissipating energy. Another reason can be the small size of RVE that was employed for homogenisation.

6.3 Future perspective

The future works extending progress already made in the thesis can be classified into two themes: 1) improving the proposed method, and 2) implementation. The following suggestions can be made to improve the proposed adaptive multiscale method:

- A coarsening procedure should be developed in order to coarsen the fully resolved region in those parts where the macro-crack has passed and high resolution is no longer required. Coarsening linear elastic materials is straight forward by considering an RVE of the linear microstructure. Unlike linear materials, the coarsening of an inelastic microstructure requires the construction of an RVE that has equal capacity of energy storage in comparison with the corresponding fully resolved region which is going to be coarsened.

- In this work, the coarse mesh was adaptively refined to control the energy norm of the error in the displacement field. The main aim in a goal-oriented error estimator is to relate the residual, the source of the error, to the quantity of interest [Oden and Prudhomme, 2001]. Goal-oriented error estimators can be employed in order to control the error not only in the energy norm of the coarse scale but also in other quantity of interests.

- study the numerical errors at the fine scale. For example the discretisation error of the fine scale also can be studied. Error in the finite element discretisation of the RVE or the error in microscopic constitutive model affect the accuracy of the homogenisation in the FE^2 method. In other words, the discretisation and modelling errors at the microscale give rise to the modelling error at the macroscale.

- polycrystalline microstructure models can be improved by introducing contact mechanics equations. In this work, a large value for the stiffness of cohesive interfaces was considered for compressive loads in order to minimise the penetration of grains into each other. In reality, grains do not penetrate, and therefore, adopting a contact model for the interfaces avoids penetration of grains and reduces modelling error at the micro scale, consequently providing a more accurate constitutive model for the macroscale.

- The influence of the fine element size on the propagation of micro-cracks needs to be investigated for the proposed cohesive interface law.

The proposed multiscale method was designed to study fracture in polycrystalline materials. The influence of microscopic material properties, e.g. grain size, grain shape and distribution, cohesive law parameters, on the macroscopic crack propagation can be studied. However, this method can also be deployed to model fracture in other microstructures, such as fibre reinforced composites. The proposed multiscale method lends itself to modelling fracture in functionally graded materials. The crack propagation and the spatial variation of the microscopic material properties can be captured by the fully resolved region. The method also can be extended to study thermal stress fracture, fatigue and impact phenomena.

Appendix A

In this appendix, the averaging theorem for strain, stress and energy fields in a heterogeneous domain with discontinuities is given. For simplicity, a domain $\mathcal{V}$ and its boundary $\partial\mathcal{V}$ composed of two parts $\mathcal{V}_L$ and $\mathcal{V}_R$ is considered. The interface between the different phases is shown by Γ, (see Figure 1). The traction vector $\mathbf{t}^{(L)}$ acts on $\mathcal{V}_L$, while $\mathbf{t}^{(R)}$ acts on $\mathcal{V}_R$ equals to $\mathbf{t}^{(L)}$ but opposite.

The average strain theorem

The non-weighted volume average of the strain over $\mathcal{V}$ is given by:

$$\begin{aligned}\langle \boldsymbol{\varepsilon}^f \rangle &= \frac{1}{|\mathcal{V}|}\int_{\mathcal{V}} \frac{1}{2}\left(\nabla\otimes\mathbf{u} + (\nabla\otimes\mathbf{u})^T\right)\,\mathrm{d}V \\ &= \frac{1}{2|\mathcal{V}|}\left(\int_{\mathcal{V}_L} \nabla\otimes\mathbf{u} + (\nabla\otimes\mathbf{u})^T\,\mathrm{d}V + \int_{\mathcal{V}_R} \nabla\otimes\mathbf{u} + (\nabla\otimes\mathbf{u})^T\,\mathrm{d}V\right) \\ &= \frac{1}{2|\mathcal{V}|}\left(\int_{\partial\mathcal{V}_L} \mathbf{u}\otimes\mathbf{n} + (\mathbf{u}\otimes\mathbf{n})^T\,\mathrm{d}\Gamma + \int_{\partial\mathcal{V}_R} \mathbf{u}\otimes\mathbf{n} + (\mathbf{u}\otimes\mathbf{n})^T\,\mathrm{d}\Gamma\right), \end{aligned} \tag{1}$$

where $\mathbf{n}$ is the outward unit vector normal to the boundaries. Note that the third line in Eq. 1 is not an outcome of the divergence theorem, but of a generalization [Zohdi and Wriggers, 2008] that can be found in [Chandrasekharaiah and Debnath, 1994]. Splitting the surface integrals into boundary integrals and interface

integrals gives:

$$\begin{aligned}
\langle \boldsymbol{\varepsilon}^f \rangle &= \frac{1}{2|\mathcal{V}|}\left(\int_{\partial \mathcal{V}_L \setminus \Gamma^{(L)}} \mathbf{u}\otimes\mathbf{n} + (\mathbf{u}\otimes\mathbf{n})^T \,\mathrm{d}\Gamma + \int_{\partial \mathcal{V}_R \setminus \Gamma^{(R)}} \mathbf{u}\otimes\mathbf{n} + (\mathbf{u}\otimes\mathbf{n})^T \,\mathrm{d}\Gamma\right) \\
&+ \frac{1}{2|\mathcal{V}|}\left(\int_{\Gamma^{(L)}} \mathbf{u}\otimes\mathbf{n} + (\mathbf{u}\otimes\mathbf{n})^T \,\mathrm{d}\Gamma + \int_{\Gamma^{(R)}} \mathbf{u}\otimes\mathbf{n} + (\mathbf{u}\otimes\mathbf{n})^T \,\mathrm{d}\Gamma\right) \\
&= \frac{1}{2|\mathcal{V}|}\left(\int_{\partial \mathcal{V}} \mathbf{u}\otimes\mathbf{n} + (\mathbf{u}\otimes\mathbf{n})^T \,\mathrm{d}\Gamma\right) \\
&+ \frac{1}{2|\mathcal{V}|}\int_{\Gamma} \mathbf{u}^{(L)}\otimes\mathbf{n}_\Gamma^{(L)} + (\mathbf{u}^{(L)}\otimes\mathbf{n}_\Gamma^{(L)})^T + \mathbf{u}^{(R)}\otimes\mathbf{n}_\Gamma^{(R)} + (\mathbf{u}^{(R)}\otimes\mathbf{n}_\Gamma^{(R)})^T \,\mathrm{d}\Gamma \\
&= \frac{1}{2|\mathcal{V}|}\left(\int_{\partial \mathcal{V}} \mathbf{u}\otimes\mathbf{n} + (\mathbf{u}\otimes\mathbf{n})^T \,\mathrm{d}\Gamma\right) \\
&- \frac{1}{|\mathcal{V}|}\int_{\Gamma} \frac{1}{2}\left(\llbracket\mathbf{u}\rrbracket\otimes\mathbf{n}_\Gamma + (\llbracket\mathbf{u}\rrbracket\otimes\mathbf{n}_\Gamma)^T\right) \mathrm{d}\Gamma. \qquad (2)
\end{aligned}$$

where $\llbracket\mathbf{u}\rrbracket = \mathbf{u}^{(R)} - \mathbf{u}^{(L)}$ is the displacement jump (see Figure 1), and $\mathbf{n}_\Gamma = \mathbf{n}_\Gamma^{(L)} = -\mathbf{n}_\Gamma^{(R)}$ is the normal unit vector at the interface. Note that these variables have been defined in such a way that $\llbracket\mathbf{u}\rrbracket \cdot \mathbf{n}_\Gamma > 0$ for an opened crack.

If the boundary condition of the domain is defined by [1] $\mathbf{u}(\mathbf{x}) = \boldsymbol{\varepsilon}\cdot\mathbf{x} \quad \forall \mathbf{x} \in \partial\mathcal{V}$ then we have:

$$\langle \boldsymbol{\varepsilon}^f \rangle = \boldsymbol{\varepsilon} - \frac{1}{|\mathcal{V}|}\int_{\Gamma} \frac{1}{2}\left(\llbracket\mathbf{u}\rrbracket\otimes\mathbf{n}_\Gamma + (\llbracket\mathbf{u}\rrbracket\otimes\mathbf{n}_\Gamma)^T\right) \mathrm{d}\Gamma. \qquad (3)$$

where $\boldsymbol{\varepsilon}$ is the macroscopic strain tensor that is a constant over the microscopic domain, $\mathcal{V}$.

The average stress theorem

The non-weighted volume average of the stress over $\mathcal{V}$ is defined by:

$$\langle \boldsymbol{\sigma}^f \rangle = \frac{1}{|\mathcal{V}|}\int_{\mathcal{V}} \boldsymbol{\sigma}^f \,\mathrm{d}V \qquad (4)$$

[1] In the Cartesian coordinate, $\mathbf{u}(\mathbf{x}) = \boldsymbol{\varepsilon}\cdot\mathbf{x}$ can be written by Einsteiń notation: $u_i = \varepsilon_{ij}x_j$

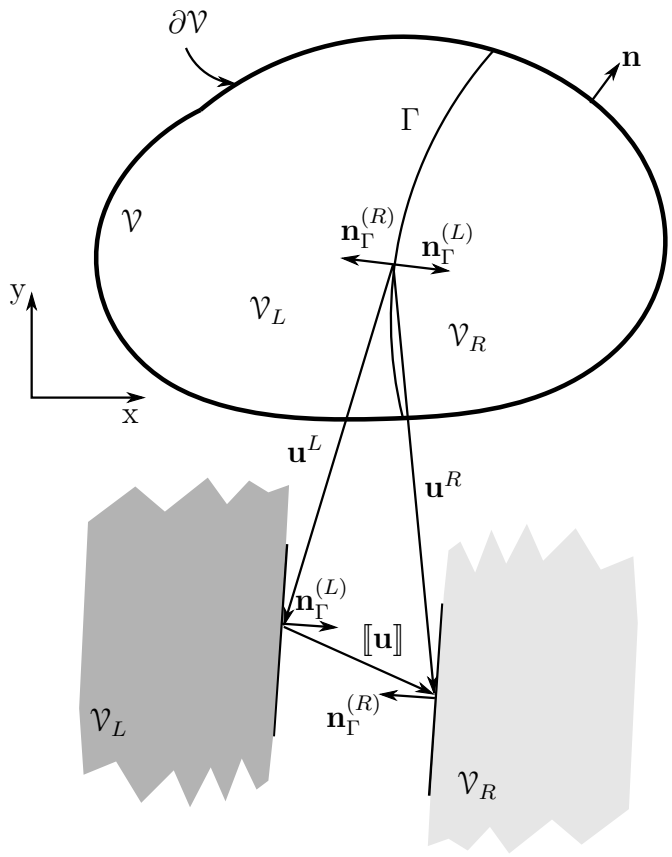

Figure 1: Heterogeneous domain

Again, splitting the domain of integral into two subdomains:

$$\begin{aligned}\langle \boldsymbol{\sigma}^f \rangle &= \frac{1}{|\mathcal{V}|}\left(\int_{\mathcal{V}_L} \boldsymbol{\sigma}^f \, \mathrm{d}V + \int_{\mathcal{V}_R} \boldsymbol{\sigma}^f \, \mathrm{d}V\right) \\ &= \frac{1}{|\mathcal{V}|}\left(\int_{\mathcal{V}_L} \boldsymbol{\sigma}^f \cdot (\boldsymbol{\nabla} \otimes \mathbf{x}) \, \mathrm{d}V + \int_{\mathcal{V}_R} \boldsymbol{\sigma}^f \cdot (\boldsymbol{\nabla} \otimes \mathbf{x}) \, \mathrm{d}V\right).\end{aligned}$$

Since the gradient of position vector equals to the second order identity tensor, $\boldsymbol{\nabla} \otimes \mathbf{x} = \mathbf{I}$, then it is allowed to replace $\boldsymbol{\sigma}^f$ by $\boldsymbol{\sigma}^f \cdot (\boldsymbol{\nabla} \otimes \mathbf{x})$. By using the chain rule we have

$$\begin{aligned}\boldsymbol{\sigma}^f \otimes (\boldsymbol{\nabla} \cdot \mathbf{x}) &= \boldsymbol{\nabla}\cdot(\boldsymbol{\sigma}^f \otimes \mathbf{x}) - (\boldsymbol{\nabla}\cdot\boldsymbol{\sigma}^f) \otimes \mathbf{x} \\ &= \boldsymbol{\nabla}\cdot(\boldsymbol{\sigma}^f \otimes \mathbf{x}) + \mathbf{f} \otimes \mathbf{x},\end{aligned}$$

where $\mathbf{f}$ is the body force. However, in the equilibrium equations of the RVE, the body forces can be neglected[1] $\mathbf{f} = \mathbf{0}$. Therefore,

$$\begin{aligned}\langle \boldsymbol{\sigma}^f \rangle &= \frac{1}{|\mathcal{V}|}\left(\int_{\mathcal{V}_L} \boldsymbol{\nabla}\cdot(\boldsymbol{\sigma}^f \otimes \mathbf{x}) \, \mathrm{d}V + \int_{\mathcal{V}_R} \boldsymbol{\nabla}\cdot(\boldsymbol{\sigma}^f \otimes \mathbf{x}) \, \mathrm{d}V\right) \\ &= \frac{1}{|\mathcal{V}|}\left(\int_{\partial\mathcal{V}_L} (\boldsymbol{\sigma}^f \cdot \mathbf{n}) \otimes \mathbf{x} \, \mathrm{d}\Gamma + \int_{\partial\mathcal{V}_R} (\boldsymbol{\sigma}^f \cdot \mathbf{n}) \otimes \mathbf{x} \, \mathrm{d}\Gamma\right) \\ &= \frac{1}{|\mathcal{V}|}\left(\int_{\partial\mathcal{V}} \mathbf{t}^f \otimes \mathbf{x} \, \mathrm{d}\Gamma + \int_{\Gamma^{(L)}} \mathbf{t}^f \otimes \mathbf{x} \, \mathrm{d}\Gamma + \int_{\Gamma^{(R)}} \mathbf{t}^f \otimes \mathbf{x} \, \mathrm{d}\Gamma\right)\end{aligned}$$

where $\mathbf{t}^f = \boldsymbol{\sigma}^f \cdot \mathbf{n}$ is the traction. Again, generalisation theorem is used to obtain the second line of the equation above. At the common interface between the two phases, the traction of the left phase is equal and opposite to the traction of the

[1] This is due to the fact that considering the body forces means to take into account the density variation of the heterogeneous microstructure and its influence on the homogenization result. Since the stress from the body force is much smaller than the stress from the boundary conditions of the RVE, then it is allowed to neglect the body forces at the microsacle even if we have the body forces at the macroscale problem.

right phase $\mathbf{t}_L^f = -\mathbf{t}_R^f$. Therefore, we can write

$$\langle \boldsymbol{\sigma}^f \rangle = \frac{1}{|\mathcal{V}|} \int_{\partial \mathcal{V}} \mathbf{t}^f \otimes \mathbf{x} \, \mathrm{d}\Gamma \tag{5}$$

This result is obtained for a heterogeneous domain with crack. Note that unlike the average strain theorem, the average stress theorem is the same for domains without cracks and domains with cracks. If it is assumed that the macroscopic stress $\boldsymbol{\sigma}$ is constant over the boundary of the RVE, then $\mathbf{t}^f = \boldsymbol{\sigma} \cdot \mathbf{n}$. In conclusion, we have

$$\begin{aligned} \langle \boldsymbol{\sigma}^f \rangle &= \frac{1}{|\mathcal{V}|} \, \boldsymbol{\sigma} \cdot \int_{\partial \mathcal{V}} \mathbf{n} \otimes \mathbf{x} \, \mathrm{d}\Gamma \\ &= \frac{1}{|\mathcal{V}|} \, \boldsymbol{\sigma} \cdot |\mathcal{V}| \mathbf{I} \\ &= \boldsymbol{\sigma}, \end{aligned}$$

where $\int_{\partial \mathcal{V}} \mathbf{x} \otimes \mathbf{n} \, \mathrm{d}\Gamma = \int_{\mathcal{V}} \boldsymbol{\nabla} \otimes \mathbf{x} \, \mathrm{d}V = \int_{\mathcal{V}} \mathbf{I} \, \mathrm{d}V = |\mathcal{V}| \mathbf{I}$, and $\mathbf{I}$ is the identity matrix.

The average energy theorem: Hill-Mandel Conditions

The Hill-Mandel condition represents the energy consistency of the micro-macro scale transition. the volume average rate of stress work over an RVE equals the rate of work of the average stress over the RVE Hill [1963]. That is to say, the average rate of strain energy density at the microscale is equal to the rate of macroscopic strain energy density: For a domain without crack this condition is given by

$$\langle \boldsymbol{\sigma}^f : \dot{\boldsymbol{\varepsilon}}^f \rangle = \boldsymbol{\sigma} : \dot{\boldsymbol{\varepsilon}}, \tag{6}$$

where $\dot{\boldsymbol{\varepsilon}} = \frac{\mathrm{d}\boldsymbol{\varepsilon}}{\mathrm{d}t}$ is the rate of the change of the strain. This equality ensures that the homogenized stiffness tensor defined through the average of stress work equals to the same defined through the relations of the average of stress-strain. For a

domain with micro-cracks, some energy may be stored in the cohesive interface of the cracks that must be taken into account to satisfy the Hill-Mandel condition. In fact, the rate of change of the macroscopic energy density equals to the average of the rate of change in the both microscopic strain energy density plus micro-cracks cohesive energy density:

$$\langle \boldsymbol{\sigma}^f : \dot{\boldsymbol{\varepsilon}}^f + \mathbf{t}^f_\Gamma \cdot [\![\dot{\mathbf{u}}]\!] \rangle = \boldsymbol{\sigma} : \dot{\boldsymbol{\varepsilon}}, \tag{7}$$

where $\mathbf{t}^f_\Gamma \cdot [\![\dot{\mathbf{u}}]\!]$ is the surface density of cohesive power at the crack interfaces. Note that there are two traction at the interface, one from left sub-domain, $\mathbf{t}^f_L$, and one from the right sub-domain, $\mathbf{t}^f_R$. Since the cohesive energy density must be non-negative, and due to the definition of displacement jump which is $[\![\mathbf{u}]\!] = \mathbf{u}_R - \mathbf{u}_L$, therefore the traction vector of the interface, used in Eq. 7, must be equal to the traction vector of the left sub-domain, $\mathbf{t}^f_\Gamma = \mathbf{t}^f_L = -\mathbf{t}^f_R$.

In the following, it is shown that in a heterogeneous domain with cohesive interfaces, the average of power over a domain equals to the average of the rate of work done on the domain boundaries:

$$\begin{aligned}
\langle \boldsymbol{\sigma}^f : \dot{\boldsymbol{\varepsilon}}^f + \mathbf{t}^f \cdot [\![\dot{\mathbf{u}}]\!] \rangle &= \frac{1}{|\mathcal{V}|} \int_{\mathcal{V}} \boldsymbol{\sigma}^f : \dot{\boldsymbol{\varepsilon}}^f \mathrm{d}V + \frac{1}{|\mathcal{V}|} \int_\Gamma \mathbf{t}^f \cdot [\![\dot{\mathbf{u}}]\!] \mathrm{d}\Gamma \\
&= \frac{1}{|\mathcal{V}|} \int_{\mathcal{V}} \boldsymbol{\sigma}^f : \frac{1}{2} \left(\boldsymbol{\nabla} \otimes \dot{\mathbf{u}} + (\boldsymbol{\nabla} \otimes \dot{\mathbf{u}})^T \right) \mathrm{d}V + \frac{1}{|\mathcal{V}|} \int_\Gamma \mathbf{t}^f \cdot [\![\dot{\mathbf{u}}]\!] \mathrm{d}\Gamma \\
&= \frac{1}{|\mathcal{V}|} \int_{\mathcal{V}} \boldsymbol{\sigma}^f : \boldsymbol{\nabla} \otimes \dot{\mathbf{u}} \, \mathrm{d}V + \frac{1}{|\mathcal{V}|} \int_\Gamma \mathbf{t}^f \cdot [\![\dot{\mathbf{u}}]\!] \mathrm{d}\Gamma.
\end{aligned} \tag{8}$$

The symmetry of the Cauchy stress tensor which comes form the balance of angular momentum law is used to obtain the third equation. After splitting the volume integral into two integrals over sub-domains, $\mathcal{V}_L$ and $\mathcal{V}_R$, the Gauss

theorem is used to convert the volume integral into a surface integral:

$$\begin{aligned}
\int_{\mathcal{V}} \boldsymbol{\sigma}^f : \boldsymbol{\nabla} \otimes \dot{\mathbf{u}} \, \mathrm{d}V &= \int_{\mathcal{V}_L} \boldsymbol{\sigma}^f : \boldsymbol{\nabla} \otimes \dot{\mathbf{u}} \, \mathrm{d}V + \int_{\mathcal{V}_R} \boldsymbol{\sigma}^f : \boldsymbol{\nabla} \otimes \dot{\mathbf{u}} \, \mathrm{d}V \\
&= \int_{\mathcal{V}_L} \boldsymbol{\nabla} \cdot (\boldsymbol{\sigma}^f \cdot \dot{\mathbf{u}}) - (\boldsymbol{\nabla} \cdot \boldsymbol{\sigma}^f) \cdot \dot{\mathbf{u}} \, \mathrm{d}V \\
&+ \int_{\mathcal{V}_R} \boldsymbol{\nabla} \cdot (\boldsymbol{\sigma}^f \cdot \dot{\mathbf{u}}) - (\boldsymbol{\nabla} \cdot \boldsymbol{\sigma}^f) \cdot \dot{\mathbf{u}} \, \mathrm{d}V \\
&= \int_{\partial\mathcal{V}_L} \mathbf{n} \cdot (\boldsymbol{\sigma}^f \cdot \dot{\mathbf{u}}) \, \mathrm{d}\Gamma + \int_{\partial\mathcal{V}_R} \mathbf{n} \cdot (\boldsymbol{\sigma}^f \cdot \dot{\mathbf{u}}) \, \mathrm{d}\Gamma \\
&= \int_{\partial\mathcal{V}_L} \mathbf{t}^f \cdot \dot{\mathbf{u}} \, \mathrm{d}\Gamma + \int_{\partial\mathcal{V}_R} \mathbf{t}^f \cdot \dot{\mathbf{u}} \, \mathrm{d}\Gamma \\
&= \int_{\partial\mathcal{V}} \mathbf{t}^f \cdot \dot{\mathbf{u}} \, \mathrm{d}\Gamma + \int_{\Gamma_L} \mathbf{t}^f \cdot \dot{\mathbf{u}} \, \mathrm{d}\Gamma + \int_{\Gamma_R} \mathbf{t}^f \cdot \dot{\mathbf{u}} \, \mathrm{d}\Gamma \\
&= \int_{\partial\mathcal{V}} \mathbf{t}^f \cdot \dot{\mathbf{u}} \, \mathrm{d}\Gamma - \int_{\Gamma} \mathbf{t}^f_{\Gamma} \cdot [\![\dot{\mathbf{u}}]\!] \, \mathrm{d}\Gamma, \qquad (9)
\end{aligned}$$

where $[\![\mathbf{u}]\!] = \mathbf{u}^{(R)} - \mathbf{u}^{(L)}$ is the displacement jump (see Fig. 1), and $\mathbf{t}^f_{\Gamma} = \mathbf{t}^f_L = -\mathbf{t}^f_R$ is the traction vector at the interface. Substitute Eq. 9 into Eq. 8 gives,

$$\langle \boldsymbol{\sigma}^f : \dot{\boldsymbol{\varepsilon}}^f + \mathbf{t}^f \cdot [\![\dot{\mathbf{u}}]\!] \rangle = \frac{1}{|\mathcal{V}|} \int_{\partial\mathcal{V}} \mathbf{t}^f \cdot \dot{\mathbf{u}} \, \mathrm{d}\Gamma. \qquad (10)$$

From Eq. 10, it can be inferred that the volume average rate of stress work is equal to the average rate of the traction work on the boundary of the RVE. This result is obtained for domains with micro-cracks which it is also true for domains without cracks. Therefore, based on the Hill-Mandel condition, the rate of change in the macroscopic stress work is equal to the average rate of the traction work on the RVE boundaries. Note that any assumptions that is made for the boundary conditions of RVE, must be consistent with the Hill-Mandel condition.

References

Abdollahi, A. and Arias, I. [2014], 'Three-dimensional simulation of crack propagation in ferroelectric polycrystals : Effect of combined toughening mechanisms', *ACTA MATERIALIA* **65**, 106–117.
URL: *http://dx.doi.org/10.1016/j.actamat.2013.11.016* 19

Abdulle, A. [2009], 'The finite element heterogeneous multiscale method : a computational strategy for multiscale PDEs', *GAKUTO International Series Math. Sci. Appl.* **31**, 133–181. 3

Abel JF, S. M. [1979], 'An algorithm for multipoint constraints in finite element analysis', *International Journal for Numerical Methods in Engineering* **14**(3), 464–467. 51

Ainsworth, M. and Oden, J. T. [1997], 'A posteriori error estimation in finite element analysis', *Computer Methods in Applied Mechanics and Engineering* **142**(1-2), 1–88. 64

Alfaro, M. V. C., Suiker, a. S. J., Verhoosel, C. V. and Borst, R. [2009], 'Computational homogenization of discrete fracture in fibre-epoxy systems', *International Journal of Material Forming* **2**(S1), 931–934. vii, 3, 4, 5

Allix, O. and Corigliano, A. [1996], 'Modeling and simulation of crack propagation in mixed-modes interlaminar fracture specimens', *International Journal of Fracture* **77**(2), 111–140. 17, 27

Allix, O., Kerfriden, P., Gosselet, P., Cachan, L.-c. E. N. S., Upmc, C. and Universud, P. [2010], 'On the control of the load increments for a proper description of

multiple delamination in a domain decomposition framework .', *International Journal for Numerical Methods in Engineering* **11**, 1518–1540. 60

Amini, A. M., Dureisseix, D. and Cartraud, P. [2009], 'Multi-scale domain decomposition method for large-scale structural analysis with a zooming technique : Application to plate assembly', *International Journal For Numercal Methods In Engineering* **79**(February), 417–443. 8, 56

Anil, J. P. S., Shetty, V. V. D. K. and Gordow, R. S. [1978], 'Strength-Grain Size Relations in Polycrystalline Ceramics'. 16

Bellante, J. J. and Kahn, H. [2005], 'Fracture toughness of polycrystalline silicon carbide thin films', *Applied Physics Letters* **86**, 3–5. 16

Belytschko, T., Loehnert, S. and Song, J.-h. H. [2008], 'Multiscale aggregating discontinuities : A method for circumventing loss of material stability', *International Journal for Numerical Method inEngineering* **73**(August 2007), 869–894. 5

Bernardi, C., Maday, Y. and Rapetti, F. [2005], 'Basics and some applications of the mortar element method', *GAMM-Mitt* **28**(2), 97–123. 8

Besson, J., Cailletaud, G., Chaboche, J. L. and Forest, S. [2010], *Non-Linear Mechanics of Materials*, Solid Mechanics and Its Applications, Springer. 54

Bochev, P., Christon, M., Collis, S. S., Lehoucq, R., Shadid, J., Slepoy, A. and Wagner, G. [2004], A Mathematical framework for multiscale science and engineering : the variational multiscale method and interscale transfer operators, Technical report, Sandia National Laboratories. 2

Bohm, H. J. [2008], A short introduction to basic aspects of continuum micromechanics, Technical report, Vienna University of Technology, Vienna, Austria. 37

Bordas, S. P. A. and Duflot, M. [2007], 'Derivative recovery and \emph{a posteriori} error estimate for extended finite elements', *Computer Methods in Applied Mechanics and Engineering* **196**(35-36), 3381–3399. 64

Boroomand, B. and Zienkiewicz, O. C. [1997], 'An improved {REP} recovery and the effectivity robustness test', *International Journal for Numerical Methods in Engineering* **40**(17), 3247–3277. 70

Bosco, E. [2012], Computational homogenization formulations for localization and multiphysics phenomena in energy storage materials, PhD thesis, Universita degli studi di Brescia. 4, 7

Brocks, W., Cornec, A. and Scheider, I. [2003], Fracture of Materials from Nano to Macro,, *in* 'Comprehensive Structural Integrity', Elsevier, Oxford, chapter 3, pp. 127–209. 18

Buehler, M. J. [2008], *Atomistic modeling of materials fFailure*, Springer. 23, 24

Buehler, M. J. and Gao, H. [2005], Ultra large scale simulations of dynamic materials failure, *in* 'Handbook of Theoretical and Computational Nanotechnology', Vol. X, chapter 14, pp. 1–41. 7

Carolan, D., Ivanković, a. and Murphy, N. [2013], 'A combined experimentalnumerical investigation of fracture of polycrystalline cubic boron nitride', *Engineering Fracture Mechanics* **99**, 101–117.
URL: *http://linkinghub.elsevier.com/retrieve/pii/S0013794412003621* 16

Chandrasekharaiah, D. S. and Debnath, L. [1994], *Continuum mechanics*, Academic press. 99

Coenen, E. W. C., Kouznetsova, V. G. and Geers, M. G. D. [2012], 'Multi-scale continuous-discontinuous framework for computational–homogenization-localization', *Journal of the Mechanics and Physics of Solids* **60**(8), 1486–1507. 7

Crisfield, M. A. [1982], 'Accelerated solution techniques and concrete cracking', *Computer Methods in Applied Mechanics and Engineering* **33**(1-3), 585–607. 58, 60

Crisfield, M. A. [1997], *Non-linear finite element analysis of solids and structures: advanced topics*, 1st edn, John Wiley & Sons, Inc., New York, NY, USA. 60

Dhia, H. B. E. N. [1998], 'Multiscale mechanical problems: the Arlequin method', *Comptes Rendus de l'Academie des Sciences Series IIB Mechanics Physics Astronomy* **326**(12), 899–904. 8, 49

Dimitri, R., Trullo, M., Zavarise, G. and Lorenzis, L. D. [2014], 'A consistency assessment of coupled cohesive zone models for mixed-mode debonding problems', *Computational Mechanics and Mechanics of Materials in Italy* **29**, 266–283. 19

E, W. and Engquist, B. [2003], 'The heterogeneous multiscale methods', *Communications in Mathematical Sciences* **1**(1), 87–132. 2

Eringen, A. C. [2001], *nonlocal continuum field theories*, springer. 1

Espinosa, H. D. and Zavattieri, P. D. [2003], 'A grain level model for the study of failure initiation and evolution in polycrystalline brittle materials. Part II: Numerical examples', *Mechanics of Materials* **35**(3-6), 365–394.
URL: *http://linkinghub.elsevier.com/retrieve/pii/S0167663602002879* 18

Farhat C, Lacour C, R. D. [1998], 'Incorporation of linear multipoint constraints in substructure based iterative solvers. Part 1: a numerically scalable algorithm.', *International Journal for Numerical Methods in Engineering* **43**(6), 997– 1016. 51

Farhat, C. and Roux, F. F.-x. [1991], 'A method of finite element tearing and interconnecting and its parallel solution algorithm.', *International Journal for Numerical Methods in Engineering* **32**(6), 1205–1227. 9, 36, 49

Feyel, F. and Chaboche, J.-l. [2000], 'FE 2 multiscale approach for modelling the elastoviscoplastic behaviour of long fibre SiC / Ti composite materials', *Computer Methods in Applied Mechanics and Engineering* **183**, 309–330. iv, 2, 3, 36, 38

Geers, M. G. D. [1999], 'Enhanced solution control for physically and geometrically non-linear problems. Part Iâthe subplane control approach', *International Journal for Numerical Methods in Engineering* **46**(2), 177–204. 60

Geers, M., Kouznetsova, V. G. and Brekelmans, W. A. M. [2010], 'Multi-scale computational homogenization: Trends and challenges', *Journal of Computational and Applied Mathematics* **234**(7), 2175–2182. 3, 47

Ghosh, A. and Chaudhuri, P. [2013], 'Computational modeling of fracture in concrete using a meshfree meso-macro-multiscale method', *Computational Materials Science* **69**(2013), 204–215. 10, 13

Ghosh, S., Bai, J. and Raghavan, P. [2007], 'Concurrent multi-level model for damage evolution in microstructurally debonding composites', *Mechanics of Materials* **39**(3), 241–266. vii, 8, 11, 12, 87

Ghosh, S., Lee, K. and Raghavan, P. [2001], 'A multi-level computational model for multi-scale damage analysis in composite and porous materials', *International Journal of Solids and Structures* **38**(14), 2335–2385. 8, 10, 11, 12

Gitman, I., Askes, H. and Sluys, L. [2007], 'Representative volume: Existence and size determination', *Engineering Fracture Mechanics* **74**(16), 2518–2534. 3, 44, 47, 78

Glaessgen, E. H., Saether, E., Phillips, D. R. and Yamakov, W. [2006], Multiscale modeling of grain-boundary fracture : cohesive zone models parameterized from atomistic simulations, *in* '47th AIAA/ASME/ASCE/AHS/ASC Structures, Structural dynamics, and materials conference', pp. 1–13. 18

Gravemeier, V., Lenz, S. and Wall, W. a. [2007], 'Towards a taxonomy for multiscale methods in computational mechanics: building blocks of existing methods', *Computational Mechanics* **41**(2), 279–291. 2

Guidault, P. and Belytschko, T. [2007], 'On the L 2 and the H 1 couplings for an overlapping domain decomposition method using Lagrange multipliers', *International Journal for Numerical Method in Engineering* **70**(October 2006), 322–350. 49

Hill, R. [1963], 'Elastic properties of reinforced solids: some theoretical principles', *J. Mech. Phys. Solids* **11**, 357–372. 43, 47, 103

Hirschberger, C. B. B., Ricker, S., Steinmann, P. and Sukumar, N. [2009], 'Computational multiscale modelling of heterogeneous material layers', *Engineering Fracture Mechanics* **76**(6), 793–812. 5

Hughes, T. [1995], 'Multiscale phenomena: Green's functions, the Dirichlet-to-Neumann formulation, subgrid scale models, bubbles and the origins of stabilized methods', *Computer Methods in Applied Mechanics and Engineering* **127**(1-4), 387–401. 2

Hund, A. and Ramm, E. [2007], 'Locality constraints within multiscale model for non-linear material behaviour', *International Journal for Numerical methods in Engineering* **70**(December), 1613–1632. 8, 51

Ibrahimbegovic, A. and Markovic, D. [2003], 'Strong coupling methods in multi-phase and multi-scale modeling of inelastic behavior of heterogeneous structures', *Computer Methods in Applied Mechanics and Enginnering* **192**, 3089–3107. 8, 12

Kerfriden, P., Allix, O. and Gosselet, P. [2009], 'A three-scale domain decomposition method for the 3D analysis of debonding in laminates', *Computational Mechanics* **44**(3), 343–362. 3

Kerfriden, P., Gosselet, P., Adhikari, S. and Bordas, S. P. A. [2011], 'Bridging proper orthogonal decomposition methods and augmented Newton Krylov algorithms : An adaptive model order reduction for highly nonlinear mechanical problems', *Computer Methods in Applied Mechanics and Engineering* **200**, 850–866. 58

Kerfriden, P., Goury, O., Rabczuk, T. and Bordas, S. P. [2013], 'A partitioned model order reduction approach to rationalise computational expenses in nonlinear fracture mechanics', *Computer Methods in Applied Mechanics and Engineering* **256**, 169–188. 48

Kouznetsova, V. G., Brekelmans, W. a. M. and Baaijens, F. P. T. [2001], 'An approach to micro-macro modeling of heterogeneous materials', *Computational Mechanics* **27**(1), 37–48. 2, 36

Kouznetsova, V. G., Geers, M. G. D. and Brekelmans, W. a. M. [2002], 'Multi-scale constitutive modelling of heterogeneous materials with a gradient-enhanced computational homogenization scheme', *International Journal for Numerical Methods in Engineering* **54**(8), 1235–1260. 47

Ladevèze, P. and Simmonds, J. G. [1999], *Nonlinear computational structural mechanics: new approaches and non-incremental methods of calculation*, Mechanical engineering series, Springer. 36, 49

Larsson, F. and Runesson, K. [2011], 'On two-scale adaptive FE analysis of micro-heterogeneous media with seamless scale-bridging', *Computer Methods in Applied Mechanics and Engineering* **200**(37-40), 2662–2674. 3, 10, 12, 65

Lee, S.-C., Vouvakis, M. N. and Lee, J.-F. [2005], 'A non-overlapping domain decomposition method with non-matching grids for modeling large finite antenna arrays', *Journal of Computational Physics* **203**(1), 1–21. 49

Lemaitre, J. and Chaboche, J. L. [1994], *Mechanics of Solid Materials*, Cambridge University Press. 24

Lions, P.-L. [1988], On the Schwarz alternating method. I., *in* 'In First international symposium on domain decomposition methods for partial differential equations', pp. 1–42. 36, 49

Lloberas-Valls, O., Rixen, D. J., Simone, A. and Sluys, L. J. [2012], 'On micro-to-macro connections in domain decomposition multiscale methods', *Computer Methods in Applied Mechanics and Engineering* **225-228**, 177–196. vii, 3, 8, 9, 12, 49, 58

Lorentz, E. and Badel, P. [2004], 'A new path-following constraint for strain-softening finite element simulations', *International Journal for Numerical Methods in Engineering* **60**(2), 499–526. 58, 61

Luo, J. F., Mao, S. C., Han, X. D., Zhang, Z., Wu, J. and Wu, M. H. [2007], 'Crystallographic mechanisms of fracture in a textured polycrystalline TiNi shape memory alloy', *Journal of Applied Physics* **102**(4), 043526.
URL: *http://link.aip.org/link/JAPIAU/v102/i4/p043526/s1&Agg=doi* 16

Mandel, J. [1993], 'Balancing Domain Decomposition', *Communications in Numerical Methods and Engineering* **241**(March 1992), 233–241. 36, 49

Massart, T. J., Peerlings, R. H. J. and Geers, M. G. D. [2007], 'Structural damage analysis of masonry walls using computational homogenization', *International Journal of Damage Mechanics* **16**(2), 199–226. 3, 5

Matous, K., Kulkarni, M. G., Geubelle, P. H. and Matous, K. [2008], 'Multiscale cohesive failure modeling of heterogeneous adhesives', *Journal of the Mechanics and Physics of Solids* **56**(4), 1511–1533. 5

Memon, B.-A., Su, X.-z., Bashir-ahmed, M. and Xiao-zu, S. U. [2004], 'Arc-length technique for nonlinear finite element analysis.', *Journal of Zhejiang University. Science* **5**(5), 618–628. 60

Menk, A. and Bordas, S. P. [2011], 'Crack growth calculations in solder joints based on microstructural phenomena with X-FEM', *Computational Materials Science* **50**(3), 1145–1156. 1

Michel, J. and Suquet, P. [2003], 'Nonuniform transformation field analysis', *International Journal of Solids and Structures* **40**(25), 6937–6955. 48

Mosler, J. [2007], On the numerical modeling of localized material failure at finite strains by means of variational mesh adaption and cohesive elements, PhD thesis, RUHR-UNIVERSITAT BOCHUM. 18

Mosler, J. and Scheider, I. [2011], 'A thermodynamically and variationally consistent class of damage-type cohesive models', *Journal of the Mechanics and Physics of Solids* **59**(8), 1647–1668. 19, 25

Nemat-Nasser, S. and Hori, M. [1999], *Micromechanics: overall properties of heterogeneous materials*, Vol. 1, 2 edn. 1, 17, 41, 42

Nguyen, O., Repetto, E. A., Ortiz, M. and Radovitzky, R. A. [2001], 'A cohesive model of fatigue crack growth', *International Journal of Fracture* pp. 351–369. 17

Nguyen, V. P., Lloberas-Valls, O., Stroeven, M., Johannes Sluys, L., Methods, C., Mech, A., Valls, O. L. and Sluys, L. J. [2011], 'On the existence of representative volumes for softening quasi-brittle materials A failure zone averaging scheme', *Computer Methods in Applied Mechanics and Engineering* **200**, 1220–1236. 3, 6

Nguyen, V. P., Lloberas-valls, O., Stroeven, M. and Sluys, L. J. [2012], 'Computational homogenization for multiscale crack modeling . Implementational and computational aspects', *International Journal for Numerical Methods in Engineering* **89**(2012), 192–226. 6

Oden, J. and Prudhomme, S. [2001], 'Goal-oriented error estimation and adaptivity for the finite element method', *Computers & Mathematics with Applications* **41**(5-6), 735–756.
URL: *http://linkinghub.elsevier.com/retrieve/pii/S0898122100003175* 98

Ogden, R. W. [1997], *Non-linear Elastic Deformations*, Dover Civil and Mechanical Engineering Series, Dover Publications. 82

Ortiz, M. and Pandolfi, A. [1999], 'FINITE-DEFORMATION IRREVERSIBLE COHESIVE ELEMENTS FOR THREE-DIMENSIONAL CRACK-PROPAGATION ANALYSIS', *International Journal for Numerical Methods in Engineering* **44**, 1267–1282. 17

Paggi, M. and Wriggers, P. [2011], 'Numerical modelling of intergranular fracture in polycrystalline materials and grain size effects', **17**, 5–14. 16, 18

Peerlings, R. H. J., De Borst, R., Brekelmans, W. A. M. and De Vree, J. H. P. [1996], 'Gradient enhanced damage for quasi-brittle materials', *International Journal for Numerical Methods in Engineering* **39**, 3391–3403. 10

Raghavan, P., Li, S. and Ghosh, S. [2004], 'Two scale response and damage modeling of composite materials', *Finite Elements in Analysis and Design* **40**, 1619–1640. 11

Riks, E. [1972], 'the application of Newtons method to the problem of elastic stability', *Journal of Applied Mechanics* **39**, 1060–1065. 58

Rollett, A. D., Saylor, D., Fridy, J., Brahme, A., Lee, S., Cornwell, C., Noack, R. and Livermore, L. [2004], 'Modeling Polycrystalline Microstructures in 3D', pp. 71–77. 16

Romkes, A., Oden, J. T. and Vemaganti, K. [2006], 'Multi-scale goal-oriented adaptive modeling of random heterogeneous materials', *Mechanics of Materials* **38**(8-10), 859–872. 3

Ruess, M., Schillinger, D., Bazilevs, Y., Varduhn, V. and Rank, E. [2011], 'Weakly enforced essential boundary conditions for NURBS-embedded and trimmed NURBS geometries on the basis of the finite cell method', *International Journal for Numerical Methods in Engineering* **00**, 1–20. 51

Runesson, K. and Larsson, F. [2008], 'Adaptive bridging of scales in continuum modeling based on error control', *International Journal for Multiscale Computational Engineering* **6**(4), 371—-392. 3

Sakai, M., Urashima, K. and Inagaki, M. [1983], 'Energy Principle of Elastic-Plastic Fracture and Its Application to the Fracture Mechanics of a Polycrystalline Graphite', *Journal of the American Ceramic Society* **66**(12), 868–874. 16

Schellekens, J. and Borst, R. D. [1993], 'On the numerical integration of interface elements', *International Journal for Numerical Methods in Engineering* **36**, 43–66. 60

Sfantos, G. K. and Aliabadi, M. H. [2007], 'A boundary cohesive grain element formulation for modelling intergranular microfracture in polycrystalline brittle materials', *International Journal for Multiscale Computational Engineering* **69**(July 2006), 1590–1626. 16, 17

Shabir, Z., Giessen, E. V. D., Duarte, C. a. and Simone, A. [2011], 'The role of cohesive properties on intergranular crack propagation in brittle polycrystals', *Modelling and Simulation in Materials Science and Engineering* **19**(3), 1–21. viii, 18, 29, 79

Sukumar, N., Srolovitz, D. J., Baker, T. J. and Prã, J. [2003], 'Brittle fracture in polycrystalline microstructures with the extended ÿnite element method', **2037**(January 2002), 2015–2037. 16, 18

Suquet, P. M. [1987], Elements of homogenization for inelastic solid mechanics, *in* A. Sanchez-Palencia, Enrique and Zaoui, ed., 'Homogenization Techniques for Composite Media', Springer Berlin Heidelberg, pp. 193–198. 2, 36

Talebi, H., Silani, M., Bordas, S. P. A., Kerfriden, P. and Rabczuk, T. [2013], 'A computational library for multiscale modeling of material failure', *Computational Mechanics* pp. 1–25. 13

Temizer, . and Wriggers, P. [2011], 'An adaptive multiscale resolution strategy for the finite deformation analysis of microheterogeneous structures', *Computer Methods in Applied Mechanics and Engineering* **200**(37-40), 2639–2661. vii, 8, 12, 13, 65, 66, 95

Toro, S., Sánchez, P. J., Huespe, A. E., Giusti, S. M., Blanco, P. J. and Feijóo, R. A. [2013], 'A two-scale failure model for heterogeneous materials : numerical implementation based on the finite element method', *International Journal for Numerical Method in Engineering* (October), 313–351. 7

Tvergaard, V. and Hutchinson, J. [1992], 'The relation between crack growth resistance and fracture process parameters in elastic-plastic solids.', *J. Mech. Phys. Solids* **40**, 1377–1397. 17

Tvergaard, V. and Hutchinson, J. [1993], 'The influence of plasticity on mixed mode interface toughness', *J. Mech. Phys. Solids* **41**, 1119–1135. 17

Unger, J. F. [2013], 'An FE2-X1 approach for multiscale localization phenomena', *Journal of the Mechanics and Physics of Solids* **61**, 928–948. 6

Unger, J. F. and Eckardt, S. [2011], 'Multiscale modeling of concrete', *Archives of Computational Methods in Engineering* **18**(3), 341–393. 9, 12, 45, 54, 87

Verhoosel, C. and Gutiérrez, M. [2009], 'Modelling inter- and transgranular fracture in piezoelectric polycrystals', *Engineering Fracture Mechanics* **76**(6), 742–

760.
URL: *http://linkinghub.elsevier.com/retrieve/pii/S0013794408001999* 16

Verhoosel, C. V., Remmers, J. J. C. and Gutiérrez, M. A. [2010], 'A partition of unitybased multiscale approach for modelling fracture in piezoelectric ceramics', *International Journal for Numerical Methods in Engineering* **82**(8), 966–994. 3, 5

Verhoosel, C. V., Remmers, J. J. C., Gutiérrez, M. A. and de Borst, R. [2010], 'Computational homogenization for adhesive and cohesive failure in quasi-brittle solids', *International Journal for Numerical Methods In Engineering* **83**(March), 1155–1179. 5

Vernerey, F. J. and Kabiri, M. [2012], 'An adaptive concurrent multiscale method for microstructured elastic solids', *Computer Methods in Applied Mechanics and Engineering* **241-244**, 52–64. ix, 8, 12, 65, 66

Wang, J. [2007], 'Cohesive zone model of FRP-concrete interface debonding under mixed-mode loading', *International Journal of Solids and Structures* **44**, 6551–6568. 17

Wang, Y., Ballarini, R. and Rodin, G. [2008], 'Crack-tip parameters in polycrystalline plates with soft grain boundaries', *Journal of engineering mechanics* **134**(January), 100–109. 7

Wei, Y. [2004], 'Grain-boundary sliding and separation in polycrystalline metals: application to nanocrystalline fcc metals', *Journal of the Mechanics and Physics of Solids* **52**(11), 2587–2616.
URL: *http://linkinghub.elsevier.com/retrieve/pii/S0022509604000833* 17, 18

Weinan, E. and Li, Xiantao and Vanden-Eijnden, E. [2004], Some recent progress in multiscale modeling, *in* P. Attinger, Sabine and Koumoutsakos, ed., 'Multiscale Modelling and Simulation', Springer Berlin Heidelberg, pp. 3–21. 2

Wempner, G. A. [1971], 'Discrete approximation related to nonlinear theories of solids', *International Journal of Solids and Structures* **7**, 1581–1599. 58

Xu, X.-P. and Needleman, A. [1994], 'NUMERICAL SIMULATIONS OF FAST CRACK IN BRITTLE SOLIDS', *Journal of Mechanics and Physics of Solids* **42**(9), 1397–1434. 17, 18

Yazdani, A. A., Gakwaya, A. and Dhatt, G. [1998], 'An improved superconvergent patch recovery technique for the axisymmetrical problems', *Computers & Structures* **66**(6), 799–821. 70

Zavattieri, P. D. and Espinosa, H. D. [2001], 'Grain level analysis of crack initiation and propagation in brittle materials', *Acta Materialia* **49**, 4291–4311. 16, 18

Zienkiewicz, O. C. and Zhu, J. Z. [1987], 'A simple error estimator and adaptive procedure for practical engineering analysis', *International Journal for Numerical Methods in Engineering* **24**(2), 337–357. 67, 68

Zienkiewicz, O. C. and Zhu, J. Z. [1992], 'The superconvergent patch recovery and a posteriori error estimates. Part 2: Error estimates and adaptivity', *International Journal for Numerical Methods in Engineering* **33**(7), 1365–1382. 70

Zohdi, T. I., Oden, J. T. and Rodin, G. J. [1996], 'Hierarchical modeling of heterogeneous bodies', *Computer Methods in Applied Mechanics and Engineering* **138**(1-4), 273–298. 8

Zohdi, T. I. and Wriggers, P. [2008], *An introduction to computational micromechanics*, Springer. 41, 99